Rare-Earth 3d Transition Metal Nanoparticles and Nanoflakes

by

Surfactant-Assisted High-Energy Ball Milling

by

Nilay Gündüz Akdoğan

A dissertation submitted to the Faculty of the University of Delaware in partial fulfillment of the requirements for the degree of Doctor of Philosophy in Physics

Summer 2012

ProQuest LLC.
789 East Eisenhower Parkway
P.O. Box 1346
Ann Arbor, MI 48106 - 1346

Rare-Earth 3d Transition Metal Nanoparticles and Nanoflakes

by

Surfactant-Assisted High-Energy Ball Milling

by

Nilay Gündüz Akdoğan

Approved: _____

George Hadjipanayis, Ph.D.
Chair of the Department of Department Name

Approved: _____

George H. Watson, Ph.D.
Dean of the College of College Name

Approved: _____

Charles G. Riordan, Ph.D.
Vice Provost for Graduate and Professional Education

I certify that I have read this dissertation and that in my opinion it meets the academic and professional standard required by the University as a dissertation for the degree of Doctor of Philosophy.

Signed: _____

George Hadjipanayis, Ph.D.
Professor in charge of dissertation

I certify that I have read this dissertation and that in my opinion it meets the academic and professional standard required by the University as a dissertation for the degree of Doctor of Philosophy.

Signed: _____

Yi Ji, Ph.D.
Member of dissertation committee

I certify that I have read this dissertation and that in my opinion it meets the academic and professional standard required by the University as a dissertation for the degree of Doctor of Philosophy.

Signed: _____

Stephen Barr, Ph.D.
Member of dissertation committee

I certify that I have read this dissertation and that in my opinion it meets the academic and professional standard required by the University as a dissertation for the degree of Doctor of Philosophy.

Signed: _____

Robert L. Opila, Ph.D.
Member of dissertation committee

ACKNOWLEDGMENTS

It is a pleasure to acknowledge the help, support and encouragement of a number of people to whom I am greatly indebted. First, I would like to greatly thank my advisor Prof. George C. Hadjipanayis. Not only he guided and encouraged me in my studies but he was also like a father to me during my years away from home. Of course, words can never be enough to say thanks to him. His influence will certainly continue to positively impact my life in every aspect.

I also would like to thank Dr. Alexander Gabay for all the discussions, his inspiration and friendship for all this years.

Finally, I wish to express my love and thanks to my husband Ozan for his loving support without whom this work would not be made possible. Also, to my family for their continues support.

Last but not the least I wish to thank each and everyone who have been a part of my life during my life here at University of Delaware, especially Sherry Rowland-Perry.

Dedicated to my husband, Ozan Akdogan…

TABLE OF CONTENTS

LIST OF TABLES

LIST OF FIGURES

ABSTRACT

The research work in this dissertation, was focused onthe fabrication of magnetic nanoparticles and nanoflakes by high-energy ball milling (HEBM), the understanding of their formation and the study of their fundamental and hard magnetic properties as a function of size and shape. A successful fabrication of (Sm, Nd & Pr)-Co, and $Nd_2Fe_{14}B$ anisotropic nanoparticles is needed for the development of anisotropic nanocomposite permanent magnets using the bottom-up approach. A novel approach has been employed for the fabrication, which is surfactant-assisted high-energy ball milling. A two-step HEBM was used to prepare the nanoparticles and the nanoflakes. In the first step the coarse powders were brought into the nanocrystalline state by using HEBM in heptane without the presence of surfactants. Surfactants during the milling process leads to the dispersion of crashed particles in the appropriate organic solvent, preventing them from welding, and enabling them to a better size refinement.

Size dependence of the coercivity was investigated on $Nd_2Fe_{14}B$ nanoparticles and it was found that the data follows a similar trend with theoretical prediction for the coherent rotation model where non-interacting single domain particles with uniaxial anisotropy are assumed. Magnetically hard $Nd_2Fe_{14}B$ nanopowders with RT coercivity in the range of 1.2 - 4 kOe have been produced by surfactant-assisted ball milling of nanocrystalline precursor alloys. The coercivity shows a strong dependence on particle size. As the particle size decreases, the coercivity is found to decrease substantially.

This effect has been attributed to both a reduced magnetocrystalline anisotropy of the nanoparticle because of surface disorder and to thermal effects.

The nanopowders consisted of $Nd_2Fe_{14}B$ flakes with a thickness below 100 nm and an aspect ratio as high as 10^2–10^3 and anisotropic square and irregular shape nanoparticles with a size in the range 2.7 to 25 nm. This is the first report on the fabrication of $Nd_2Fe_{14}B$ nano-cubes. It was found that the nanocrystalline structure acquired in the course of wet milling strongly influences the evolution of the particle shape and size during the second milling step. A strong correlation between the grain size of the nanoflakes and the size of the nanoparticles has been observed. The data suggests that the nanoparticles break from the nanoflakes along the grain boundaries during milling. When investigating shape evolution, it has been observed that $Nd_2Fe_{14}B$ flake had planar defects. These defect planes (including, perhaps, grain boundaries) facilitate the breakage of the flakes into square nanoparticles.

High temperature magnetic ordering studies on rare earth transition-metal nanoparticles and nanoflakes present a great challenge due to the very high reactivity of these materials. The problem has been addressed via Mn substitution for Fe in $Nd_2Fe_{14}B$ compound which decreases the Curie temperature to a temperature range that allows for reliable measurements to be made. Magnetic properties of Mn substituted $Nd_2Fe_{14}B$ particles have been studied in the temperature range of 50-400 K. Different size nanoparticles have been obtained by varying the milling conditions. The Curie temperature was determined from the temperature dependence of magnetization and susceptibility. It was found that the data shows a different magnetic ordering behavior in the nanoparticles with Curie temperatures that are much higher

when compared to the bulk values. We show that this enhancement is very well described by the finite-size-scaling model.

Another system with complex magnetic ordering behavior at different temperatures has been investigated; $NdCo_5$. Bulk $NdCo_5$ has a hexagonal $CaCu_5$ structure with the c-axis as the easy direction of magnetization above 290 K. The nanoparticles also showed spin reorientation temperatures, which are lower when compared to the bulk values. Compared to the powders and bulk samples, smaller spin reorientation values have been observed for the nanoparticles. The T_{SR1} and T_{SR2} transition temperatures observed for the nanoparticles are 276 K and 237 K, respectively. These values are lower when compared to the 290 K and 245 K values of bulk, indicating a likely size effect on the spin reorientation temperatures.

Chapter 1

INTRODUCTION

"I would like to describe a field, in which little has been done, but in which an enormous amount can be done in principle."

Richard P. Feynman
December 1959

In his historic talk "There is plenty of room at the bottom..." at Caltech in 1959, Richard Feynman, a Nobel Laureate, introduced the idea of NANO for first time. He emphasize on the enormous number of technical applications of this new field.

Influence of dimensions of a system on the fundamental magnetic properties constitutes a subject that has fascinated both theorists and experimentalists in the past several years [1,2]. This phenomenon is significant not only to our understanding of nature, but also to our current technology as efforts continue to create smaller and smaller devices. Recent years saw increasing demand for even finer permanent magnet powders based on the rare earth - transition metal (RE-TM) compounds. However, fabrication of ultra-fine powders from these highly reactive materials has always been very challenging. Most of the studies published so far on magnetically hard nanocrystalline intermetallic compounds are focused on polycrystalline samples made via mechanical alloying [4, 5] and ball milling [6, 7]. Very few studies exist on isolated nanoparticles [8-10] and micron-size particles [11] made by chemical synthesis. The chemical methods, nevertheless, have had limited success in the

synthesis of hard magnetic nanoparticles of rare-earth compounds. One of the approaches for preparation of hard magnetic nanoparticles is by surfactant-assisted ball milling [12-17], a technique, which has long being used for making magnetic fluids. However, the magnetic properties reported on these particles are inferior to those in bulk and the room-temperature coercivity of the as-synthesized nanoparticles with a size below 10 nm did not exceed 0.1 kOe [4, 5, 18, 19].

This study is aimed to investigate the formation of RE-TM nanoparticles and nanoflakes, which has been produced by a novel technique, surfactant-assisted high-energy ball milling; and study their fundamental and hard magnetic properties as a function of size and shape.

Besides the fundamental interest, these nanoparticles and nanoflakes are good candidates and may serve as precursors for the bottom-up fabrication of anisotropic exchange-coupled nanocomposite magnets consisting of a fine mixture of magnetically hard and soft particles [20, 21]. Though most suitable for a large-scale manufacturing, the *top-down approach* evidently does not provide a sufficient control over the size, morphology and orientation of the hard and soft elements. The alternative *bottom-up approach* implies assembling the material from small building blocks and, at least in principle, may give us the ultimate control over the resulting nanostructure. One *bottom-up* technique, most commonly used for the fabrication of nanocomposite magnets, is sputtering [22-24]. However, sputtering, in all its many varieties, is poorly suited for a large scale manufacturing of bulk materials. Besides sputtering, other *bottom-up* efforts to fabricate nanocomposite magnets so far have been scarce.

During the novel SA-HEBM process, as soon as the particles and/or fresh surfaces are formed, surfactants are absorbed on to the surface of the particles by the formation of the chemical bonds, which prevents agglomeration. This greatly reduces cold welding and the re-welding of crushed particles, which finally allows the separated particles with smaller sizes to be formed. The most important factor facilitating the nanoparticle formation is the compatibility of the surfactant used in the ball milling process. Polarity (the dielectric constant) of the liquid environment is known to be among the most important factors influencing the milling process [25]. The dispersibility of certain ceramic powders increases and their agglomeration decreases with increasing the dielectric constant of the surrounding liquid [26]. This plays a crucial role in obtaning the particles in the form of flakes.

In this dissertation, the (Sm, Nd & Pr)-Co, and $Nd_2Fe_{14}B$ alloys were the focus of attention. Magnetically hard stoichiometric $Nd_2Fe_{14}B$, Sm-Co-Fe, $PrCo_5$, $NdCo_5$ and $Nd_2Fe_{14-x}Mn_xB$ nanoparticles and nano-thick flakes were obtained by subjecting brittle alloys to a successive wet and surfactant-assisted HEBM (SA-HEBM). A two-step HEBM was used to prepare the nanoparticles and the nanoflakes.

Detailed information about the fabrication of nanoparticles and nanoflakes, characterization is presented in chapter 4. Chapter 5 is focused on the intrinsic magnetic properties of RE-TM nanoparticles and nanoflakes. Characterization and hard magnetic properties are discussed in chapter 6. Chapter 7 will give a brief conclusion of this work and the recommendations/suggestions for the future work.

REFERENCES

1. R. Skomski and J. M. D. Coey *Phys Rev* B 48, 15812 (1993).
2. G. C. Hadjipanayis and R.W. Siegel, Nanophase Materials: Synthesis-Properties- Applications. NATO ASI Series. 260 (1994).
3. H. Zeng, J. Li, J. P. Liu, Z. L. Wang and S. Sun *Nature* 420, 395 (2002).
4. L. Schultz, J. Wecker and E. Hellstern *J. Appl. Phys.* 61, 3583 (1987).
5. J. Han, S. Liu, X. Zhang, H. Du, C. Wang, Y. Yang, M. Yue and X. Liu *J. Appl. Phys.* 101, 09K502 (2007).
6. E. M. Kirkpatrick, S. A. Majetich and M. E. McHenry *IEEE Trans. Magn.* 32, 4502 (1996).
7. J. I. Lee, H. W. Kwon and Y. S. Kang *J. of Magnetics* 13, 102 (2008).
8. W. Liu and P. G. McCormick *Nano Stuctured Materials* 12, 187 (1999).
9. H. Gu, B. Xu, J. Rao, R. K. Zheng, X. X. Zhang, K. K. Fung and C. Y. C. Wong *J. Appl. Phys.* 93, 7589 (2003).
10. M. Tortarolo, R. D. Zyslera, H. Troiani and H. Romero *Physica B* 354, 117 (2004).
11. J. H. Lin, S. F. Liu, Q. M. Cheng, X. L. Qian, L. Q. Yang and M. Z. Su *J. Alloys Compd.* 249, 237 (1997).
12. V. M. Chakka, B. Altuncevahir, Z. Q. Jin, Y. Li and J. P. Liu *J. Appl. Phys.* 99, 08E912 (2006).
13. N. G. Akdogan, G. C. Hadjipanayis and D. J. Sellmyer *J. Appl. Phys.* 105, 07A710 (2009).
14. Y. Wang, Y. Li, C. Rong and J. P. Liu *Nanotechnology* 18, 465701 (2007).
15. H. G. Cha, Y. H. Kim, C. W. Kim, H. W. Kwon and Y. S. Kang *J. Phys. Chem.* 111, 1219 (2006).
16. M. Yue, Y. P. Wang, N. Poudyal, C. B. Rong and J. P. Liu *J. Appl. Phys.* 105, 07A708 (2009).

17. N. G. Akdogan, G. C. Hadjipanayis and D. J. Sellmyer *Nanotechnology* 21, 295705 (2010).

18. Z. M. Chen, X. Meng-Burany and G. C. Hadjipanayis *Appl. Phys. Lett.* 75, 3165 (1999).

19. Y. Zhang, A. M. Gabay, Y. Wang and G. C. Hadjipanayis *J. Magn. Magn. Mater.* 272-276, 1899 (2004).

20. I. I. Kryukov, N. A. Manakov, V. B. Sadkov and K. S. Sakhaev *Pisma v Zhurnal Tekhnicheskoi Fiziki* 15, 50 (1989).

21. E. F. Kneller, R. Hawig *IEEE Trans. Magn*. 27, 3588 (1991).

22. Z. Chen, Y. Zhang, Y. Ding, and G. C. Hadjipanayis, *J. Appl. Phys.* 85, 8 (1999).

23. L. Withanawasam, A. S. Murphy , G. C. Hadjipanayis and R. F. Krause *J. Appl. Phys.* 76, 7065 (1994).

24. Z. Chen, C. Ni, G.C Hadjipanayis, *J. Magn. Magn. Mater.* 186, 41 (1998).

25. H. El-Shall and P. Somasundaran *Powder Technol.* 38, 275 (1984).

26. Y. H. Choa, N. Bamba, H. Hayashi, H. Kondo, T. Sekino and K. Niihara *J. Mater. Sci.* 34, 3789 (1999).

Chapter 2

THEORETICAL BACKGROUND

2.1 Introduction to Magnetism

According to ancient reports Cleopatra was said to have slept on a lodestone for many years. At one point in history, it was thought that lodestone has healing and therapeutic powers. Magnets have attracted the attention of human being since 4th century. Today, in search of more efficient transportation techniques, power and energy generation, and magnetic technology is gaining considerable significance in today's world. As time goes on and technology continues to develop, our understanding of magnets will surely grow and continue to play a vital role in our everyday lives. Here in this chapter, a brief theoretical background is given on the origin of magnetism, the types of magnetism, the magnetic hysteresis loop and some basic nanomagnetism concepts.

2.2 Origin of magnetism

There are two kinds of electron motion, orbital and spin, and each has a magnetic moment associated with them. Thus each electron in an atom may be thought of as being a small magnet having permanent orbital and spin magnetic moments (Figure 2.1). The magnetic moment associated with each kind of motion is a vector quantity and magnetic moment of the atom is the vector sum of all its electronic moments. All materials exhibit at least one of these types of magnetism, and the behavior of the material depends on the response of electron and atomic magnetic

dipoles to the application of an externally applied magnetic field. The most fundamental magnetic moment is the *Bohr magneton* μ_B, which is of magnitude $0.927\times10^{-20}\ erg/Oe$. For each electron in an atom the spin magnetic moment is $\pm\mu_B$ (plus for spin up, minus for spin down). Furthermore, the orbital magnetic moment contribution is equal to being the magnetic quantum number of the electron [1].

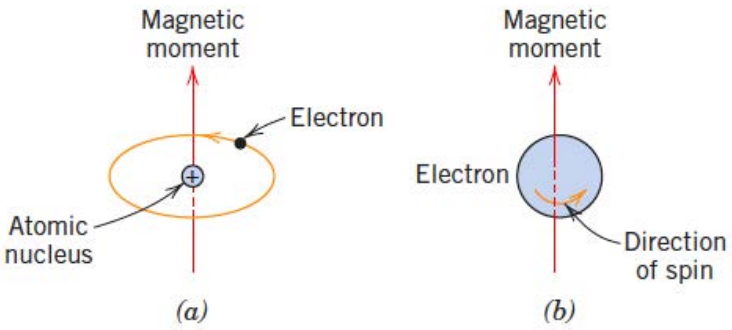

Figure 2.1 Demonstration of the magnetic moment associated with (a) an orbiting electron and (b) a spinning electron.

In each individual atom, orbital moments of some electron pairs cancel each other; this also holds for the spin moments. The net magnetic moment, then, for an atom is just the sum of the magnetic moments of each of the constituent electrons, including both orbital and spin contributions, and taking into account moment cancellation. For an atom having completely filled electron shells or subshells, when all electrons are considered, there is total cancellation of both orbital and spin moments. Thus materials composed of atoms having completely filled electron shells

are not capable of being permanently magnetized. The types of magnetism include diamagnetism, paramagnetism, and ferromagnetism; in addition, antiferromagnetism and ferrimagnetism are considered to be subclasses of ferromagnetism. The behavior depends on the response of electron and atomic magnetic dipoles to the application of an externally applied magnetic field.

The properties of ferromagnetic materials, which are used for characterization, can be separated in two main categories: intrinsic and extrinsic. The extrinsic properties, coercivity H_c, remanence M_r and initial permeability m_o depend strongly on microstructure, mechanical, stress and thermal properties. Intrinsic properties include the saturation magnetization M_s, magnetocrystalline anisotropy K and Curie temperature T_c, which depend on the type of material and its electronic structure.

DIAMAGNETISM

Diamagnetism is a fundamental property of all matter. Diamagnetism is a very weak form of magnetism that is nonpermanent and persists only while an external field is being applied. It is induced by a change in the orbital motion of electrons due to an applied magnetic field. The magnitude of the induced magnetic moment is extremely small, and in a direction opposite to that of the applied field. Thus, the relative permeability is less than unity (however, only very slightly), and the magnetic susceptibility is negative; that is, the magnitude of the B field within a diamagnetic solid is less than that in a vacuum.

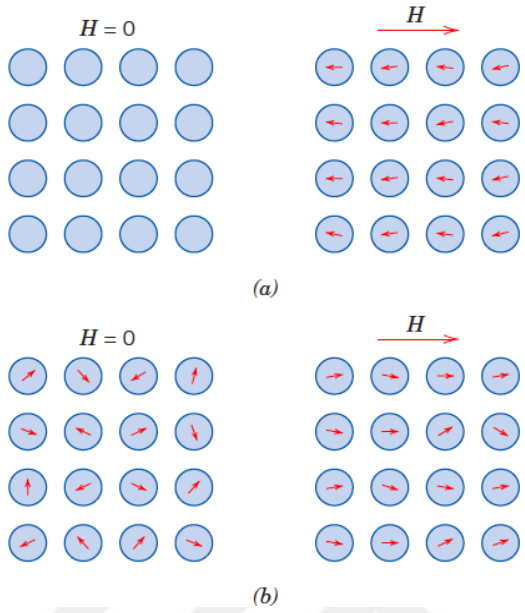

Figure 2.2 (a) The atomic dipole configuration for a diamagnetic material with and without a magnetic field. In the absence of an external field, no dipoles exist; in the presence of a field, dipoles are induced that are aligned opposite to the field direction. (b) Atomic dipole configuration with and without an external magnetic field for a paramagnetic material [1].

Figure 2.2 (a) illustrates schematically the atomic magnetic dipole configurations for a diamagnetic material with and without an external field; here, the arrows represent atomic dipole moments, whereas for the preceding discussion, arrows denoted only the electron moments. The dependence of B on the external field H for a material that exhibits diamagnetic behavior is presented in Figure 2.3. Diamagnetism is found in all materials; but because it is so weak, it can be observed only when other types of magnetism are totally absent. This form of magnetism is of no practical importance.

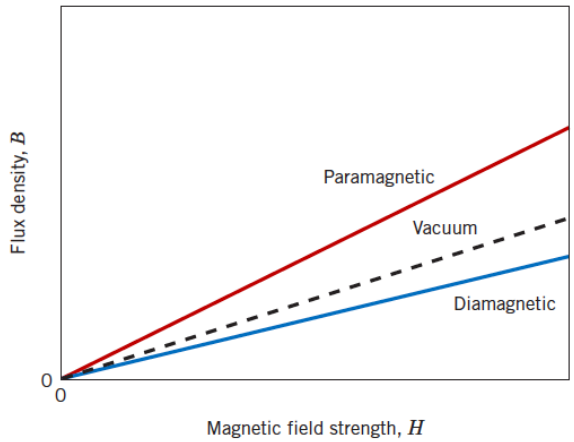

Figure 2.3 Schematic representation of the flux density B versus the magnetic field strength H for diamagnetic and paramagnetic materials [1].

PARAMAGNETISM

For some solid materials, each atom possesses a permanent dipole moment by virtue of incomplete cancellation of electron spin and/or orbital magnetic moments. In the absence of an external magnetic field, the orientations of these atomic magnetic moments are random (because of thermal energy), such that a piece of material possesses no net macroscopic magnetization. These atomic dipoles are free to rotate, and paramagnetism results when they preferentially align, by rotation, with an external field as shown in Figure 2.2 (b). These magnetic dipoles are acted on individually with no mutual interaction between adjacent dipoles. Inasmuch as the dipoles align with the external field, they enhance it, giving rise to a relative permeability that is greater than unity, and to a relatively small but positive magnetic susceptibility. A schematic B - versus-H curve for a paramagnetic material is also shown in Figure 2.3. Both

diamagnetic and paramagnetic materials are considered to be nonmagnetic because they exhibit magnetization only when in the presence of an external field.

FERROMAGNETISM

The most characteristic property of ferromagnets is that once exposed to a magnetic field they retain their magnetization even when the field is removed. This is schematically illustrated in Figure 2.4. This mutual spin alignment exists over relatively large volume regions of the crystal called domains. The movement of these domains determines how the material responds to a magnetic field [2].

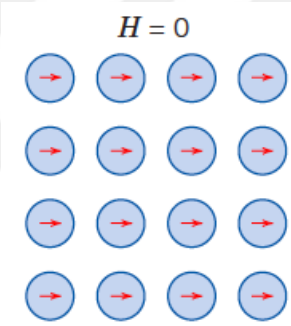

Figure 2.4 Schematic illustration of the mutual alignment of atomic dipoles for a ferromagnetic material, which will exist even in the absence of an external magnetic field.

The retention of magnetization distinguishes ferromagnets from paramagnets, which, although they acquire a magnetic moment in an applied magnetic field, cannot maintain the magnetization after the field is removed.

The most common way to represent the magnetic properties of a ferromagnetic material is by a plot of the magnetization M against the applied magnetic field H. In contrast to the non-hysteretic behavior of paramagnetic materials, which follows the

Brillouin function, the magnetization M of a ferromagnetic material exhibits a hysteretic behavior as a function of the applied magnetic field H (see Figure 2.5).

Important quantities determining an hysteresis loop are the coercive field H_c, the remanent magnetization M_r, and the saturation magnetization M_s. The area within the hysteresis loop is proportional to the work that has to be done to switch the magnetization from one direction to the opposite direction (this is usually converted to heat).

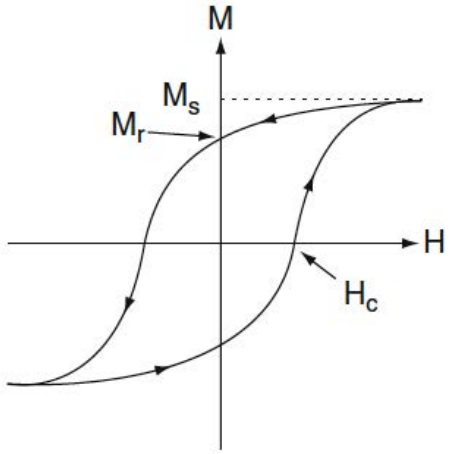

Figure 2.5 A typical hysteresis loop of a ferromagnetic material. M_s, M_r, and H_c are the saturation magnetization, the remanent magnetization, and the coercive field, respectively [2].

The maximum possible magnetization, or saturation magnetization, M_s of a ferromagnetic material represents the magnetization that results when all the magnetic dipoles in a solid piece are mutually aligned with the external field.

ANTIFERROMAGNETISM

The phenomenon of magnetic moment coupling between adjacent atoms or ions occurs in other materials besides those that are ferromagnetic. In one such group, this coupling results in an antiparallel alignment; the alignment of the spin moments of neighboring atoms or ions in exactly opposite directions is termed antiferromagnetism. Manganese oxide (MnO) is one material that displays this behavior. Manganese oxide is a ceramic material that is ionic in character, having both Mn^{2+} and O^{2-} ions. No net magnetic moment is associated with the O^{2-} ions, since there is a total cancellation of both spin and orbital moments. However, the Mn^{2+} ions possess a net magnetic moment that is predominantly of spin origin. These Mn^{2+} ions are arrayed in the crystal structure such that the moments of adjacent ions are antiparallel so the solid as a whole possesses no net magnetic moment [1].

FERRIMAGNETISM

Some ceramics also exhibit a permanent magnetization, termed ferrimagnetism. The macroscopic magnetic characteristics of ferromagnets and ferrimagnets are similar; the distinction lies in the source of the net magnetic moments. These ionic materials may be represented by the chemical formula MFe_2O_4, in which M represents any one of several metallic elements. The prototype ferrite is Fe_3O_4, the mineral magnetite, sometimes called lodestone. There are antiparallel spin-coupling interactions between the Fe ions, similar in character to anti-ferromagnetism. However, the net ferromagnetic moment arises from the incomplete cancellation of spin moments. Ferrimagnetism is therefore similar to ferromagnetism. Ferrimagnetism exhibits all the hallmarks of ferromagnetic behavior spontaneous: magnetization,

Curie temperatures, hysteresis, and remanence. However, ferro and ferrimagnets have very different magnetic ordering [1].

2.3 Hysteresis Loops

Magnetic hysteresis behavior is one of the most significant characteristics of ferromagnetic materials. The hysteresis loop is a means of characterizing various parameters. If the material is initially unmagnetized, then B varies as a function of H as shown in Figure 2.6. The curve begins at the origin, and as H is increased, the B field begins to increase slowly, then more rapidly, finally leveling off and becoming independent of H. This maximum value of B is the saturation flux density B_s, and the corresponding magnetization is the saturation magnetization M_s. As an H field is applied, the domains change shape and size by the movement of domain boundaries. Schematic domain structures are represented in the insets (labeled U through Z) at several points along the B-versus-H curve in Figure 2.6. Initially, the moments of the constituent domains are randomly oriented such that there is no net B (or M) field (inset U). As the external field is applied, the domains that are oriented in directions favorable to (or nearly aligned with) the applied field grow at the expense of those that are unfavorably oriented (insets V through X). This process continues with increasing field strength until the macroscopic specimen becomes a single domain, which is nearly aligned with the field (inset Y). Saturation is achieved when this domain, by means of rotation, becomes oriented with the H field (inset Z).

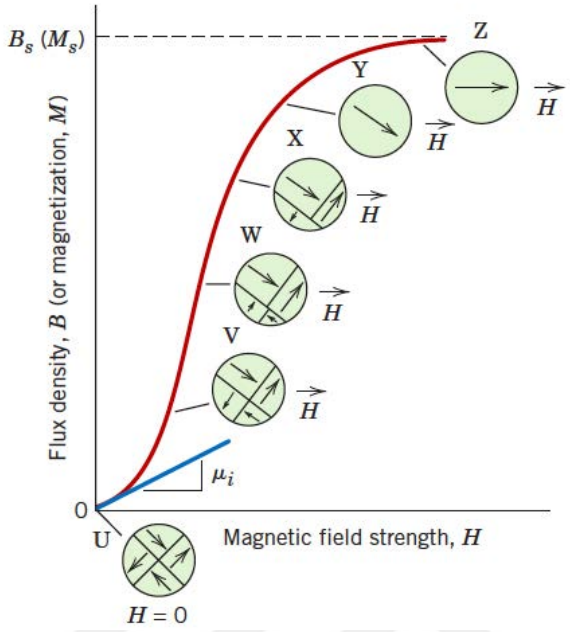

Figure 2.6 The B-versus-H behavior for a ferromagnetic or ferrimagnetic material that was initially unmagnetized. Domain configurations during several stages of magnetization are represented [1].

From saturation, point S in Figure 2.7, as the H field is reduced by reversal of field direction; the curve does not retrace its original path. A hysteresis effect is produced in which the B field lags behind the applied H field, or decreases at a lower rate. At zero H field (point R on the curve), there exists a residual B field that is called the remanence, or remanent flux density, B_r; the material remains magnetized in the absence of an external H field.

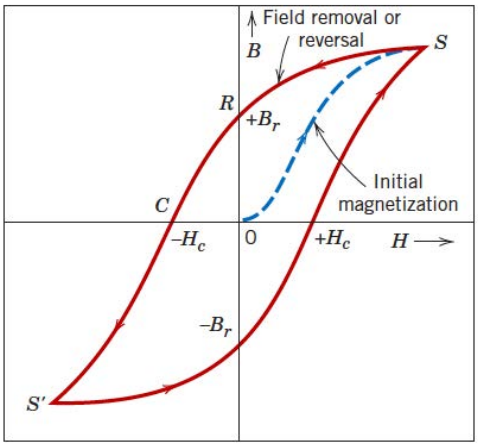

Figure 2.7 Magnetic flux density versus the magnetic field strength for a ferromagnetic material that is subjected to forward and reverse applied fields (points S and S`). The hysteresis loop is represented by the solid red curve; the dashed blue curve indicates the initial magnetization. The remanence B_r and the coercive force H_c are also shown [1].

Hysteresis behavior and permanent magnetization may be explained by the motion of domain walls. Upon reversal of the field direction from saturation (point S in Figure 2.7), the process by which the domain structure changes is reversed. First, there is a rotation of the single domain with the reversed field. Next, domains having magnetic moments aligned with the new field form and grow at the expense of the former domains. Critical to this explanation is the resistance to movement of domain walls that occurs in response to the increase of the magnetic field in the opposite direction; this accounts for the lag of B with H, or the hysteresis. When the applied field reaches zero, there is still some net volume fraction of domains oriented in the former direction, which explains the existence of the remanence B_r.

To reduce the B field within the specimen to zero (point C on Figure 2.7), an H field of magnitude $-H_c$ must be applied in a direction opposite to that of the original field; H_c is called the coercivity, or sometimes the coercive force. Upon continuation of the applied field in this reverse direction, as indicated in the figure, saturation is ultimately achieved in the opposite sense, corresponding to point S`. A second reversal of the field to the point of the initial saturation (point S) completes the symmetrical hysteresis loop and also yields both a negative remanence ($-B_r$) and a positive coercivity ($+H_c$). The B-versus-H curve in Figure 2.7 represents a hysteresis loop taken to saturation. The area contained within the loop indicates the amount of energy absorbed [$(BH)_{max}$] by the material during each cycle of the hysteresis loop and the remanence ratio $\mathbf{M_r/M_s}$ is generally used as measure of squareness of the **M-H** loop. The maximum energy product $(BH)_{max}$ is a measure of the maximum amount of useful work that can be performed by the magnet. $(BH)_{max}$ is used as a figure of merit for permanent magnet materials. In addition, the shape of the initial magnetization curve can provide information about the magnetic domain behavior within the material.

Magnetic materials with high coercivity and relatively large remanence are known as hard magnets (permanent magnet). The most common use of these magnets are as actuators, motors, microwave generators, magnetic lenses etc. On the other hand magnetic materials with small coercivity are known as soft magnets. As represented in Figure 2.8, their loop is characteristically thin and narrow. Consequently, a soft magnetic material must have a high initial permeability and a low coercivity. A

material possessing these properties may reach its saturation magnetization with a relatively low applied field. Soft magnets are used as transformers, inductors, generators and in magnetic recording head.

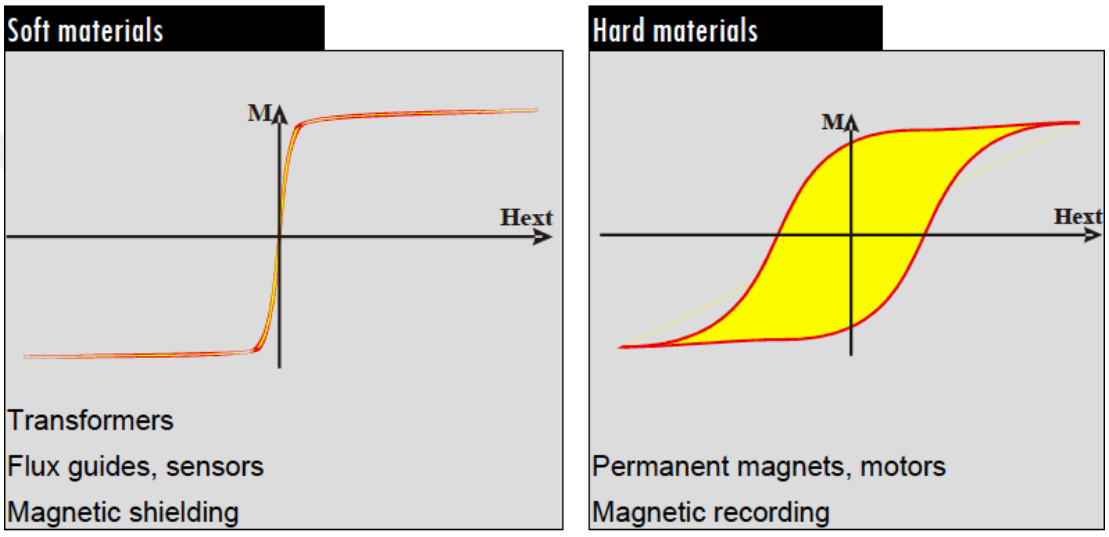

Figure 2.8 Schematic magnetization curves for soft and hard magnetic materials [3].

2.4 Exchange Energy

The magnet's mystery, explain that to me!
No greater mystery but love and hate.

Johann Wolfgang von Goethe (1749–1832)

In 1928, the year of Dirac's QED theory, there was another important breakthrough in the history of magnetism with Heisenberg's formulation of a spin-dependent model for the exchange interaction. The molecular field postulated by Weiss could now be interpreted as having its origin in the exchange interaction. The

introduction of the strong, short-range exchange interaction constituted the birth of modern magnetism theory, which has its roots in, both, quantum theory and relativity. The exchange interaction between two neighboring spin moments arises as a consequence of the overlap between the magnetic orbitals of two adjacent atoms. This so-called direct exchange interaction is strong in particular for 3d metals, because of the comparatively large extent of the 3d-electron charge cloud.

The exchange force is a consequence of the Pauli exclusion principle, applied to the two atoms as a whole. This principle states that two electrons can have the same energy only if they have opposite spins. Thus two hydrogen atoms can come so close together that their two electrons can have the same velocity and occupy very nearly the same small region of space, i.e., have the same energy, provided these electrons have opposite spin. If their spins are parallel, the two electrons will tend to stay far apart. Heisenberg showed that the exchange interaction also plays a decisive role in ferromagnetism. If two atoms i and j, then the exchange energy between them is given by $E_{ex} = -2\,J_{ex}S_iS_j\cos\phi$, where J_{ex} is a particular integral, called the ***exchange integral***, which occurs in the calculation of the exchange effect, and ϕ is the angle between the spins. If J_{ex} is positive, E_{ex} is a minimum when the spins are parallel ($\cos\phi$ =1) and a maximum when they are antiparallel ($\cos\phi$ = -1). If J_{ex} is negative, the lowest energy state results from antiparallel spins. As we have already seen, ferromagnetism is due to the alignment of spin moments on adjacent atoms. A positive value of the exchange integral is therefore a necessary condition for ferromagnetism to occur. This is also a rare condition, because J_{ex} is commonly negative, as in the hydrogen molecule [4].

2.5 Magnetic anisotropy

One factor, which may strongly affect the shape of the **M**, **H** (or **B**, **H**) curve, or the shape of the hysteresis loop, is magnetic anisotropy. This term simply means that the magnetic properties depend on the direction in which they are measured. There are several kinds of anisotropy:

1. Crystal anisotropy, formally called magnetocrystalline anisotropy
2. Shape anisotropy
3. Stress anisotropy

Of these, only crystal anisotropy is intrinsic to the material.

The term magnetic anisotropy is used to describe the dependence of the internal energy on the direction of the spontaneous magnetization, creating easy and hard directions of magnetization. The total magnetization of a system will prefer to lie along the easy axis. The energetic difference between the easy and hard axis results from two microscopic interactions: the spin-orbit interaction and the long-range dipolar coupling of magnetic moments. The anisotropy energy arises from the spin-orbit interaction and the partial quenching of the angular momentum. The spin-orbit coupling is responsible for the intrinsic (magnetocystalline) anisotropy, surface anisotropy, and magnetostriction, while the shape anisotropy is a dipolar contribution and is calculated e.g. by assuming a uniform distribution of magnetic poles on plane surfaces. Anisotropy energies are usually in the range 10^{2}-10^{7} Jm^{-3}. This corresponds to energy per atom in the range 10^{-8}-10^{-3} eV. The anisotropy energy is larger in lattices (of magnetic ions) of low symmetry and smaller in lattices of high symmetry. In bulk materials, magnetocrystalline and magnetostatic energies are the main source of anisotropy whereas in fine particles, thin films and nanostructures, other kinds of anisotropies such as shape and surface anisotropy are relevant in addition to these

usual anisotropies. In the following we will discuss four different contributions to magnetic anisotropy: magnetocrystalline anisotropy, shape anisotropy, strain anisotropy [4].

2.5.1 Magnetocrystalline Anisotropy

In a solid, the electron orbitals of an atom are coupled to the crystal lattice, leading thus to a particular orientation of the electron orbitals with respect to the crystalline axes. As the associated orbital angular momentum (**L**) is coupled to the spin angular momentum (**S**) through the spin–orbit interaction ($E_{so} = L \cdot S$), the orientation of orbitals forces the spin magnetic moments in one or more particular directions, the so-called easy directions of magnetization. This phenomenon of magneto-crystalline anisotropy is the reason why a rotation of the spin direction relative to the crystalline axes changes both the exchange energy and electrostatic interaction. Thus, the energies in the two configurations (a) and (b) in Figure 2.9 are not identical. Usually, the configuration (a) is energetically more favorable, because in this configuration the electrons can be more easily delocalized, thanks to the overlap of neighboring electron distributions, while no overlap is realized in the configuration (b). On the other hand, the uncertainty principle of Heisenberg tells us that the uncertainty of the velocity is small when the uncertainty of the position is large, that is, the kinetic energy is much smaller in the configuration (a).

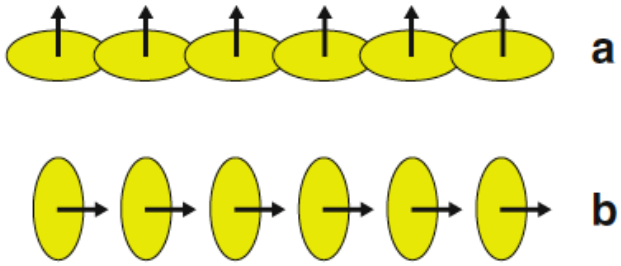

Figure 2.9 The asymmetric overlap of the electron distributions at neighboring positions is the origin of the magneto-crystalline anisotropy. Via the spin–orbit interaction this asymmetry is related to the magnetization direction; a change of the spin direction results thus in a change of the overlap energy [2].

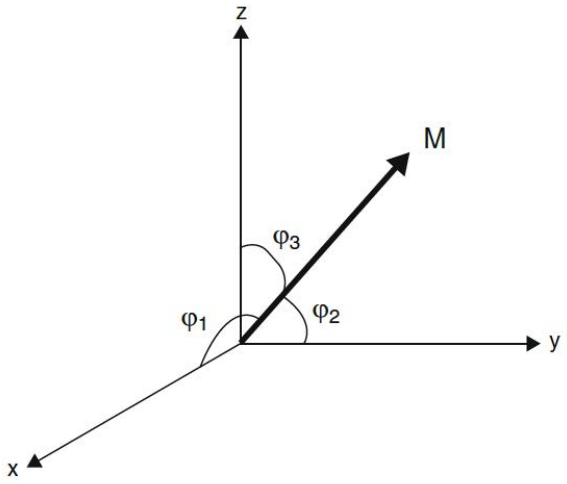

Figure 2.10 The magnetization M and the angles ϕ_i between the magnetization and the principal axes *i, i.e., x, y,* and *z* [2].

On one hand, the energy must be invariant under time reversal. On the other hand, the axial vector M changes sign under time reversal, so that we must have

$\boldsymbol{E_A}(M) = \boldsymbol{E_A}(-M)$. Thus, the energy expression must contain neither odd power terms of $\boldsymbol{\alpha_i}$ nor cross terms such as $\boldsymbol{\alpha_i \alpha_j (i \neq j)}$.

As an example, let us consider the cubic case (sc, fcc, bcc). Consequently, the anisotropy energy must be independent of an interchange of the α_i. As a result, the c_i in the second order contribution $E_A = c_1{\alpha_1}^2 + c_2{\alpha_2}^2 + c_3{\alpha_3}^2$ are all identical. On the other hand, ${\alpha_1}^2 + {\alpha_2}^2 + {\alpha_3}^2 = 1$, so that no anisotropy results from it. The first nonvanishing anisotropy terms are of fourth and sixth order: ${\alpha_1}^2{\alpha_2}^2 + {\alpha_2}^2{\alpha_3}^2 + {\alpha_3}^2{\alpha_1}^2$ and ${\alpha_1}^2{\alpha_2}^2{\alpha_3}^2$.

Therefore, $E_A/V = K_1({\alpha_1}^2{\alpha_2}^2 + {\alpha_2}^2{\alpha_3}^2 + {\alpha_3}^2{\alpha_1}^2) + K_1\,{\alpha_1}^2{\alpha_2}^2{\alpha_3}^2 + \cdots$, with K_1 and K_2 the anisotropy constants of fourth and sixth order, respectively. We note that the unit of the anisotropy constants is Jm^{-3} [2].

Generally the magnetic anisotropy energy term possesses the crystal symmetry of the material, and known as crystal magnetic anisotropy or magnetocrystalline anisotropy [5]. The simplest forms of crystal anisotropies are the uniaxial anisotropy in the case of a hexagonal and the cubic anisotropy in the case of a cubic crystal. For example, hexagonal cobalt exhibits uniaxial anisotropy, which makes the stable direction of internal magnetization (or easy direction) parallel to the c axis of the crystal at room temperature. For uniaxial symmetry the energy is given by

$$E_a^{uni} = K_0 + K_1 V \sin^2\theta + K_2 V \sin^4\theta + \cdots \qquad (2.1)$$

Where K_1 and K_2 are anisotropy constants, V is the particle volume and θ is the angle between the magnetization and the symmetry axis. The K's are dependent on temperature [6, 7], but at temperatures much lower than the Curie temperature of the

material they can be considered as constants. Usually in case of ferromagnetic materials K_2 and other higher order coefficients are negligible in comparison with K_1 and many experiments may be analyzed by using the first term only. In the convention of Eq. (2.1), $K_1 > 0$ implies an easy axis. For single-domain particles with uniaxial anisotropy most of the calculations are performed also by neglecting K_2 and the magnetocrystalline anisotropy energy is written as:

$$E_a^{uni} = KV \sin^2\theta \qquad (2.2)$$

Where K is usually considered as the uniaxial anisotropy constant. This expression describes two local energy minima at each pole (θ = 0 and p) separated by an equatorial (θ = 90) energy barrier KV.

We note that beside the magneto-crystalline anisotropy, there is another important contribution leading to magnetic anisotropy via spin–orbit interaction, namely **magnetostriction**. The spin moments are coupled to the lattice via the orbital motion of the electrons. If the lattice is changed by strain, the distances between the magnetic atoms are altered and hence the interaction energies are changed. Thus, stressing or straining a magnetic material can produce a change in its preferred magnetization direction.

2.5.2 Shape anisotropy

Shape anisotropy is not an intrinsic property of a material. Rather, it is due to a geometrically induced directional dependency of the demagnetization field H_d within

the specimen. For example, take a long thin needle shaped grain. The demagnetizing field will be less if the magnetization is along the long axis than if is along one of the short axes. This produces an easy axis of magnetization along the long axis (Figure 2.11). A sphere, on the other hand, has no shape anisotropy. The magnitude of shape anisotropy is dependent on the saturation magnetization [8]. The internal field is written as:

$$\vec{H}_i = H_{Applied} - N \cdot \vec{M} \tag{2.3}$$

Where M is the magnetization of the sample and N is the demagnetization factor, which depends on the geometry of the sample, and along the direction the magnetization curve is measured.

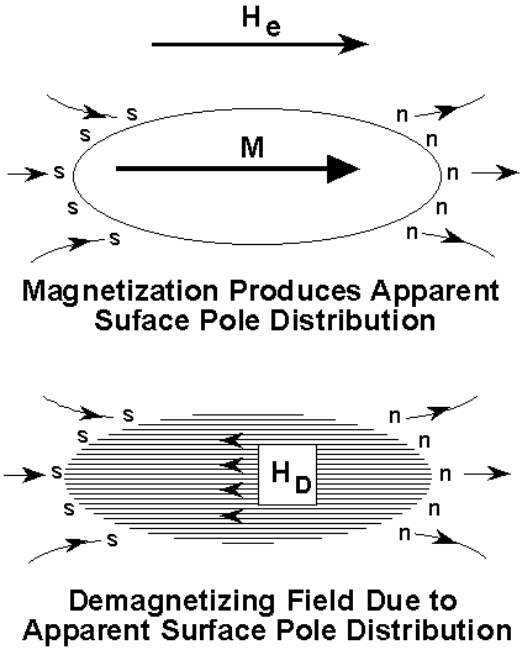

Figure 2.11 Schematic representation of shape anisotropy [9].

2.5.3 Stress Anisotropy

Exchange energy depends strongly on the details of the physical interaction between orbitals in neighboring atoms with respect to one another; hence changing the positions of these atoms will affect that interaction. Put another way, straining a crystal will alter its magnetic behavior. Similarly, changes in the magnetization can change the shape of the crystal by altering the shapes of the orbitals. This is the phenomenon of magnetostriction. The magnetic energy density caused by the application of stress to a crystal be approximated by:

$$E_\sigma = \frac{3}{2}\bar{\lambda}\sigma sin^2\theta \qquad (2.4)$$

Where λ is an experimentally derived constant, σ is the stress, and θ is the angle of the stress with respect to the c crystallographic axis. Moskowitz (1993) measured the magnetostriction constants parallel to [111] and [100] in magnetite and found λ_{111} and λ_{100} to be 78.2×10^{-6} and -21.8×10^{-6} respectively. λ is given by:

$$\bar{\lambda} = \frac{2}{5}\lambda_{100} + \frac{3}{5}\lambda_{111} \qquad (2.5)$$

So λ for magnetite is about 38×10^{-6}. Stress has units of Nm^{-2}, which have the same fundamental units as Jm^{-3}, so λ is dimensionless. Note the similarity in form of magnetostriction and uniaxial anisotropy giving rise to a single "easy axis" within the crystal [10].

2.6 Physics of Small Particles

Magnetic nanoparticles exhibit a variety of unique magnetic phenomena that are drastically different from those of their bulk counterparts due to large surface to volume ratio at nanometer scale. As the particles size decreases, a large percentage of all the atoms in a nanoparticle are surface atoms, which implies that surface and interface effects become more important. For example, for face-centered cubic (fcc) cobalt with a diameter of around 1.6nm, about 60% of the total number of spins are surface spins [4, 12]. Owing to this large surface atoms/bulk atoms ratio, the surface spins make an important contribution to the magnetization. This local breaking of the symmetry might lead to changes in the band structure, lattice constant or/and atom coordination. Under these conditions, some surface and/or interface related effects occur, such as surface anisotropy.

Magnetic properties of small ferromagnetic particles, such as coercivity and saturation magnetization, are mainly influenced by two critical features: *i)* a size limit below which the specimen cannot be broken into domains, and so it remains single domain; and *ii)* the thermal energy in small particles, which decouples the magnetization and in turn gives rise to the phenomenon of superparamagnetism. These two important features are represented by two critical sizes: single domain size and superparamagnetic size [12].

2.6.1 Domains

In ferromagnetic materials, individual atomic magnetic moments have a tendency to align parallel to each other, keeping at a lower value a type of energy known as the exchange energy. The origin of the exchange energy $E_{exchange}$ can be found in spin–spin interactions that constitute the basis for ferromagnetism [5]. When the spins of unpaired electrons are parallel, the exchange energy is minimum. However, the parallel alignment of spins and thereby atomic magnetic moments increases another kind of energy, the magnetostatic energy $E_{magnetostatic}$. In a magnetized large single crystal, large external magnetic fields are created, a process shown schematically in Figure 2.12. Therefore, to decrease the magnetostatic energy related to the large stray fields, a division into magnetic domains with antiparallel magnetizations occurs while also magnetic walls start to form between these domains (Figure 2.13). In this configuration, the exchange energy is somewhat increased; however, the magnetostatic energy is lowered. Several magnetic domains are thereby formed within the material so that each domain will contain individual magnetic moments. These moments add up to a total magnetization in each magnetic domain. Adjacent domains are separated by domain boundaries or walls, across which the direction of magnetization gradually changes (Figure 2.12 (b)). In the absence of a field, the average magnetization of the domains is zero.

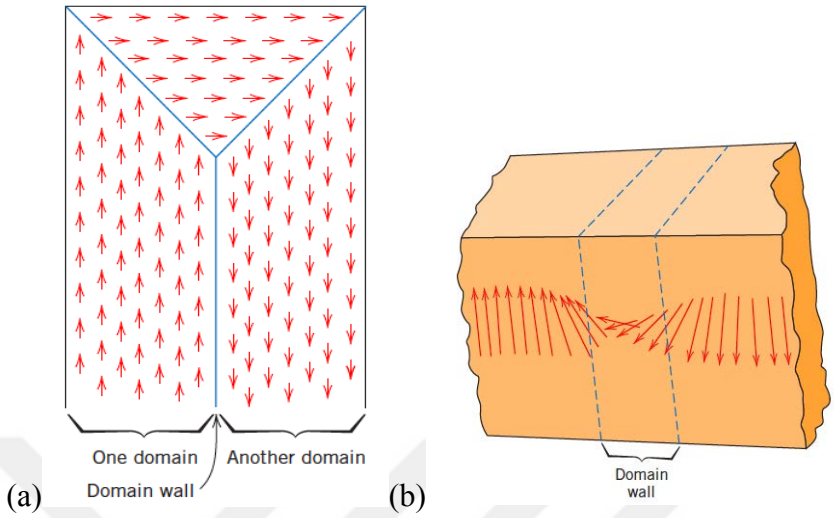

Figure 2.12 (a) Schematic depiction of domains in a ferromagnetic or ferrimagnetic material; arrows represent atomic magnetic dipoles. Within each domain, all dipoles are aligned, whereas the direction of alignment varies from one domain to another. (b) The gradual change in magnetic dipole orientation across a domain wall [13].

The five basic energies [4] involved in the formation of magnetic domains are thus:

$$E = E_{exchange} + E_{magnetostatic} + E_{magnetocrystalline} + E_{magnetoelastic} + E_{wall} \quad (2.6)$$

Formation of a certain magnetic configuration is the outcome of the sum of the five basic energies being minimized, although the energies themselves may not be at their minimum. As a consequence of this minimization competition between five different energies, ferromagnetic materials divide spontaneously into magnetic domains.

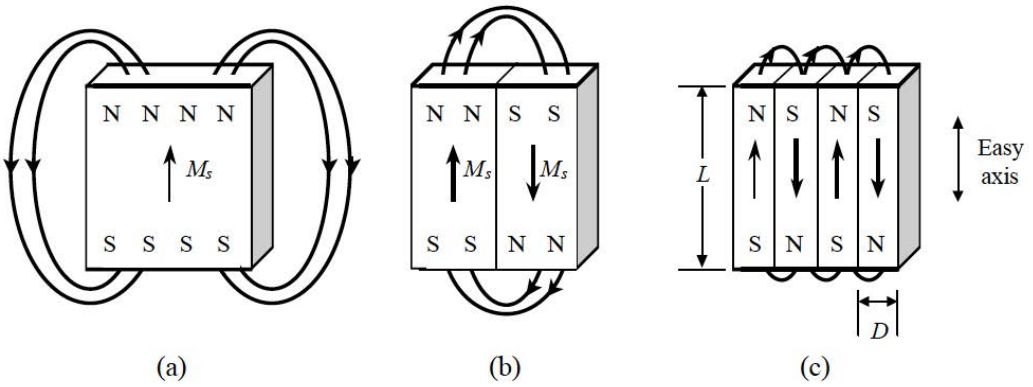

Figure 2.13 Domains in uniaxial ferromagnet (a) uniformly magnetized (b) divided into two and c) four domains.

To describe single-domain particles, it must be considered that the formation of magnetic domains is determined by the competition between domain wall energy lost and demagnetizing field energy gained. The walls are quasi-2D objects and the domain wall energy is thus a surface energy term [14]. As the volume of the particle decreases, the strength of the wall energy is relatively reduced with respect to that of the demagnetizing field energy term, a volume term. At very small sizes, the state of minimum energy is the single domain state. For uniaxial materials, a rough estimate of the single domain particle size can be obtained using the procedure discussed below. The magnetostatic energy per unit area of the single domain crystal is (Figure 2.13 (a)),

$$E_{ms} = 2\pi M_s^2 L \qquad (2.7)$$

For the uniaxial multi-domain crystal (Figure 2.13 (c)), the calculation of the magnetostatic energy gives:

$$E_{ms} = 1.7M_s^2 D \tag{2.8}$$

where D is the width of the domains, and the domain wall energy is :

$$E_{wall} = \gamma \frac{L}{D} \tag{2.9}$$

where γ is the domain wall energy per unit area, $\gamma = 4\sqrt{AK}$, A is the exchange constant and K is the crystal anisotropy. If the total magnetostatic energy per unit area $E_{total} = 1.7M_s^2 D + \gamma \frac{L}{D}$ is assumed, the minimum energy occurs when:

$$\frac{dE_{total}}{dD} = \frac{d(E_{ms} + E_{wall})}{dD} = 1.7M_s^2 - \gamma \frac{L}{D^2} = 0 \tag{2.10}$$

which yields:

$$D = \sqrt{\frac{\gamma L}{1.7M_s^2}} \tag{2.11}$$

Therefore, the minimum energy is calculated to be:

$$E_{min} = 2\sqrt{1.7M_s^2 \gamma L} \tag{2.12}$$

Equating the crystal`s energy as a single domain given by eq. (2.7) with its energy when divided into domains, eq. (2.12), L_c (single-domain particle size) is found to be:

$$L_c = \frac{1.7\gamma}{\pi^2 M_s^2} \tag{2.13}$$

For $Nd_2Fe_{14}B$ particles, $L_c = 0.4\,\mu$. Single domain particle formation implies that the observation of coercivity does not require prior magnetic saturation under applied field, unlike the case of multi-domain particles. In itself, it does not give any indication on the magnetization reversal process involved under H_{app}.

Magnetization reversal in single-domain particle occurs via spin rotation, since there are no domain walls to move. Single-domain particles consequently have a larger coercivity compared to multi-domain system, as it is harder to rotate the magnetization than to move a domain wall. In this single-domain regime, the magnetic coercivity increases as the size of the nanoparticle increases (Figure 2.14).

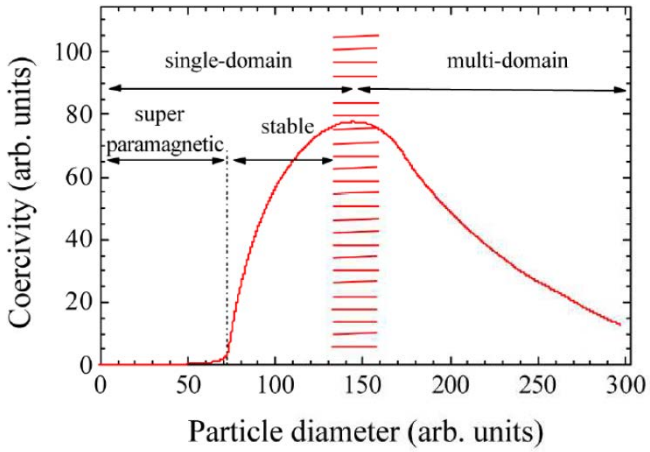

Figure 2.14 Variation of coercivity with particle diameter.

Above the critical size ($L > L_c$), multi-domain magnetism begins in which a smaller reversal magnetic field is required to make the net magnetization zero.

Saturation magnetization of nanoparticles is also strongly dependent on their size. Magnetic materials intrinsically possess magnetically disordered spin glass like layers near the surface due to the reduced spin–spin exchange coupling energy at the surface [15, 16]. In bulk cases, since the disordered surface layer is minimal compared to the total volume of the magnet, such surface spin canting effects are negligible. Upon reduction of the size of magnetic materials to the nano-scale regime, however, the surface canting effects are dramatically pronounced in the saturation magnetization value (m_s), described as:

$$m_s = M_S\,[(r - d)/r]^3 \qquad (2.14)$$

where r is the particle radius, M_S is the saturation magnetization of bulk materials, and d is the thickness of disordered surface layer. For very small nanoparticles (less than ~ 5 nm) such size effect on m_s is more noticeable, since internal spins of the nanoparticle also start to be canted as do the surface spins because of increased interactions between the surface and internal spins.

It is important to keep in mind that the critical single-domain size is largely unrelated to hysteresis [17, 18]. First, L_c is a ground-state property, comparing free energies of single-domain and multi-domain states, whereas hysteresis is a non-equilibrium phenomenon caused by free-energy barriers.

2.6.2 Stoner- Wohlfarth Model

The resistance to magnetization reversal indicates that an energy barrier separates the initial and the final magnetic states [19, 20]. This energy barrier is a

consequence of magnetic anisotropy. This can be illustrated within the so-called Stoner-Wohlfarth (SW) model, in which reversal is assumed to occur by in-phase rotation of all moments (coherent rotation) [21]. For H_{app}, antiparallel to M, the energy may be expressed as:

$$E = K sin^2 \Phi + \mathrm{M}\, H_{app} cos\Phi \tag{2.15}$$

where Φ is the angle between M and z (Φ = 0 in the initial state). In Eq. (2.15), the first term represents the anisotropy energy and the second term represents the Zeeman energy. From energy minimization, it is found that the barrier against reversal vanishes when H_{app}, reaches the value of the so-called anisotropy field $H_A = 2\ K/M_s$ (by definition, H_A is the field required to align the moment along a field applied perpendicular to z).

$$\frac{dE_{total}}{d\theta} = 2K\ sin\theta\ cos\theta - H\ M_s \sin(\phi - \theta) = 0 \tag{2.16}$$

$$\frac{d^2E_{total}}{d\theta^2} > 0 \tag{2.17}$$

Magnetization measurement along the applied field direction gives a value $M = M_s \cos(\phi - \theta)$. In order to simplify these equations, dimensionless quantities h and m have been substituted,

$$sin\theta\ cos\theta - h \sin(\phi - \theta) = 0 \tag{2.18}$$

where

$$h = \frac{HM_S}{2K} \qquad m = \frac{M}{M_s} = \cos(\phi - \theta) \tag{2.19}$$

The switching field, for a given angle θ, is the point where the solution changes from an energy minimum ($d^2E_{total}/d\theta^2 > 0$) to an energy maximum (($d^2E_{total}/d\theta^2 < 0$). Thus, the critical field h_{cr} and the critical angle θ_{cr} at which the magnetization flip can be calculated by solving eq. (2.16) along with energy minimum equation. And it gives:

$$\theta_c = arctan\sqrt[3]{-tan\phi} \qquad h_{cr} = \sqrt{(1 - \tfrac{3}{4}sin^2 2\theta_{cr})} \tag{2.20}$$

solving these equations lead to:

$$H_{cr} = \frac{2K}{M_S}\, h_{cr} = \frac{2K}{M_S}\sqrt{(1 - \tfrac{3}{4}sin^2 2\theta_{cr})} \tag{2.21}$$

Using eq. (2.18) and (2.19), hysteresis loops for different angles can be plotted. (Figure 2.15) For a system of non-interacting uniaxial particles with their easy-axis randomly oriented in space, Stoner and Wohlfarth calculated that h_{cr} is calculated as $h_{cr} = 0.48$ and $m_{cr} = 0.5$; which can be reinterpreted in terms of the quantities with dimensions as,

$$H_c = 0.48\left(\frac{2K}{M_S}\right) \qquad M_r = \frac{M_S}{2} \tag{2.22}$$

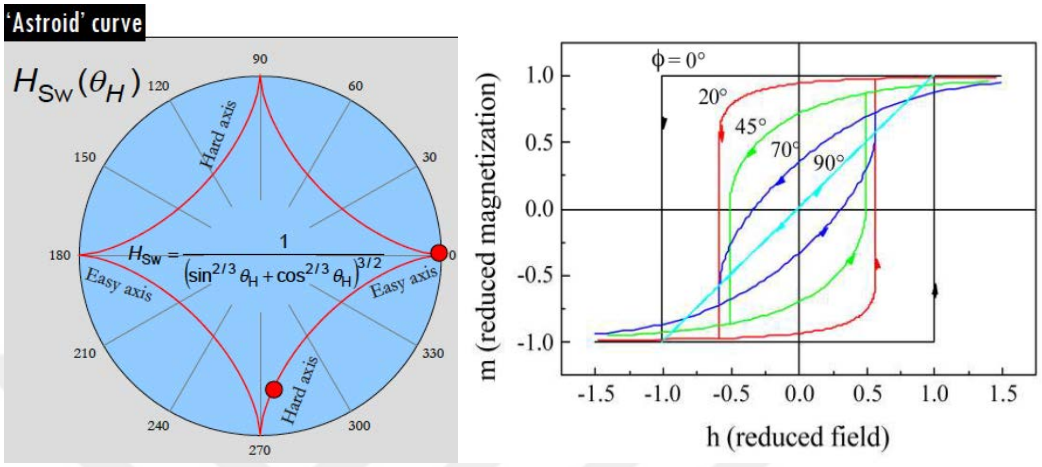

Figure 2.15 Astroid curve and some hysteresis loops predicted by the Stoner-Wohlfarth model for different angles between the field and easy-axis [3].

2.6.3 Superparamagnetic Region

Thermal activation effects become more effective at very small particle size. In particular, they lead to the appearance of superparamagnetism [21]. Consider a single domain uniaxial particle, which may reverse its magnetization by coherent rotation. In zero applied field, the barrier against reversal amounts to $\Delta E = KV$, where V is the particle volume. The particle moment may fluctuate above the energy barrier at a frequency equal to $1/\tau$. In systems made of micron size particles, τ amounts to values longer than any physical time. Thermal activation effects are insignificant. However, when the particle volume is reduced in the nanosize range, the time τ may be reduced to values of the order of the characteristic time of the measurement technique used. For instance, the characteristic time of magnetization measurements is typically 1s; it is reached at the so-called blocking temperature T_B such that $\Delta E/kT_B \approx 25$. Above T_B, the magnetization fluctuates above the energy barrier; it behaves similarly as if it

was paramagnetic (note that T_B depends on the measurement technique). The phenomenon of superparamagnetism sets a limit to the exploitation of nanoparticle hard magnetic properties. In 4 nm diameter Co metal nanoparticles, $T_B = 50$ K; in $Nd_2Fe_{14}B$ particles of the same diameter, it is of the order of 450 K (using the bulk values).

Even below T_B, the magnetization of nanoparticles may be strongly affected by thermal activation. Very small Co particles showing coherent rotation allowed thermal activation effects to be analyzed quantitatively [22]. From 40 mK up to 12 K, the coercive field was found to be a function of the expression theoretically expected for thermal activation, $T \ln \frac{\tau}{\tau_0}^{2/3}$. The volume of the smallest hard $Nd_2Fe_{14}B$ nanoparticles obtained until today is of approximately 10^5 nm^3. This is 100 times more than the size of the activation volume usually measured in Nd-Fe-B magnets [23]. Assuming that, in nanoparticles, reversal is governed by the same mechanism as in magnets, no thermal activation effect may be expected. Alternatively, assuming that reversal occurs by coherent rotation, the coercive energy barrier is 0.5 10^{-15} J, 500 times more than $25k_BT$, the energy provided by thermal activation. Again, no thermal activation may occur. Thermal activation effects are expected to become substantially enhanced with respect to the effects observed in micron-size particles at particle size below 10 δ^3 ($\approx v_{act}$) only.

2.7 Magnetic Characterization

Intrinsic properties refer to the atomic origin of magnetism and involve quantum phenomena such as exchange, crystal-field interaction, interatomic hopping and spin-orbit coupling [24-28]. Intrinsic properties themselves are interesting figures

of merit, but they also affect the hysteresis loop by entering the micromagnetic equations as parameters.

For characterization of intrinsic magnetic properties, various magnetic measurements and analysis have been performed including hysteresis loops, magnetization curves, the law of approach to saturation, the Sucksimith-Thompson method and magnetic viscosity.

2.7.1 Law of Approach to Saturation

It has been experimentally confirmed that ferromagnetic materials follow the law of approach to saturation. Between the low-field Raylegh region and the high-field region near saturation there exists a large section of the magnetization curve, comprising most of the change of magnetization between zero and saturation. The main processes here are large Barkhausen jumps, and the shape of this portion of the magnetization curve varies widely from one kind of specimen to another. In the high-field region, magnetization rotation is the predominant effect, and changes in magnetization with field are relatively small. The relation between M and H in this region is called the "law of approach" to saturation [4] and is written as

$$M = M_S \left(1 - \frac{A}{H^2} - \frac{B}{H^3} - \cdots\right) + \chi \mathrm{H} \qquad (2.23)$$

The term χH represents the field-induced increase in the spontaneous magnetization of the domains, or forced magnetization; this term is usually small at temperatures well below the Curie point and may often be neglected. Constant A is generally interpreted

as due to inclusions and/or micro-stress, and B as due to crystal anisotropy. The constants A and B for uniaxial materials;

$$A = \frac{4}{15}\left(1 + \frac{16}{17}\frac{K_2}{K_1} + \cdots\right)\frac{K_1^2}{M_S^2}$$
$$B = \frac{16}{105}\left(1 + \frac{8}{3}\frac{K_2}{K_1} + \cdots\right)\frac{K_1^3}{M_S^3} \qquad (2.24)$$

where K`s are the principal anisotropy constants. Anisotropy of the system, K_1 and K_2, values can be determined solving equation A and B in eq. (2.24).

2.7.2 Sucksmith-Thompson Method

In some materials, K_2 is negligible and measurements of H_a (Anisotropy Field) are sufficient for the determination of K_1 [29]. A frequently used method to determine both K_1 and K_2 has been developed by Sucksmith and Thompson [30] and is based on the relation:

$$H = \frac{2\,K_1 \sin\theta + 4\,K_3 \sin^3\theta}{M_S} \qquad (2.25)$$

$$\frac{2\,K_1}{M_S^2} + \frac{4\,K_2}{M_S^4}M^2 = \frac{H}{M} \qquad (2.26)$$

which holds for the magnetization curve of a single crystal obtained in comparatively small fields applied perpendicular to the easy direction. Under these circumstances, one may assume that the value of the saturation polarization M_s does not change with field strength and hence $\sin\theta = M/M_S$. Substitution into Eq. (2.25) then leads to Eq.

(2.26). When H/M is plotted versus M^2, the anisotropy constant K_1 in Eq. (2.26) may be derived from the vertical intercept and the anisotropy constant K_2 from the slope of the straight line.

Substantial errors may arise from misalignment when this method is used for determining K_1 and K_2 on aligned powder samples. Misalignment leads to curvature of the magnetization, similar to what would be the effect of a larger value of K_2. Somewhat better in this respect is a method based on the Sucksmith–Thompson plot, as proposed by Ram and Gaunt (1983). In this modification, $H/\alpha\ (M - M_S)$ is plotted versus $\alpha^2(M - M_r)^2$, where M_r is the remanence in the hard direction and where the factor $\alpha = (M_S - M_r)/M_s$ has been introduced to simulate perfect magnetic alignment of the powder particles.

2.7.3 Magnetic Interactions

According to the random anisotropy model [31], overall anisotropy of the system can decrease if there is any exchange interaction occurring in the system. As the anisotropy decreases in the system, the coercivity also decreases.

2.7.3.1 Remanence Curves

In addition to the full hysteresis loop properties of magnetic media, there has been increased interest in the measurement of remanence curves. Measurement of remanence determines the interactions in the system. There are two principle remanence curves; the isothermal remanence (IRM) and the DC demagnetization curve (DCD). The IRM is measured after the application and removal of a field with the sample initially demagnetized. The DCD is measured from the saturated state by

application of increasing demagnetizing fields. According to Stoner-Wohlfarth [21] for non-interacting particles M_{DCD} and M_{IRM} values are related following the formula:

$$M_{DCD}(H) = \left(1 - 2M_{IRM}(H)\right) \tag{2.27}$$

The difference between right and the left side of the equation is defined as δM:

$$\delta\mathrm{M(H)} = M_{DCD}(H) - \left(1 - 2M_{IRM}(H)\right) \tag{2.28}$$

where δM=0 represents the case for no interaction. It has been shown before that δM>0 represents the exchange interaction and δM<0 represents the dipolar interactions [32, 33].

2.7.3.2 Magnetic Viscosity Studies

The time dependence of intrinsic properties such as magnetization, referred to as magnetic viscosity is of utmost importance in the areas of hard and semi-hard magnetism. In most materials it is found experimentally that the magnetization changes over time for a constant applied field such that,

$$M = C_0 + S\, ln(t / t_0) \tag{2.29}$$

where S is the magnetic viscosity coefficient and C_0 is a constant. The phenomenon has been explained due to thermal activation of domain walls and magnetization over activation energy barriers [34,35].

S is related to the activation volume, a concept introduced by Street and Woolley [36]. The activation volume V_{act} [37] can be written in terms of S,

$$V_{act} = \frac{k\,T\chi_{irr}}{M_S\,S} \tag{2.30}$$

Gaunt [38] explained the activation volume as the volume of material that coherently switches which is associated with the magnetization change between the maximum and minimum energy positions of a domain wall or maximum and minimum magnetization orientations in a single domain particle. Therefore, through the viscosity measurements the activation volume of the particle system can be determined. The above derivations are based on the coherent rotation model of Stoner and Wohlfarth [21,39].

2.8 Hard Magnetic Alloys

Due to the Co crisis in 1970`s, quest for Co-free magnet has begun. Not long after, around 1983, Hadjipanayis et. al. and Croat et. al. in GE and Sagawa in Sumitomo metals discovered the Nd-Fe-B magnet and opened a new chapter in magnet history [40, 41]. Rare-earth transition-metal (RE-TM) compounds based on the Nd-Fe-B systems have a very high magnetocrystalline anisotropy (Nd-Fe-B ~ 4.6 10^7 erg/cc at RT) and the highest magnetization among all the hard magnetic materials. Therefore they are very attractive for many advanced technological applications. In the RE-TM intermetallic compounds, the RE (Sm or Nd) unpaired 4f electrons provide the magnetocrystalline anisotropy, which is potentially much stronger than the shape

anisotropy, whereas the TM (Co or Fe) 3d electrons provide most of the magnetization and determine the Curie temperature [42].

The magnitude of the magnetocrystalline anisotropy depends on the ratio of crystal field energy and spin–orbit coupling. As a relativistic phenomenon, spin–orbit coupling is most pronounced for inner-shell electrons in heavy elements, such as rare-earth 4f electrons. This leads to a rigid coupling between spin and orbital moment, and the magnetocrystalline anisotropy is given by the comparatively small electrostatic interaction of the unquenched 4f charge clouds with the crystal field. The dominance of the rare-earth spin orbit coupling ensures an unquenched orbital moment, and the rotational symmetry of the Nd^{3+} charge cloud is an equivalent of the unquenched character of the 3d wave function. Furthermore, the crystal field acting on the 4f electrons is largely screened by rare-earth 5d and 6s electrons. On changing the spin direction, orbital moment and the energy cloud follow the spin, because the crystal field is too weak to break the spin-orbit coupling. However, changing the spin direction modifies the crystal field energy. The negative 4f charges and the negative crystal field charges repel each other and this repulsion is the source of magnetocrystalline anisotropy of rare-earth magnets. In 3d atoms, the spin–orbit coupling $\lambda \approx 50$ meV is much smaller than the crystal-field energy $E_0 \geq 1$ eV, and the magnetic anisotropy is a perturbative effect. For uniaxial symmetry, the anisotropy is of the order of λ^2/E_0, whereas the anisotropy of cubic materials scales as λ^4/E^3_0.

The strength of permanent magnet materials has remarkably increased over the last fifty years [1, 2]. Modern permanent magnets have developed from Alnico's with a maximum energy product $(BH)_{max}$ of 8 - 10 MGOe to the strong Sm-Co magnets [$(BH)_{max}$ of 25-30 MGOe] and Nd-Fe-B "supermagnets" [$(BH)_{max}$ up to 59 MGOe]

[43]. The immediate impact of the $(BH)_{max}$ on the magnet efficiency is based on the fact that for a given magnetic field the volume of the magnet needed for a device is inversely proportional to $(BH)_{max}$. Therefore, for smaller weight and higher efficiency devices high-energy magnets are greatly needed.

RE-TM intermetallics have been the focus of the recent tremendous progress in hard magnetic materials [44-46]. First, the alloys are rich in the late 3d-transition metals (TMs) (Fe or Co), which ensure a high saturation magnetization (M_s) and Curie temperature (T_C). There is usually some trade-off between these two properties; Co alloys tend to have higher T_C but lower M_s. Second, the highly asymmetrical 4f electrons of the REs exhibit a strong spin-orbit coupling (Figure 2.16), which translates into high anisotropies and coercivities in samples with the proper microstructure.

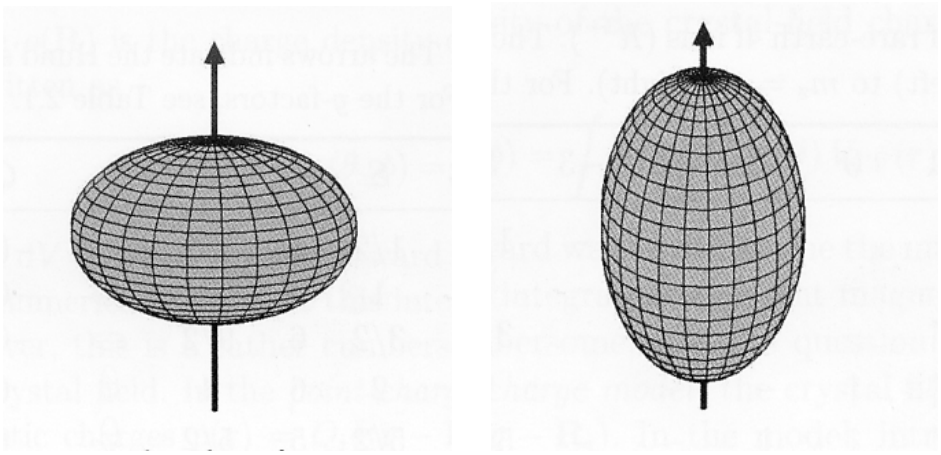

$Ce^{3+}, Pr^{3+}, Nd^{3+}$ $Sm^{3+}, Er^{3+}, Tm^{3+}$

Figure 2.16 Charge distribution of the 4f electron clouds of tripositive rare-earth ions. There are three types: oblate or pancake-like and prolate or cigar-like.

2.8.1 The Rare-Earth Magnet Family

The newest and still growing family of hard magnetic alloys includes the well-known samarium- cobalt and neodymium- iron- boron magnets, but also many other related materials (Figure 2.17). All are based on intermetallic compounds formed when 3d- transition metals **(**TM**)**, notably the strongly magnetic Co and Fe, are alloyed with rare-earth elements **(**RE**)** of the 4f- transition series, i.e., the "lanthanides" Ce, Pr, Nd, Sm, Gd, Dy [47, 48]. A large number of such binary and ternary intermetallics are ferro- or ferrimagnetic, and at least 50 combine a substantial saturation magnetization, $\mathbf{B_s}$, with a sufficiently high Curie point, $\mathbf{T_c}$, to possibly qualify them for some magnetic application. Several combine these features with a very large single- easy-axis magnetocrystalline anisotropy, which makes them potential permanent magnet materials [49]. Three subgroups in particular— the compound types RE-Co`s, RE_2Co_7 and $RE_2Fe_{14}B$ — were thoroughly studied and a few members of these have been developed into useful permanent magnets [50].

Table 2.1 lists the current high performance magnets together with the intrinsic/hard magnetic properties of the particular intermetallic compound. All of these magnets have one thing in common: their hard magnetic properties arise from the fundamental properties of their major constituent compound. The $(BH)_{max}$ limits set by the intrinsic properties of these compounds have been nearly reached $(BH)_{max}$. As seen in Table 2.1, the maximum $(BH)_m$ achieved so far experimentally is 59 MGOe in Nd-Fe-B magnets.

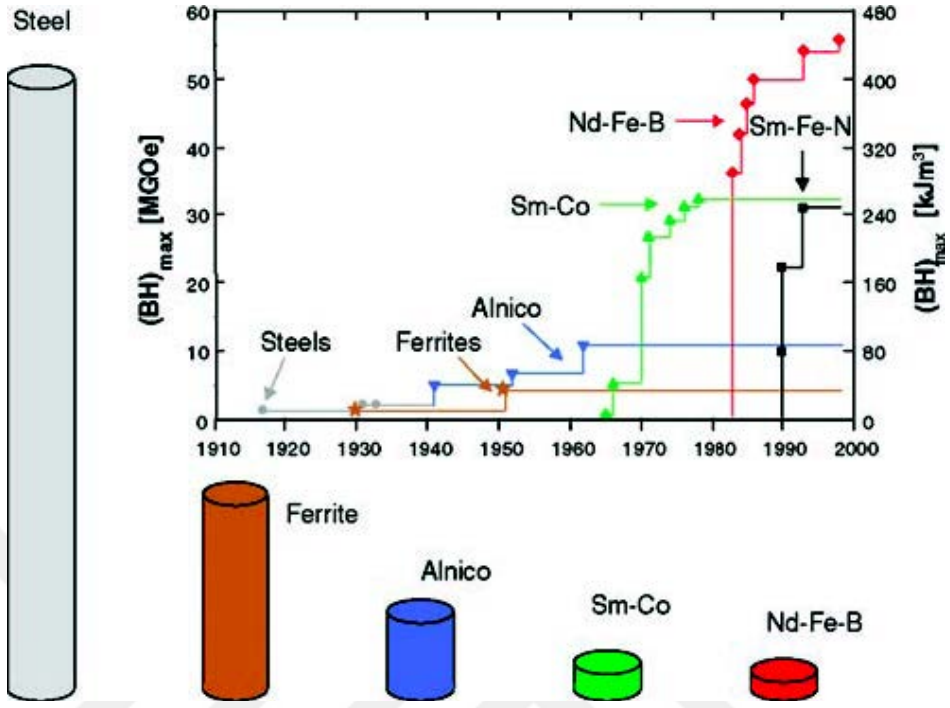

Figure 2.17 Current market of rare earth permanent magnets [51].

2.8.1.1 Neodymium-iron-boron Magnets

The most powerful permanent magnets presently available consist essentially of the tetragonal $Fe_{14}Nd_2B$ phase with tetragonal structure (Figure 2.18). The $Fe_{14}Nd_2B$ phase is formed with all rare earth (RE) elements with the exception of Eu. Their intrinsic properties have been investigated extensively. Neodymium shows the highest permanent magnet potential based on its combination of high values of $\mathbf{K}_1$ and $\mathbf{M}_s$. The intrinsic magnetic properties of the Co_5RE and $Co_{17}RE_2$ phases are summarized in Table 2.1.

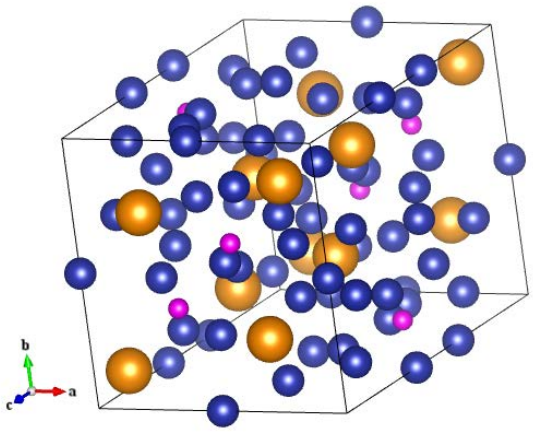

Figure 2.18 Crystal structure of $Nd_2Fe_{14}B$ phase (Balls; yellow: Nd, blue: Fe, Pink: B).

2.8.1.2 Samarium-cobalt Magnets

Numerous magnetic, binary, rare earth (RE) transition metal (TM) compounds exist, of which the Co_5RE and $Co_{17}RE_2$ phases form the basis for materials with excellent permanent magnetic properties. They combine high saturation magnetization $\mathbf{M}_s$ with high crystal anisotropy $\mathbf{K}_1$ and high Curie temperature $\mathbf{T}_c$. The intrinsic magnetic properties of the Co_5RE and $Co_{17}RE_2$ phases are summarized in Table 2.1 (Co_5RE and $Co_{17}RE_2$ are, also, referred to as 5/1 and 17/2 phases). It is obvious that Co_5Sm with hexagonal $CaCu_5$ structure (Figure 2.19 (a)) and $Co_{17}Sm_2$ with rhombohedral Th_2Zn_{17} structure (Figure 2.19 (b)) have the best potential for manufacturing permanent magnetic materials.

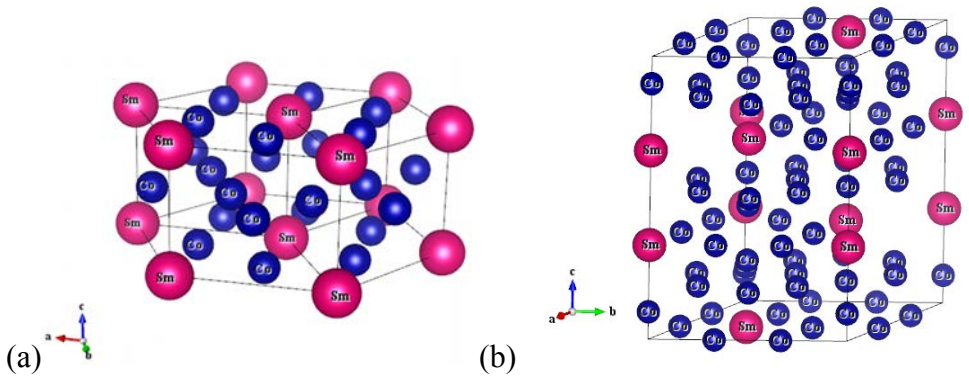

Figure 2.19 Crystal structure of (a) $SmCo_5$ with hexagonal $CaCu_5$ structure, and (b) Sm_2Co_{17} with rhombohedral Th_2Zn_{17} structure.

2.8.1.3 Neodymium-Cobalt Alloys

$RECo_5$ intermetallics possess strong magnetocrystalline anisotropies and high Curie temperatures, which predestine them for the use as permanent magnets in the case of a uniaxial orientation of the easy magnetization direction. $NdCo_5$ has a hexagonal $CaCu_5$ structure with the c-axis as the easy direction of magnetization above 290 K. Below this temperature the moments rotate, in the *ac* plane, and below 245 K the a-axis in the basal plane becomes the easy-axis. The reason for this behavior is that in rare-earth intermetallics, both the RE and Co sublattices contribute to the total magneto-crystalline anisotropy and in some cases the different temperature dependencies of these contributions lead to a change in the easy direction of magnetization with temperature. In $NdCo_5$, the Nd sublattice favors a planar anisotropy at low temperature, whereas the Co sublattice has uniaxial anisotropy, which dominates at high temperature [52,53].

Table 2.1 Fundamental magnetic properties of selected hard magnetic compounds together with the corresponding theoretical limits of $(BH)_{max}$ and the highest values reported to date (values in parenthesis).

Compound	Saturation magnetization (kG)	Anisotropy field (kOe)	Curie temperature (°C)	Theoretical $(BH)_{max}$ (MGOe)
$Nd_2Fe_{14}B$	16.0	67	312	64.0 (59)
$Sm_2Fe_{17}N_{2.3}$	15.4	140	476	59.3 (47)
$Sm_2(Co,Fe,Cu,Zr)_{17}$	12.5	65	920	39.1 (33)
$SmCo_5$	11	≤ 440	681	30.2 (25)
$PrCo_5$	12.3	≥ 145	620	37.8

REFERENCES

1. William D. Callister, Jr., Materials Science and Engineering: An Introduction, 7th Edition, John Wiley & Sons., Inc., New York, 2007.

2. W. Weber, Springer Proceedings in Physics, 2010, Volume 133, 1-41.

3. http://perso.neel.cnrs.fr/olivier.fruchart/slides/

4. Cullity B D 1972 Introduction to Magnetic Materials (Reading, MA, USA: Addison-Wesley).

5. S. Chikazumi, Physics of Ferromagnetism (Oxford University Press, New York, 1999).

6. R. C. O´Handley, Modern Magnetic Materials: Principles and applications. (John Wiley & Sons, 2000).

7. M. Farle *Rep. Prog. Phys.* 61, 755 (1998).

8. Edward P. Furlani Permanent Magnet and Electromechanical Devices: Materials, Analysis, and Applications Academic Press 2001.

9. http://www.irm.umn.edu/hg2m/hg2m_c/hg2m_c.html

10. http://magician.ucsd.edu/essentials/WebBookse20.html

11. J. M. D. Coey, "Permanent Magnetism", Solid State Communications, 102, 101 (1997).

12. Jales D. Introduction to Magnetism and Magnetic Materials; CRC Press, Boca Raton, FL, (1998).

13. W. D. Kingery, H. K. Bowen, and D. R. Uhlmann, Introduction to Ceramics, 2nd Ed., John Wiley &. Sons, Inc., New York 1976.

14. D. J. Sellmyer, R. Skomski Advanced Magnetic Nanostructures Springer New York 2006.

15. M. P. Morales, S. Veintemillas-Verdaguer, M. I. Montero and C. Serna *J. Chem. Mater.* 11, 3058 (1999).

16. M. P. Morales, C. J. Serna, F. Bødker and S. Mørup *J. Phys.: Condens. Matter* 9, 5461 (1997).

17. Y. Liu, D. J. Sellmyer and D. Shindo Handbook of Advanced Magnetic Materials vol 2, 2006 Springer New York.

18. R. Skomski and J. M. D. Coey. Permanent Magnetism. Institute of Physics, Bristol (1999).

19. S. Rivoirard and D. Givord Advanced Magnetic Nanostructures Ch. 12 Springer New York 2006.

20. A. Aharoni An Introduction to the Theory of Ferromagnetism. Oxford University Press. London (1996).

21. E. C. F. R. S. Stoner, E. P. Wohlfarht, *Phil. Trans. R. Soc. A* 1948, *240*, 599.

22. W. Wernsdorfer, E. Bonet Orozco, K. Hasselbach, A. Benoit, B. Barbara, N. Demoncy, A. Loiseau, H. Pascard, and D. Mailly *Phys. Rev. Lett.* 78, 1791 (1997).

23. D. Givord, A. Lienard, P. Tenaud, and T. Viadieu *J. Magn. Magn. Mat.* 67, L281 (1987).

24. E. Ising *Z. Phys.* 31, 253 (1925).

25. W. Heisenberg *Z. Phys.* 49, 619 (1928).

26. F. Bloch *Z. Phys.* 57, 545 (1929).

27. H. Brooks *Phys. Rev.* 58, 909 (1940).

28. J. C. Slater *Rev. Mod. Phys.* 25, 199 (1953).

29. K. H. J. Buschow And F. R. De Boer Physics Of Magnetism And Magnetic Materials Ch. 11 Kluwer Academic Publishers New York, Boston, Dordrecht, London, Moscow 2003.

30. W. Sucksmith and J. E. Thompson *Proc. Roy. Soc. London* A225, 362 (1954).

31. G. Herzer, *IEEE Trans. Magn. 26*, 1397 (1990).

32. R. Alben, J. J. Becker and M. C. Chi *J. Appl. Phys. 49*, 1653 (1978).

33. R. W. Chantrell, K. O'Grady, *Appl. Magn. 253*, 113 (1994).

34. K. O'Grady, R. W. Chantrell, Proceedings of the International Workshop on Studies of Magnetic Properties of Fine Particles 93 (1992).

35. L. Neel *J. Phys. Rad.* 11, 40 (1959).

36. R. Street, J.C. Woolley and P.B. Smith *Proc. Phys. Soc. B* 65, 679 (1952).

37. E. P. Wohlfarth *J. Phys. F: Met. Phys.* 14, 1155 (1984).

38. P. Gaunt *J. Appl. Phys.* 59, 4129 (1986).

39. A. Lyberatos and R. Chantrell *J. Phys. D: Appl. Phys.* 29, 2332 (1996).

40. G. C. Hadjipanayis and R. C. Hazelton *Appl. Phys. Lett.* 43, 797 (1983).

41. J. J. Croat, J. F. Herbst, R. W. Lee and F. E. Pinkerton *Appl. Phys. Lett.* 44, 148 (1984).

42. R. Skomski, Simple Models of Magnetism Oxford University Press, USA (March 15, 2008).

43. R. Skomski, J.M.D. Coey, in: *Permanent magnetism*, Taylor francis Group LLC (1996).

44. K. Kumar *J. Appl. Phys.*63, R13 (1988).

45. J. F. Herbst *Rev. Mod. Phys.*63, 819 (1991).

46. R. Skomski and J.M.D. Coey *Phys. Rev. B*48, 15812 (1993)

47. W. E. Wallace; Rare Earth Intermetallics, Part 3, p. 112, New York, NY: Academic Press, 1973.

48. K. H. J. Buschow Volume 1, Chapter 4, p. 297.

49. K. J. Strnat *IEEE Transactions on Magnetics* 8, 511 (1972).

50. K. J. Strnat *IEEE Transactions on Magnetics* 23, 2094 (1987).

51. O. Gutfleisch, M. A. Willard, E. Brück, C. H. Chen, S. G. Sankar and J. P. Liu *Adv. Mater.* 23, 821 (2011).

52. G. Asti, F. Bolzoni, D. Melville and S. Rinaldi *IEEE Transactions on Magnetics* Mag-11 (1975).

53. W. G. D. Frederick, C. W. Searle and M. Hoch, *Magn. Magn. Mater. Nineteenth Annual Conference* 18, 1197 (1974).

Chapter 3

SAMPLE PREPARETION & CHARACTERIZATION METHODS

3.1 Particle Preparation

Stoichiometric alloys were prepared by arc-melting in argon using pure metals. All constituent elements of 99.9 at% purity were melted together in a water-cooled copper crucible of the arc-melt. The chamber of the arc-melt system was flashed with pure argon several times. The melting was done at a constant argon pressure. Pulverizing techniques included crushing the homogenized alloys, grinding down to 200 μm and milling with a SPEX-8000 mill.

3.1.1 Physics of Ball Milling

Fundamentally, the term milling may be referred to as the breaking down of relatively coarse materials to the ultimate fineness. Ball milling techniques use mechanical energy to crush powder or to activate structural changes, which include disordering, amorphization and compositional changes.

Shaker mills such as SPEX mills (Figure 3.1 (a)), which mill about 10±20 g of the powder at a time, are most commonly used for laboratory investigations and for alloy screening purposes [1]. These mills are manufactured by SPEX CertPrep, Metuchen, NJ. The common variety of the mill has one vial, containing the sample and grinding balls, secured in the clamp and swung energetically back and forth several thousand times a minute. The back-and-forth shaking motion is combined with lateral movements of the ends of the vial. With each swing of the vial the balls impact

against the sample and the end of the vial, both milling and mixing the sample. Whenever two balls collide with or a ball collides with a wall of vial, some amount of powder is trapped in between them. Because of the amplitude (about 5 cm) and speed (about 1200 rpm) of the clamp motion, the ball velocities are high (on the order of 5 m/s) and consequently the force of the ball's impact is unusually great. The force of the impact plastically deforms the powder particles, leading to work hardening and facture. Therefore, these mills can be considered as of high-energy variety. The most recent design of the mills has provision for simultaneously milling the powder in two vials to increase the throughput. This machine incorporates forced cooling to permit extended milling times. A variety of vial materials is available for the SPEX mills and these include hardened steel, alumina, tungsten carbide, zirconia, stainless steel, silicon nitride, agate, plastic, and methacrylate. A typical example of a tungsten carbide vial, gasket and grinding balls for the SPEX mill is shown in Figure 3.1 (b).

Typically, in dry ball milling the new surface created enables the particles to weld together, and this leads to an increase in particle size. The process involves repeated flattening, cold welding, fracturing, and the re-welding of powder particles in a controlled atmosphere (usually an inert medium).

The ratio of the weight of balls to powder (BPR), sometimes referred to as charge ratio (CR), is an important variable in the milling process. This has been varied by different investigators from a value as low as 1:1 [2] to as high as 220:1 [3]. Generally speaking, a ratio of 10:1 is most commonly used while milling the powder in a small capacity mill such as a SPEX mill. The BPR has a significant effect on the time required to achieve a particular phase in the powder being milled. The higher the BPR, the shorter is the time required.

The major effect of the milling atmosphere is on the contamination of the powder. Traditionally, the powders are milled in containers that have been either evacuated or filled with an inert gas such as argon or helium.

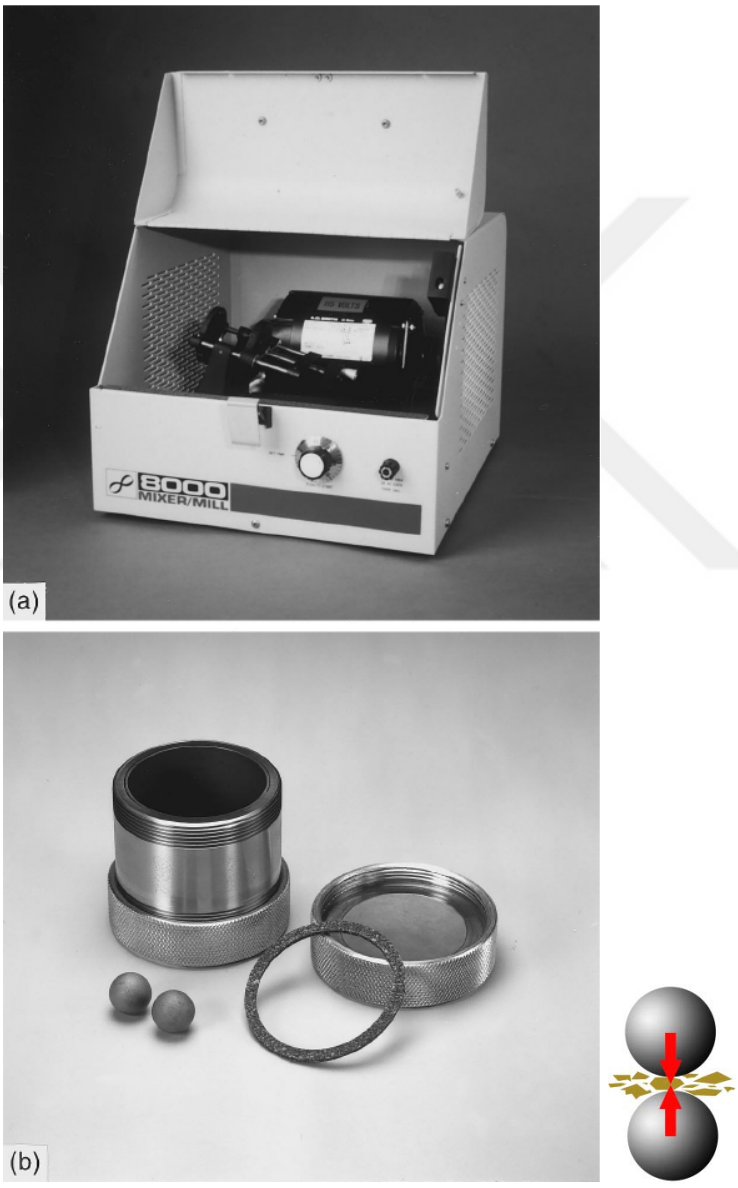

Figure 3.1 (a) SPEX 8000 mixer/mill in the assembled condition. (b) Tungsten carbide vial set consisting of the vial, lid, gasket, and balls.

3.1.2 Function of Process Control Agents (Surfactants) in Ball Milling

Typically, in dry ball milling, the powder particles get cold-welded to each other, as the new surface created, and this leads to an increase in particle size. A process control agent (PCA) (also referred to as lubricant or surfactant) is added to the powder mixture during milling to reduce the effect of cold welding. The PCAs can be solids, liquids, or gases. They are mostly organic compounds, which act as surface-active agents. The PCA is adsorbed on the surface of the powder particles and minimizes cold welding between powder particles and thereby inhibits agglomeration. The surface-active agents adsorbed on the particle surfaces interfere with cold welding and lower the surface tension of the solid material. A wide range of PCAs has been used in practice at a level of about 1±20 wt% of the total powder charge. The nature and quantity of the PCA used and the type of powder milled would determine the final size, shape, and purity of the powder particles.

It should be realized that there is no universal PCA. The amount of the PCA is dependent upon the (a) cold welding characteristics of the powder particles, (b) chemical and thermal stability of the PCA, and (c) the amount of the powder and grinding medium used. The powder particle size tends to increase if the weight proportion of the PCA to the powder is below a critical value, while above this value the particle size tends to decrease. One has to decide on a PCA by looking at the possible interactions between the metal and the components in the PCA.

3.1.3 Ball Milling of RE-TM Compounds

Ball milling is a versatile technique and has been successful to produce a large range of nanoscaled materials, including nanocrystaline structures, nanoparticles, and nanocomposites. In this dissertation thesis, RE-TM nanoparticles and nanosize-thick

flakes were prepared by subjecting the brittle arc-melted alloys to a successive wet and surfactant-assisted high energy ball milling (SA-HEBM).

3.1.3.1 Surfactant-Assisted Ball Milling

RE-TM based powders, which are prepared by arc-melting, were used in our experiments. Powders were first crushed down to 200 μm in a mortar. The organic solvent heptane (99.8% purity) was used as the milling medium, and different type of surfactants were used during milling. The powders were placed in a milling jar with different size carbon-steel balls by using a SPEX 8000M high-energy ball-milling machine.

Different type of surfactants such as; OA (90%) (Oleic acid), OY (oleylamine), TOP (>98%) (trioctylphosphine), TOA (>98%) (trioctylamine) and octanoic acid (Figure 3.2) have been used in high energy ball milling.

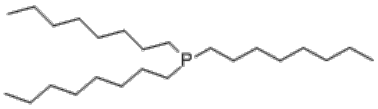

TOP

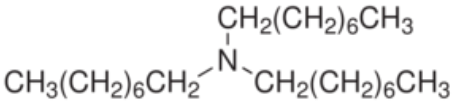

TOA

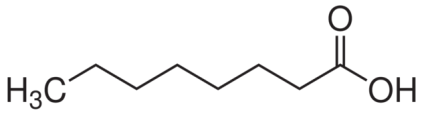

OCTANOIC

OY

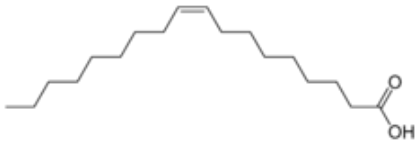

OA

Figure 3.2 Molecular structures of surfactants.

The ball-to-powder weight ratio used was 10:1. Heptane (99.8%) was used as the compatible milling medium.

In this work, the first step in HEBM is milling the powders in heptane without the presence of surfactants. At the end of the first step, the color of the liquid medium did not change (Figure 3.3 (a)), indicating that there was no dispersion of particles in the heptane. In the second stage, the surfactants are added to the milling vial, which is filled with heptane.

During the milling process, as soon as the particles and/or fresh surfaces are formed, surfactants are absorbed on to the surface of the particles by the formation of the chemical bonds, which prevents agglomeration (The tail portions (R) of the surfactants repel each other) (Figure 3.3 (b)). This greatly reduces cold welding and the re-welding of crushed particles, which finally allows the separated particles with smaller sizes to be formed. Therefore, after the SA-HEBM, a black-colored liquid containing a dispersion of nanoparticles was observed along with coarse micron size particles and/or flakes (slurry particles), which immediately settled down at the bottom of the milling vial.

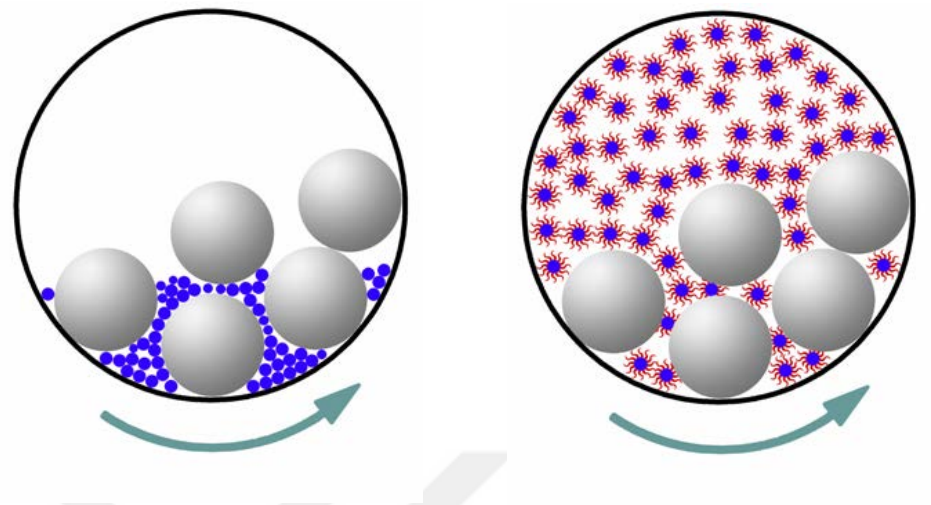

Figure 3.3 Milling vial (a) First step, wet milling in heptane, and (b) SA-HEBM.

3.2 Sample Characterization

3.2.1 Vibrating Sample Magnetometer (VSM)

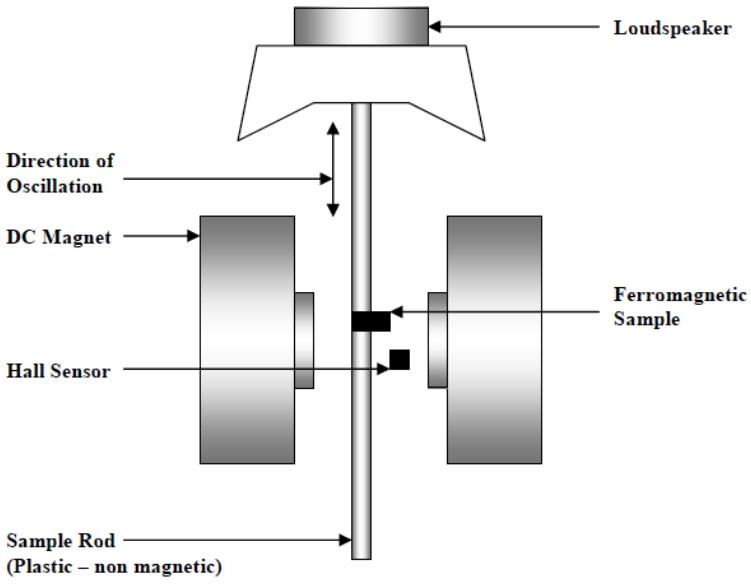

Figure 3.4 Schematic representation of a VSM [4].

Vibrating Sample Magnetometry (VSM) is based on Faraday's law of induction, which states that an electromagnetic force is generated in a coil when there is a change in flux linking the coil and a changing magnetic field will produce an electric field [4]. In the measurement setup, a magnetic sample is moving in the proximity of two pickup coils as indicated in Figure 3.4. This electric field can be measured and can tell us information about the changing magnetic field.

The oscillator provides a sinusoidal signal that is translated by the transducer assembly into a vertical vibration. The sample which is fixed to the sample rod vibrates with a given frequency and amplitude (60 Hz and ~1 mm, respectively). It is centered between the two pole pieces of an electromagnet that generates a magnetic field $\overrightarrow{H_0}$ of high homogeneity. Field strengths of several Tesla are commonly possible with laboratory VSM systems. Stationary pickup coils are mounted on the poles of the electromagnet. Their symmetry center coincides with the magnetic center of the sample. Hence, the change in magnetic flux originating from the vertical movement of the magnetized sample induces a voltage U_{ind} in the coils. $\overrightarrow{H_0}$, being constant, has no affect on the voltage but is necessary only for magnetizing the sample. According to Faraday the voltage in a single winding of the pickup coil can be written as $U_{ind} = -\frac{\partial \Phi}{\partial t}$, where Φ is the magnetic flux.

If the sample is magnetic, constant magnetic field will magnetize the sample by aligning the magnetic domains, or the individual magnetic spins, with the field. The stronger the constant field, the larger the magnetization will be. The magnetic dipole moment of the sample will create a magnetic field around the sample; sometimes align the magnetic stray field. As the sample is moved up and down, this magnetic stray field is changing as a function of time and can be sensed by a set of pick-up coils

(Figure 3.4). The alternating magnetic field will cause an electric current in the pick-up coils according to Faraday's Law of Induction. This current will be proportional to the magnetization of the sample. The greater the magnetization, the greater is the induced current.

In this work, we used a Quantum Design`s VersaLab VSM for the measurements.

3.2.2 Superconducting Quantum Interference Device (SQUID)

The SQUID magnetometer is based on the same principle as the VSM but with a superconducting pickup coil circuit and a superconducting quantum interference device (SQUID) as the flux detector. The structure of a SQUID magnetometer is schematically shown in Figure 3.5.

This device is based on the tunneling of superconducting electrons across a very narrow insulating gap, called a Josephson junction [6], between two superconductors. A sketch of the device in its usual form is shown in Figure 3.6. A superconducting measuring current flows through the ring, so that equal currents pass through each of two Josephson junctions. A changing magnetic flux through the ring generates a voltage and a current in the ring, according to Faraday's Law. This induced current adds to the measuring current in one junction, and subtracts in the other. Because of the wave nature of the superconducting current, the result is a periodic appearance of resistance in the superconducting circuit, and the appearance of a voltage between points A and B. Each voltage step corresponds to the passage of a single flux quantum across the boundary of the ring. The existence of the flux quantum was demonstrated in somewhat similar experiments on superconducting rings; its value is $h/2e = 2.07\times10^{-15}$ weber or Tm^2, or 2.07×10^{-7} maxwell or

gauss cm^2. This sensitivity is rarely needed in a measurement of magnetic field, and in practice the device is most commonly linked to a coil to measure the flux from a small sample, and thus the sample magnetization. In this form it is called a **SQUID** (for **superconducting quantum interference device**) **magnetometer**. Since a superconducting Josephson device requires low-temperature operation, it is usually used in conjunction with a superconducting solenoid.

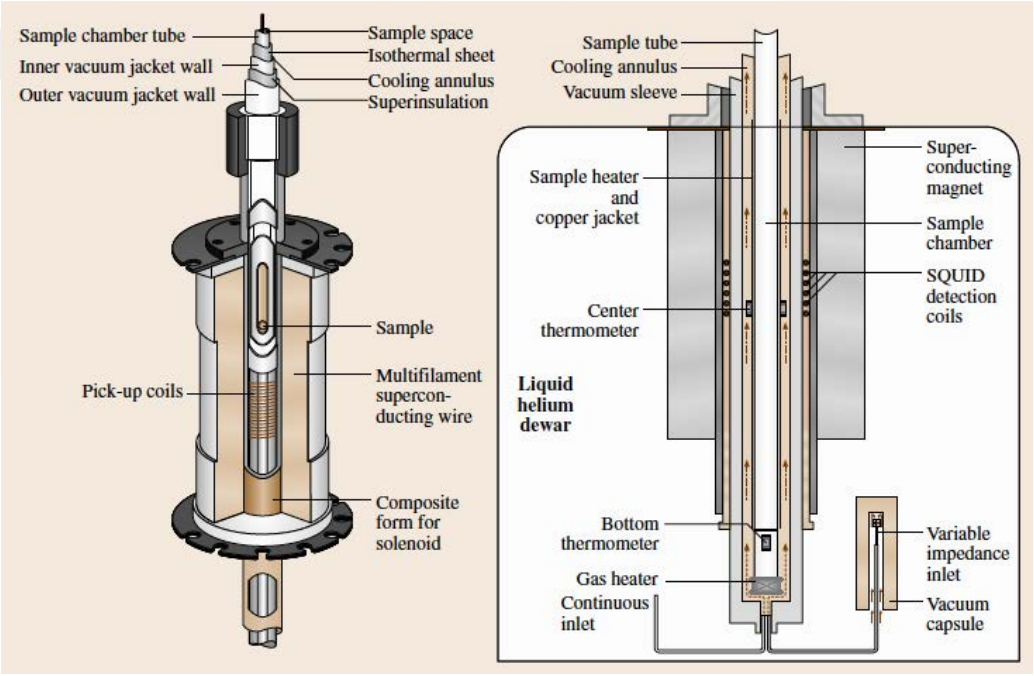

Figure 3.5 Schematic view of a SQUID magnetometer consisting of a liquid-He cryostat, a superconducting magnet, the variable-temperature sample chamber and the detection coils close to the sample position [5].

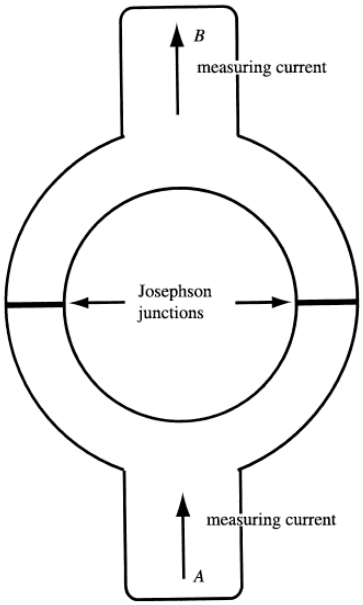

Figure 3.6 SQUID (superconducting quantum interference device) flux sensor [7].

3.2.2.1 AC Measurements

AC magnetic measurements were performed by Physical Property Measurement System (PPMS). In AC magnetic measurements, a small AC drive magnetic field is superimposed on the DC field, causing a time-dependent moment in the sample. The field of the time-dependent moment induces a current in the pickup coils, allowing measurement without sample motion. The detection circuitry is configured to detect only in a narrow frequency band, normally at the fundamental frequency (that of the AC drive field). In order to understand what is measured in AC magnetometry, first consider first the case of very low frequencies, where the measurement is most similar to DC magnetometry. In this case, the magnetic moment of the sample follows the M(H) curve that would be measured in a DC experiment. As long as the AC field is small, the induced AC moment is $M_{AC} = (dM/dH) \cdot H_{AC}$ sin(ωt) where H_{AC} is the amplitude of the driving field, ω is the driving frequency, and

$\chi = dM/dH$ is the slope of the M(H) curve, called the susceptibility. The susceptibility is the quantity of interest in AC magnetometry.

At higher frequencies than those considered above, the AC moment of the sample does not follow the DC magnetization curve due to dynamic effects in the sample. For this reason, the AC susceptibility is often known as the dynamic susceptibility. In this higher frequency case, the magnetization of the sample may lag behind the drive field, an effect that is detected by the magnetometer circuitry. Thus, the AC magnetic susceptibility measurement yields two quantities: the magnitude of the susceptibility, χ, and the phase shift, ϕ (relative to the drive signal). Alternately, one can think of the susceptibility as having an in-phase, or real, component χ' and an out-of-phase, or imaginary, component χ''. The two representations are related by

$$\begin{aligned} \chi' &= \chi \cos\varphi \\ \chi'' &= \chi \sin\varphi \end{aligned} \quad \Leftrightarrow \quad \begin{aligned} \chi &= \sqrt{\chi'^2 + \chi''^2} \\ \varphi &= \arctan(\chi''/\chi') \end{aligned} \tag{3.1}$$

3.2.3 X-Ray Diffractometer (XRD)

X-rays are electromagnetic radiation with typical photon energies in the range of 100 eV - 100 keV. For diffraction applications, only short wavelength x-rays (hard x-rays) in the range of a few angstroms to 0.1 angstrom (1 keV - 120 keV) are used. Because the wavelength of x-rays is comparable to the size of atoms, they are ideally suited for probing the structural arrangement of atoms and molecules in a wide range of materials. The energetic x-rays can penetrate deep into the materials and provide information about the bulk structure.

X-rays are produced generally by either x-ray tubes or synchrotron radiation. In a x-ray tube, which is the primary x-ray source used in laboratory x-ray instruments, x-rays are generated when a focused electron beam accelerated across a high voltage field bombards a stationary or rotating solid target. As electrons collide with atoms in the target and slow down, a continuous spectrum of x-rays are emitted, which are termed Bremsstrahlung radiation. The high energy electrons also eject inner shell electrons in atoms through the ionization process. When a free electron fills the shell, an x-ray photon with energy characteristic of the target material is emitted.

X-rays primarily interact with electrons in atoms. When x-ray photons collide with electrons, some photons from the incident beam will be deflected away from the direction where they originally travel, much like billiard balls bouncing off one anther. If the wavelength of these scattered x-rays did not change (meaning that x-ray photons did not lose any energy), the process is called elastic scattering (Thompson Scattering) in that only *momentum* has been transferred in the scattering process. *These are the x-rays that we measure in diffraction experiments, as the scattered x-rays carry information about the electron distribution in materials.* On the other hand, in the inelastic scattering process (Compton Scattering), x-rays transfer some of their energy to the electrons and the scattered x-rays will have different wavelength than the incident x-rays.

Diffracted waves from different atoms can interfere with each other and the resultant intensity distribution is strongly modulated by this interaction. If the atoms are arranged in a periodic fashion, as in crystals, the diffracted waves will consist of sharp interference maxima (peaks) with the same symmetry as in the distribution of

atoms. Measuring the diffraction pattern therefore allows us to deduce the distribution of atoms in a material.

The peaks in an x-ray diffraction pattern are directly related to the atomic distances. Let us consider an incident x-ray beam interacting with the atoms arranged in a periodic manner. The atoms, represented as green spheres in Figure 3.7, can be viewed as forming different sets of planes in the crystal. For a given set of lattice planes with an inter-plane distance of d, the condition for a diffraction (peak) to occur can be simply written as

$$2d \sin\theta = n\,\lambda \qquad (3.2)$$

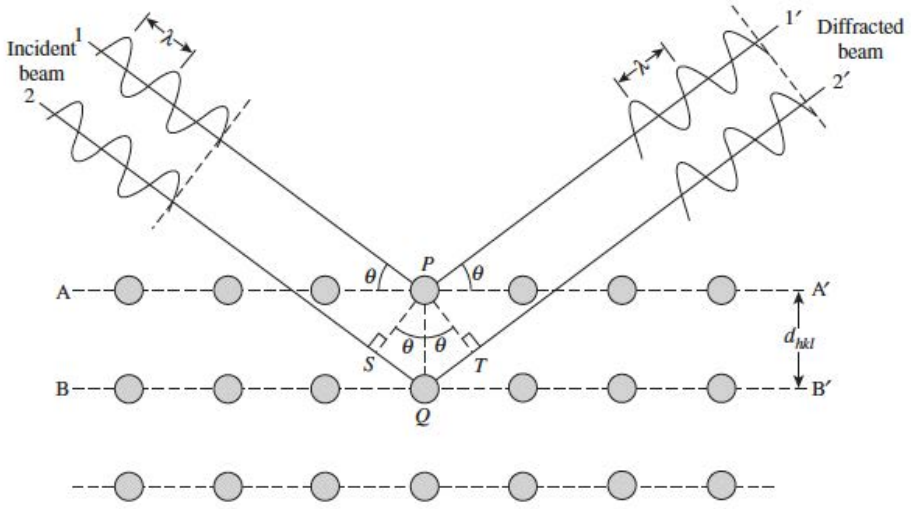

Figure 3.7 Diffraction geometry.

which is known as the Bragg's law [7], after W.L. Bragg, who first proposed it in 1918. In the eq. (3.2), λ is the wavelength of the x-ray, θ the scattering angle, and n an integer representing the order of the diffraction peak. The Bragg's Law is one of most important laws used for interpreting x-ray diffraction data.

It is important to point out that although we have used atoms as scattering points in this example, Bragg's Law applies to scattering centers consisting of any periodic distribution of electron density. In other words, the law holds true if the atoms are replaced by molecules or collections of molecules, such as colloids, polymers, proteins and virus particles.

Powder Diffraction

Powder XRD (X-ray Diffraction) is perhaps the most widely used x-ray diffraction technique for characterizing materials. As the name suggests, the sample is usually in a powdery form, consisting of fine grains of single crystalline material to be studied. The technique is used also widely for studying particles in liquid suspensions or polycrystalline solids (bulk or thin film materials).

The term 'powder' really means that the crystalline domains are randomly oriented in the sample. Therefore when the 2-D diffraction pattern is recorded, it shows concentric rings of scattering peaks corresponding to the various d spacings in the crystal lattice. The positions and the intensities of the peaks are used for identifying the underlying structure (or phase) of the material.

Powder diffraction data can be collected using reflection geometry, as shown in Figure 3.8. Because the particles in the powder sample are randomly oriented, these two methods will yield the same data.

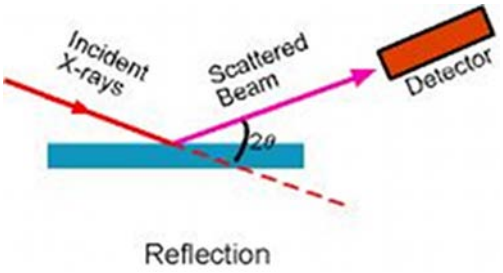

Figure 3.8 Reflection.

Strain and finite size of crystallites causes a broadening of the diffraction peaks. If strain assumed to be negligible the relation follows as,

$$t = \frac{0.9\,\lambda}{B\,\cos\theta_B} \tag{3.3}$$

which is known as the Scherrer formula calculated from the full width at half maximum (FWHM) of the peak (B). It is used to estimate the particle size of very small crystals from the measured width of their diffraction curves. Previous work suggests that the broadening is produced by either lattice strains alone, or by lattice strains and small particle size simultaneously. Williamson and Hall [8] showed that there is another broadening that needs to be taken in to account, which comes from the strain. This broadening can be defined as;

$$\beta_S = 2\xi \tan\theta \tag{3.4}$$

where ξ is the strain distribution. Total broadening combined with the Scherrer's formula becomes,

$$\beta = \left(2\xi + {}^{2d}/_{t}\right)\tan\theta \qquad (3.5)$$

In this work, we used the Rigaku Ultima IV diffractometer, which uses CuK_α ($\lambda = 1.5405$ Å) radiation.

3.2.4 Transmission Electron Microscopy (TEM)

Transmission electron microscopy utilizes the wave properties of electrons to generate highly resolved images of specimens. In 1986 the Nobel Prize in physics was awarded by one half to Ernst Ruska for his fundamental work in electron optics, and for the design of the first electron microscope (EM), and by one half to Gerd Binnig and Heinrich Rohrer for their design of the scanning tunneling microscope. In some aspects operation of a transmission electron microscope (TEM) is comparable with that of a slide projector (Figure 3.9): electrons from the electron gun pass through condenser lenses that focus the electrons onto the sample. The electron beam shines through the specimen. Objective lenses and projector lenses magnify the transmitted beam and project it onto the fluorescent viewing screen. Impact of electrons excites the screen and produces a visible magnified image of the sample. This image is recorded with various detectors, such as a CCD camera [9].

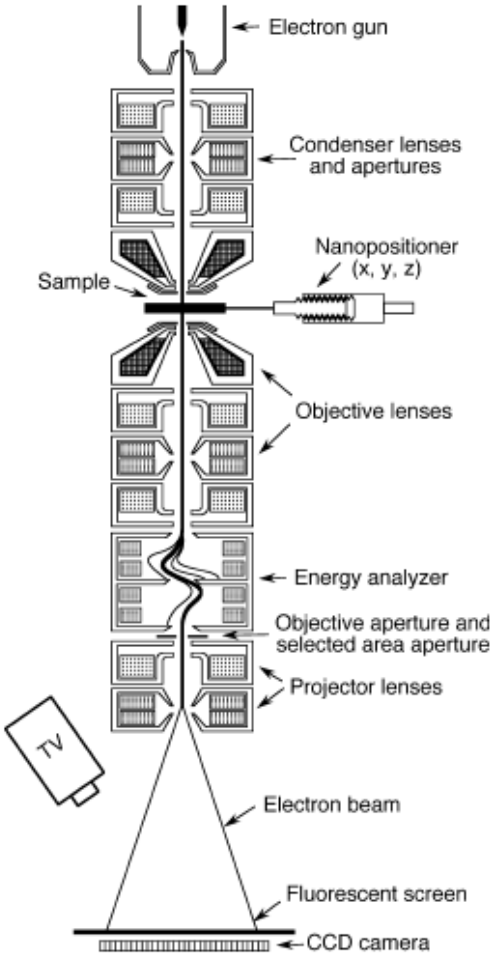

Figure 3.9 Schematic representation of a TEM system [9].

The sample is placed in front of the objective lens in the form of thin foil, thin section or fine particles which are transparent to the electron beam (Figure 3.10). The objective lens forms an image of the electron density distribution at the exit surface of the specimen based on the electron optical principles. A diffraction pattern is formed in the back focal plane of the objective lens and the recombination of the diffracted beams forms an image in the image plane of the objective lens. The diffraction,

projection and intermediate lenses below the objective lens are used to focus and magnify either the diffraction pattern or the image onto a fluorescent screen, which converts the electrons into visible light signal.

The transmission electron microscope may be operated to produce either a diffraction pattern from a specific region of the specimen or one of several types of images, where quantitative information about the microstructure of the material is required, and a detailed correlation is made between the diffraction pattern and the image.

The essential features of the diffraction and image modes of operation can be explained in terms of a geometric optics treatment at the objective lens. Figure 3.10 shows an electron beam parallel to the optic axis and incident upon the specimen. The action of forming the image brings both the transmitted and the diffracted beam to a focus in the back focal plane of the objective lens. Thus a diffraction pattern is produced here. Because both a diffraction pattern and an image of the specimen are always produced by the objective lens, a magnified image of either may be produced on the viewing screen by focusing the next lens in the magnification system on one or the other. When we focus the diffraction lens at the image plane of the objective lens and introduce an aperture in the back focal plane of the objective lens an image of the sample is produced on the screen. The differential scattering and absorption of electrons creates intensity variations at the exit surface of the sample and these variations are magnified and imaged on the fluorescent screen by the lens system.

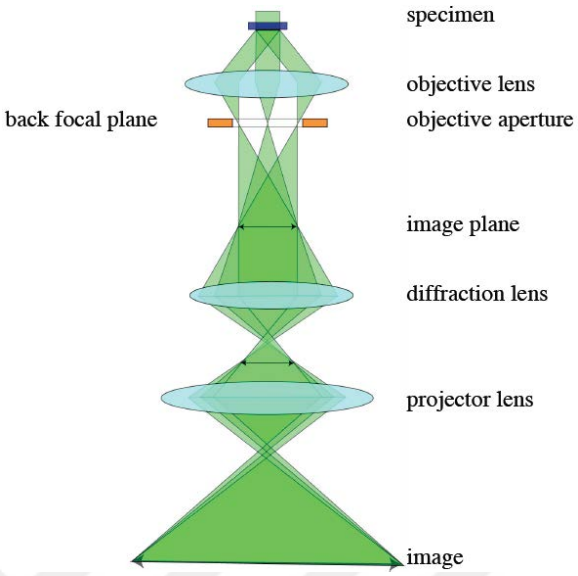

Figure 3.10 Scheme of the image formation mechanism in TEM [10].

3.2.5 Scanning Electron Microscopy (SEM) and Energy Dispersive Spectroscopy (EDS)

In an optical microscope, we image features in the samples either by passing light through them in the transmission mode or by reflecting light from the surface in the reflection mode. The SEM is a reflection instrument but with some significant differences from a light microscope. Electrons interact with the specimen with a variety of different mechanisms producing a complex set of signals. These signals include backscattered electrons, secondary electrons, Auger electrons and characteristic X-rays (Figure 3.11).

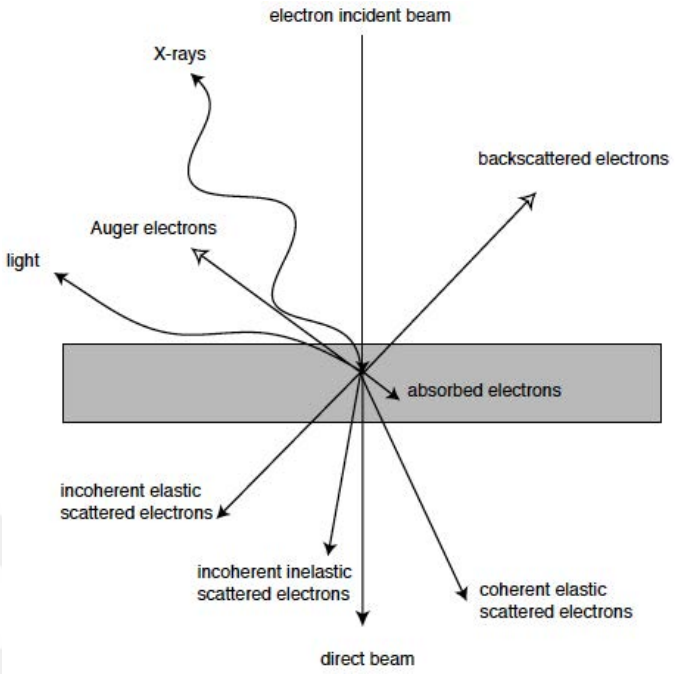

Figure 3.11 Interactions between electrons and material [11].

The SEM forms an image by sweeping an electron beam across the surface of the specimen and coupling that e-beam raster with the raster of a cathode ray tube, LCD, or plasma screen. Figure 3.12 shows a schematic drawing of the major elements of the image formation in the SEM. The signal from the detector is then used to adjust the intensity of the corresponding pixel of the screen. Naturally more signal leads to more intensity on the screen and the image is built up bit-by-bit in a back and forth, raster pattern. In the SEM, a reasonably well-focused electron beam is produced and directed down the column to the specimen. In order to manipulate the electron beam and minimize interactions, the column must be at high vacuum. The beam is finely focused by an electromagnetic or electrostatic lens and a series of apertures.

This beam is swept across the surface of the specimen using deflection-scanning coils. The signal from specimen is collected and used to moderate the intensity of an accompanying monitor. The beam deflection coils are connected to and synchronized with the output monitor [12].

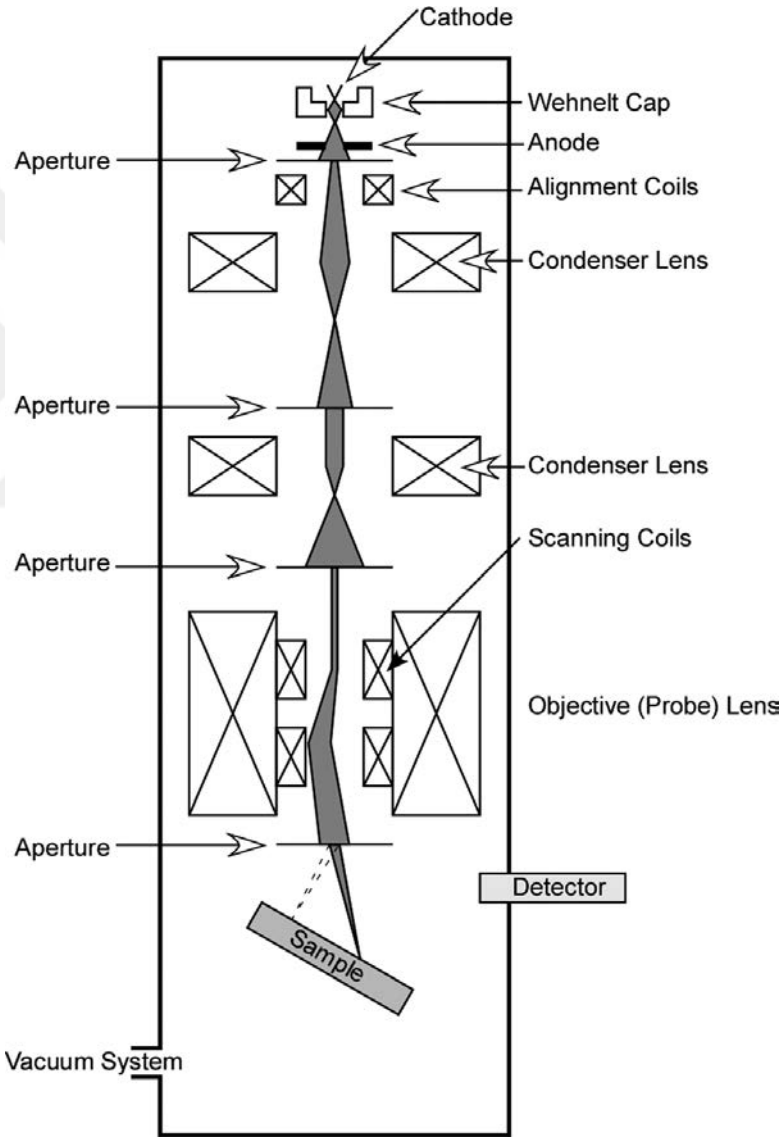

Figure 3.12 Inside schematic of SEM [13].

Energy Dispersive X-Ray Spectrometry (EDS)

EDS makes use of the X-ray spectrum emitted by a solid sample bombarded with a focused beam of electrons to obtain a localized chemical analysis. All elements from atomic number 4 (Be) to 92 (U) can be detected in principle, though not all instruments are equipped for 'light' elements ($Z < 10$). Qualitative analysis involves the identification of the lines in the spectrum and is fairly straightforward owing to the simplicity of X-ray spectra. Quantitative analysis (determination of the concentrations of the elements present) entails measuring line intensities for each element in the sample and for the same elements in calibration standards of known composition [14].

By scanning the beam in a television-like raster and displaying the intensity of a selected X-ray line, element distribution images or 'maps' can be produced. Also, images produced by electrons collected from the sample reveal surface topography or mean atomic number differences according to the mode selected. The scanning electron microscope (SEM), which is closely related to the electron probe, is designed primarily for producing electron images, but can also be used for element mapping, and even point analysis, if an X-ray spectrometer is added. Schematic representation of the EDS detector can be seen from Figure 3.13.

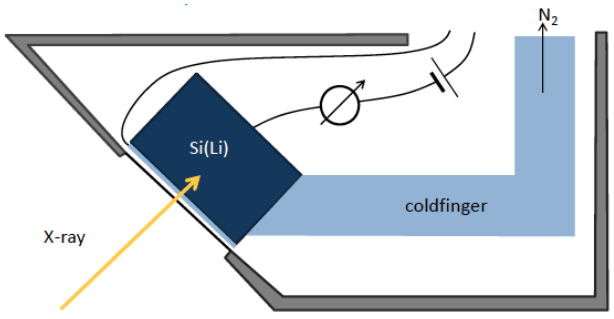

Figure 3.13 Schematic of the EDS detector.

3.2.6 Fourier Transform Infrared Spectrometry

FT-IR stands for Fourier Transform InfraRed, the preferred method of infrared spectroscopy. In infrared spectroscopy, IR radiation is passed through a sample. Some of the infrared radiation is absorbed by the sample and some of it is passed through (transmitted) (Figure 3.14). The resulting spectrum represents the molecular absorption and transmission, creating a molecular fingerprint of the sample. Like a fingerprint no two unique molecular structures produce the same infrared spectrum. An infrared spectrum represents a fingerprint of a sample with absorption peaks, which correspond to the frequencies of vibrations between the bonds of the atoms making up the material. Because each different material is a unique combination of atoms, no two compounds produce the exact same infrared spectrum. Therefore, infrared spectroscopy can result in a positive identification (qualitative analysis) of every different kind of material [15].

The normal instrumental process is as follows:

1. **The Source:** Infrared energy is emitted from a glowing black-body source. This beam passes through an aperture, which controls the amount of energy presented to the sample (and, ultimately, to the detector).

2. **The Interferometer:** The beam enters the interferometer where the "spectral encoding" takes place. The resulting interferogram signal then exits the interferometer.

3. **The Sample:** The beam enters the sample compartment where it is transmitted through or reflected off of the surface of the sample, depending on the type of analysis being accomplished. This is where specific frequencies of energy, which are uniquely characteristic of the sample, are absorbed.

4. **The Detector:** The beam finally passes to the detector for final measurement. The detectors used are specially designed to measure the special interferogram signal.

5. **The Computer:** The measured signal is digitized and sent to the computer where the Fourier transformation takes place. The final infrared spectrum is then presented to the user for interpretation and any further manipulation.

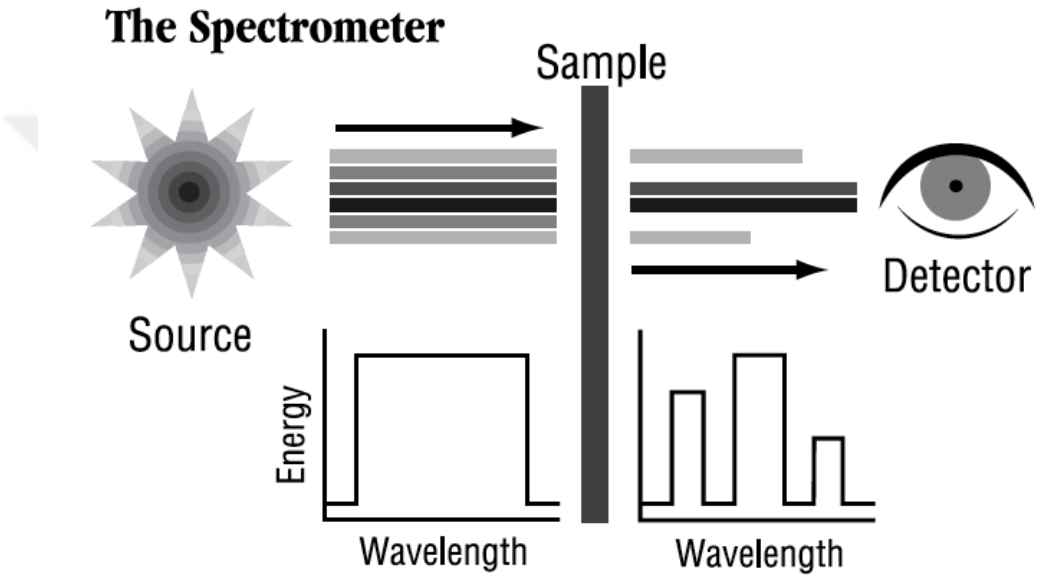

Figure 3.14 A schematic of an FTIR spectroscopy.

REFERENCES

1. C. Suryanarayana *Prog. Mater. Sci.* 46, 184 (2001).
2. Z. H. Chin, T. P. Perng *Mater Sci Forum* 235-238, 121 (1997).
3. V. Kis, D. L. Beke *Mater Sci Forum* 225-227, 465 (1996).
4. K.H.J. Buschow and F.R. de Boer Physics of Magnetism and Magnetic Materials. Kluwer Academic/Plenum Publishers, 2003.
5. H. Czichos, T. Saito, L. E. Smith, Springer handbook of metallurgy of Testing, Springer NY 2011.
6. B. D. Josephson *Phys. Lett.* 1, 251 (1962).
7. Cullity B D 1972 Introduction to Magnetic Materials (Reading, MA, USA: Addison-Wesley).
8. G. K. Williamson and W. H. Hall *Acta Metalurgica* 1, (1953).
9. B. Nolting, Methods in Modern Biophysics Ch. 6 Springer-Verlag Berlin Heidelberg 2009.
10. http://micron.ucr.edu/public/manuals/Tem-intro.pdf
11. http://cbe.ivic.ve/mic250/pdf/thesebook-chap3.pdf
12. R. A. Carlton, Pharmaceutical Microscopy, Springer NY 2011.
13. G. Dehm, J. M. Howe and J. Zweck. In-situ Electron Microscopy: Applications in Physics, Chemistry and Materials Science, First Edition. 2012 Wiley-VCH.
14. http://micron.ucr.edu/public/manuals/EDS-intro.pdf
15. http://www.wcaslab.com/tech/tbftir.htm

Chapter 4

FABRICATION OF NANOPARTICLES AND NANOFLAKES

4.1 Introduction

Recent years saw an increasing demand for even finer permanent magnet powders based on the rare earth - transition metal (RE-TM) compounds. Alongside with the industrial need for hard magnetic materials such as Nd-Fe-B and Sm-Co alloys, currently, there has been a great scientific interest in the study of the fundamental properties as a function of particle size including systems such as $Nd_2(Fe,Mn)_{14}B$ and $NdCo_5$ which shows complex magnetic ordering behavior at different temperatures.

The efforts in this section have been focused on the fabrication and characterization of nanoflakes and nanoparticles using the novel method of SA-HEBM. The challenge is to control the particle/grain size with a uniform size distribution, and to synthesize them with good crystallinity and superior magnetic properties.

4.2 Experimental Details

Synthesis

Stoichiometric 2:14:1, 1:5 and 2:17 alloys were prepared by arc-melting in argon using pure metals. Nd-(Fe,Mn)-B was also prepared with the stoichiometric composition, $Nd_2Fe_{11}Mn_3B$. The alloys prior to mechanical alloying were

homogenized at 1000^{o}C for 12 h. Pulverizing techniques included crushing the homogenized alloys, grinding down to 200 μm and then subject them to high energy ball milling (HEBM) with a SPEX- 8000 mill. High-energy ball milling experiments were performed in a milling vial with carbon-steel balls. In wet milling, cold welding and the re-welding of particles can be prevented by using surfactants along with milling media during milling. Ball milling is a complex process that involves the optimization of a number of variables to achieve the desired product phase or structure. Some of the important parameters that have an effect on the final constitution of the powders are: (1) milling time, (2) the size, and size distribution of the grinding medium (balls), ball to powder ratio, (3) the milling atmosphere, and (4) the process control agent (milling media).

The balls-to-powders weight ratio used was 10:1. Heptane (99.8%) was used as the milling medium and oleic acid (OA) (90%) as the surfactant. The amount of surfactant employed was 9-15 wt % of the starting powder. The effect of different milling conditions has been discussed in section 4.9. As discussed in Chapter 3, a two-stage SA-HEBM is a powerful technique, which allows us to obtain compounds with different microstructures and control their shape and size.

In this chapter, a variety of RE-TM compounds have been used for the synthesis of flakes with different aspect ratios and nanoparticles with different size. The effects of the experimental parameters on the microstructure and any relationship between final flake nanoparticle microstructure with the grain size of the precursor powder are discussed. Investigation of how the magnetic and fundamental properties (M_s, K, T_c, T_{sr}) are influenced by size/surface effects will be presented in Chapter 5 and 6.

Characterization

The surface chemistry of the particles was studied by Fourier transform infrared spectroscopy (FTIR) with a Thermo Nicolet Nexus 670 instrument. The structure and morphology of the powders were characterized by transmission electron microscopy (TEM) with a JEOL JEM-3010 instrument, scanning electron microscopy (SEM) with a JEOL JSM-6335F instrument, and x-ray diffraction (XRD) with Rigaku Ultima IV operating with a Cu-K$\boldsymbol{\alpha}$ radiation. The XRD data were processed with a Powder Cell program [1]; the crystallite size and microstrain were estimated from the broadening of the XRD peaks using the Williamson-Hall plots [2] after correcting the XRD data for K_2 contribution and instrumental broadening. Room temperature magnetic properties were measured with a vibrating sample magnetometer on field-aligned powder samples embedded into wax in the presence of a 19 kOe orienting field. AC susceptibility measurements were performed by a Physical Property Measurement System (PPMS).

4.3 $Nd_2Fe_{14}B$ Nanoflakes and Nanoparticles

4.3.1 Formation Mechanism and Structural Studies

As discussed in chapter 3, high-energy ball milling is a non-equilibrium process, which involves repeated welding, fracturing and re-welding of powder particles. As-crushed ingot has a wide size distribution with particles below 200 μ (Figure 4.1).

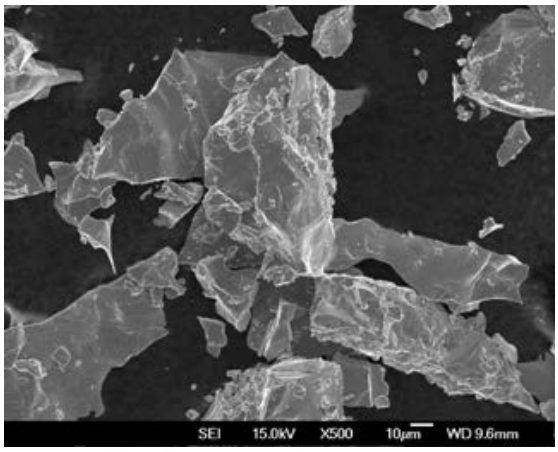

Figure 4.1 SEM image of as-crushed powders.

A two-step HEBM was used to prepare both the nanoparticles and the nanoflakes. In the first step the coarse powders were brought into the nanocrystalline state by using HEBM in heptane without the presence of surfactants. In the second step, the addition of surfactant (Oleic acid, OA) facilitated the formation of nanoparticles. Polarity (the dielectric constant) of the liquid environment is known to be among the most important factors influencing the milling process [3]. The dispersibility of certain ceramic powders increases and their agglomeration decreases with increasing the dielectric constant of the surrounding liquid [4]. This plays a crucial role in producing the powders in the form of flakes.

Wet milling in heptane has been used in order to bring the coarse powders into the nanocrystalline state. As mentioned in section 3.1.2, wet milling is more advantageous method as compared to traditional dry milling in argon, and this is due to the fact that wet milling slows down the milling, decreases the number of collisions and in turn preserves the crystalline structure of the powders longer. Figure 4.2 shows the particles, under the same experimental conditions, after (a) dry-milling under

argon and (b) wet-milling in heptane solvent. In the case of dry milling, the particles agglomerate severely (grain size = 5 nm, using the Williamson-hall plots), whereas the liquid environment decreases particle agglomeration significantly (grain size = 20 nm, using the Williamson-hall plots) [5, 6].

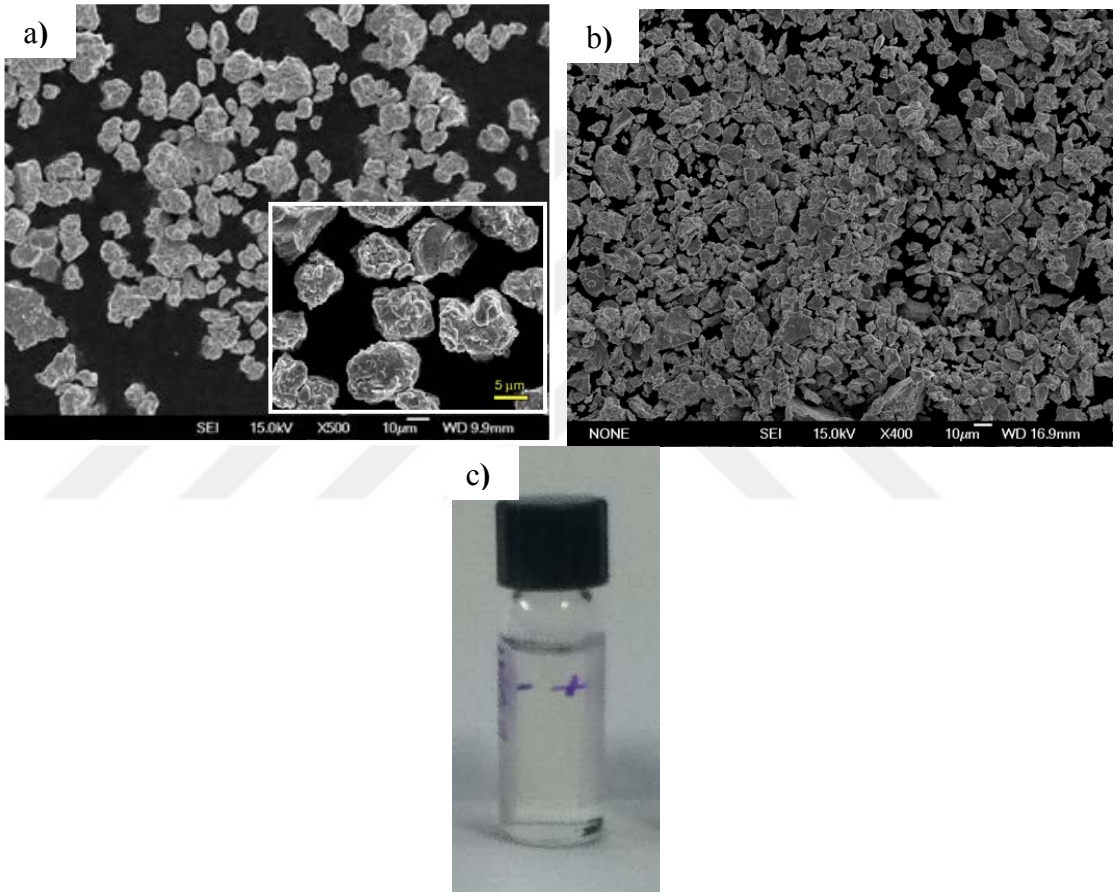

Figure 4.2 Particles in slurry (a) dry-milled under argon, (b) wet-milled in heptane and (c) powders in heptane after milling.

Judging from the magnetic properties, during dry milling, the changes in the grain structure and particle morphology occur approximately at a rate six times the

rate for surfactant-free wet milling (Figure 4.3). The increase in M_r, which is an indication that grain size is approaching to the values comparable to the effective exchange length (hysteresis loops are corrected for self-demagnetizing field), occurs after 20 min for dry-milled powders whereas it starts increasing only after 120 min for wet-milled powders (heptane) (Figure 4.3). Therefore, we can conclude that the liquid environment in milling procedure decreases the number of collision hence it slows down the milling energetically [5].

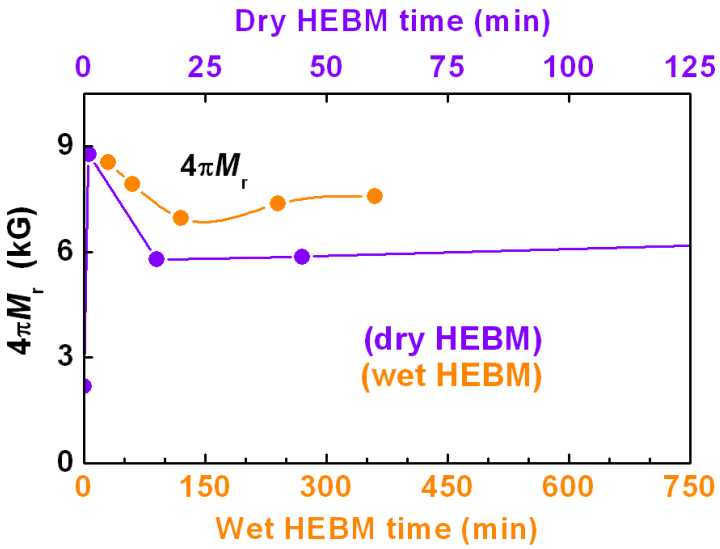

Figure 4.3 Particles in slurry (a) dry-milled under argon and (b) wet-milled in heptane.

As shown in Figure 4.2 (c), after wet milling in heptane the slurry with micron size particles sediments at the bottom of the milling vial. Figure 4.4 shows the powders in the slurry milled in heptane from 15 min to 4 h. Particles have been obtained with different grain sizes (Table 2.1) down to around 20 nm (calculated using

Williamson-hall plots) after 4 h of milling. The polycrystallinity during milling is being induced via coalescence of the particles and/or via formation of new (sub)grains [7-10]. As milling continues, average particle size does not change much but the size distribution gets narrower (Figure 4.5).

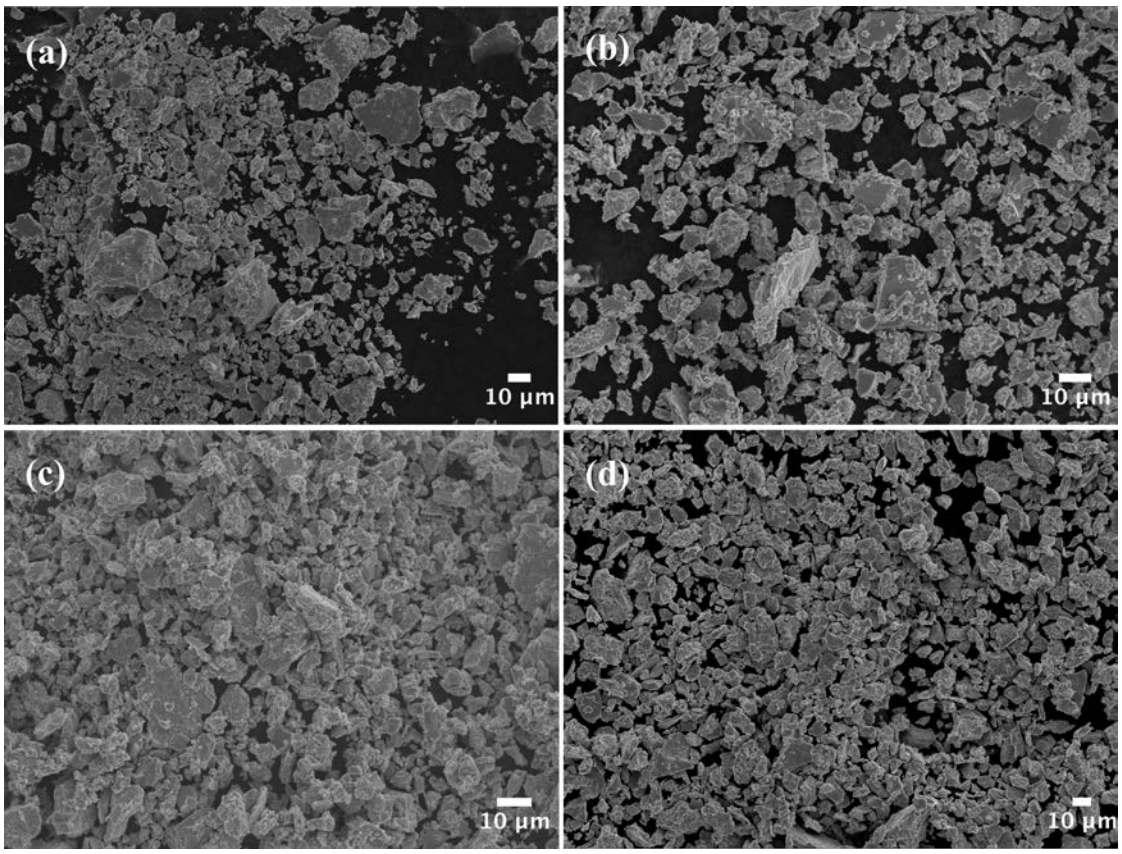

Figure 4.4 SEM image of $Nd_2Fe_{14}B$ powders wet-milled (step 1) in heptane (a) 15 min, (b) 1 h, (c) 2 h and (d) 4 h.

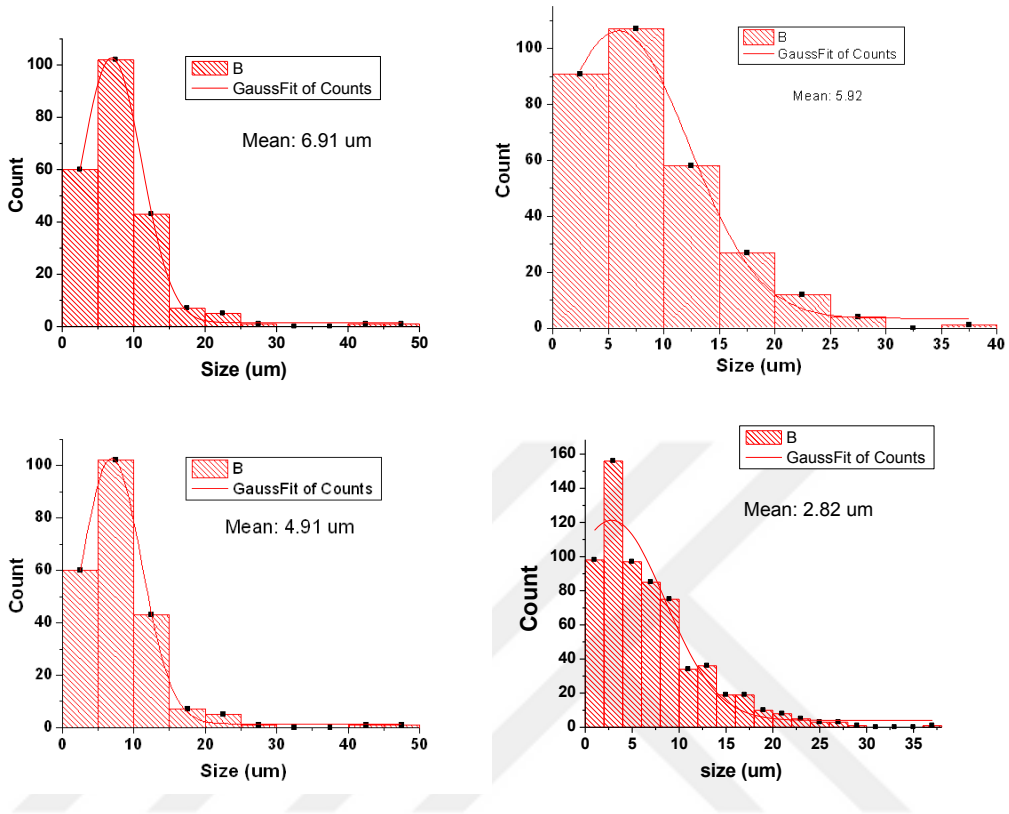

Figure 4.5 Corresponding size distributions of $Nd_2Fe_{14}B$ powders wet-milled in heptane (a) 15 min, (b) 1 h, (c) 2 h and (d) 4 h.

Wet milling of the precursor led to SA-HEBM powders consisting of uniform flakes. The mechanism responsible for the unusual formation of the nanoflakes by the SA-HEBM is based on the following known effects. It has been suggested [11] that the mechanical properties of nanocrystalline materials prepared by mechanical attrition are no longer controlled by dislocation movement through the crystals but by cohesion across the grain boundaries. Intercrystalline regions which were believed to be formed in the HEBM [11] must greatly facilitate grain-boundary sliding. The plasticity of nominally brittle materials increases in their nanocrystalline state due to grain boundary sliding (the shear modulus of the grain-boundary regions is expected

to decrease by about 40% when the volume fraction of the grain boundaries becomes comparable to that of the crystals [12-14]). Moreover, the impediment of cold welding is efficient in a liquid milling environment, especially in the presence of appropriate surfactants.

The typical morphology of these flakes is shown in Figure 4.6 after the two-step HEBM (SA-HEBM for 6 h). The slurry contains some nanoparticles but mostly micron long $Nd_2Fe_{14}B$ flakes with different thicknesses (Figure 4.6). As the wet milling (step 1) time was increased, nanocrystalline powders with smaller crystallite size were obtained which led to a decrease in the average thickness of the flakes down to below 100 nm with an aspect ratio as high as 10^2 - 10^3 (Figure 4.6).

The flakes must have evolved from the "dense" assembled particles like the one shown in Figure 4.4 (d). The rough estimate of average volume of the precursor particles (150 μm^3) is reasonably close to the volume of the typical flake (e.g., 30 μm × 25 μm × 0.2 μm), indicating that little, if any, coalescence or breaking of the particles had taken place during the SA-HEBM. Thus, the evolution of particle shape for the nominally brittle RE-TM alloys subjected to SA-HEBM after prolonged wet milling (1^{st} step) is similar to that of ductile materials [13,14]. This result is perfectly consistent with the above model of nanostructure-induced ductility. It should be noted, however, that unlike at least some of the truly ductile materials, which reportedly may evolve into flakes while being wet-milled without added surfactants [13,14], the nanocrystalline RE-TM powders milled in heptane *without* OA do not contain any flakes (Figure 4.4).

The data suggest that there is a strong correlation between the milling of precursors (grain size) with the thickness of the flakes. We have investigated the

evolution of powder morphology with milling time. Keeping the SA-HEBM time constant at 6 h, the pre-milling time has been changed from 15 min to 4 h. Since SA-HEBM time was kept constant, as seen in Figure 4.7, there is a direct effect of pre-milling time on the thickness of the flakes. When the precursor powders were subjected to 6 h of SA-HEBM, the thickness was found to decrease from above 500 nm to below 100 nm (Figure 4.7).

Table 4.1 summarizes the change in flake thickness and lateral size distribution. As seen in the table, the size distribution of precursor powder and the lateral size distribution of the flakes are in good agreement. As the size distribution of precursor powder gets narrower, the lateral size of the flakes gets narrower as well, which is consistent with the above discussion on the formation of flakes from the nanocrystalline structure.

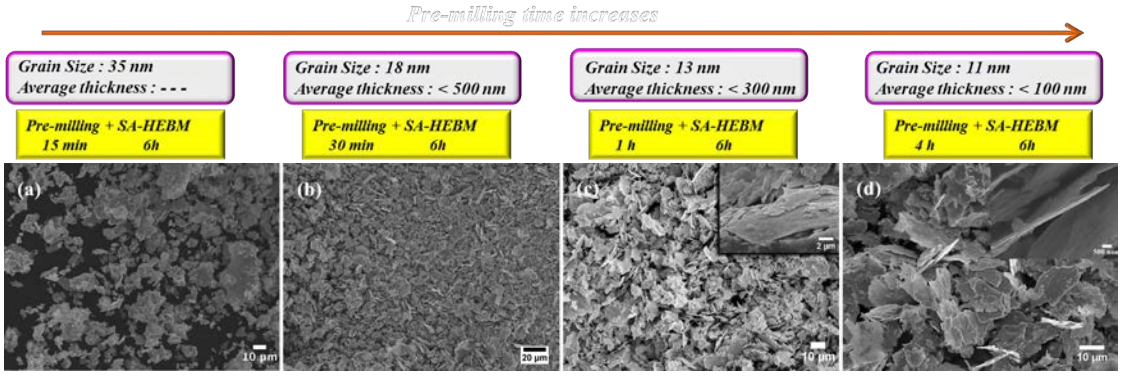

Figure 4.6 SEM image of $Nd_2Fe_{14}B$ nano-flakes wet-milled in heptane for (a) 15 min milling, (b) 30 min, (c) 1h and (d) 4h (all followed by 6 h of SA-HEBM).

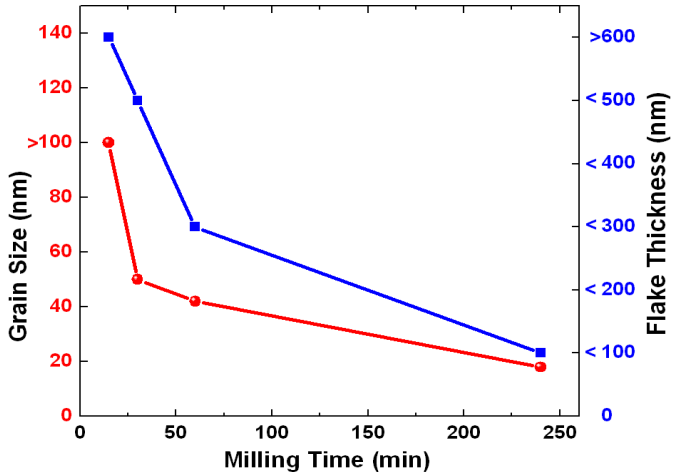

Figure 4.7 The change in grain size of the precursor powder and corresponding flake thicknesses with milling.

Figure 4.8 shows the XRD patterns of $Nd_2Fe_{14}B$ powders of different crystallite sizes obtained after wet milling for up to 4 h. The as-made ingot exhibits the single tetragonal $Nd_2Fe_{14}B$ structure (Figure 4.8 (a)). As expected the results show that the diffraction peaks broaden with decreasing particle size, which indicates that crystallite/grain size is decreasing. After 4 h of wet milling, an average crystallite size of 18 nm was found using Williamson-Hall method (which uses the Scherrer's formula) (Table 4.1).

XRD characterization of the $Nd_2Fe_{14}B$ pre-milled powders after subsequent SA-HEBM for 6 h, is presented in figure 4.9. It can be seen that no peaks from oxides or pure iron, are present in the diffraction patterns, indicating that the prepared powders have been effectively protected. The diffraction patterns also confirm that no detectable contamination or decomposition in the particles has occurred during the milling process. The crystallite size of the flakes is found to decrease from 35 to 11 nm. The values of the microstrain determined were very small, 0.36% - 0.3%, for the

initial 4 h and additional 6 h of milling. Table 4.1 summarizes the change in particle and grain sizes of the powders and the flakes with milling.

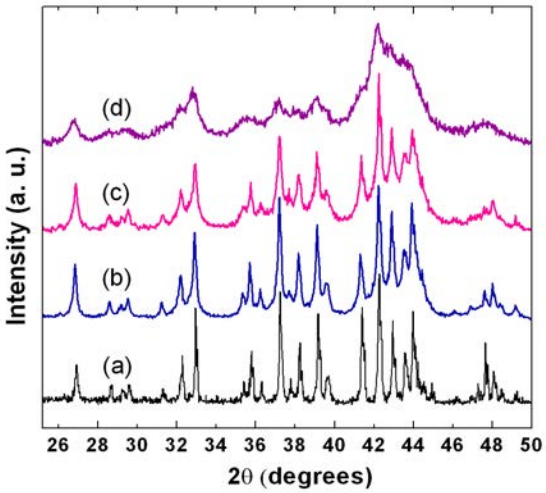

Figure 4.8 X-ray diffraction data for $Nd_2Fe_{14}B$ alloy which was homogenized (a) and milled in heptane for 30 min (b), 1 h (c) and 4 h (d).

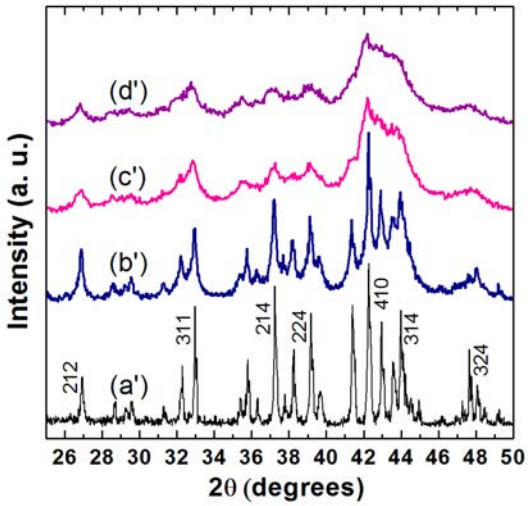

Figure 4.9 X-ray diffraction data for $Nd_2Fe_{14}B$ alloy, which was homogenized (a') and milled in heptane for 30 min followed by SA-HEBM (6 h) (b'), 1 h followed by SA-HEBM (6 h) (c') and 4 h followed by SA-HEBM (6 h) (d').

Table 4.1 Effect of different experimental conditions on the flake thickness/grain size/particle size.

Milling Media	Pre-Milling Time	Particle Size Micron	Grain Size (nm)	Type of Surfactant	Surfactant Wt. (%)	OA Milling Time	Flake Thickness (nm)	Grain Size of flakes (nm)	Size Distribution
Heptane	15 min	1 to 50	---	OA	15	6 h	Very Thick	35 nm	Very Wide
Heptane	30 min	1 to 30	> 50 nm	OA	15	6 h	<500	18	Wide
						12 h	<100	9 nm	Wide
Heptane	1 h	3 to 25	42 nm	OA	15	6 h	< 300	13 nm	Wide
Heptane	2 h	3 to 20	30 nm	OA	15	6 h	<200	12 nm	Narrow
Heptane	4 h	5 to 20	18 nm	OA	15	6 h	<100	11 nm	Very Narrow

In order to investigate the microstructure further, HRTEM (high resolution TEM) was performed to probe the morphology and microstructure of nanoflakes (4h wet + 6h SA-HEBM). Figure 4.10 shows the in-plane HRTEM image of the flakes. The average grain size we observed in the ion milled (thinned) flakes is around 24 nm. The grain size directly observed from TEM micrograph images is in good agreement with the average size estimated from XRD patterns (with grain size of 18 nm calculated using Williamson-Hall method).

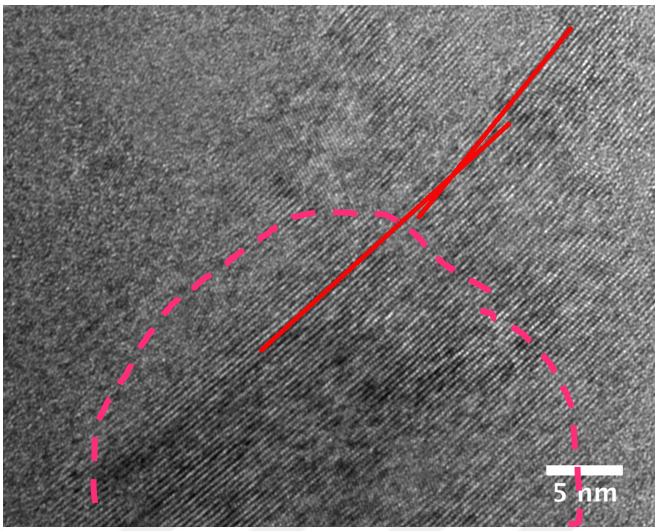

Figure 4.10 HRTEM image of (4h wet-milled + 6h SA-HEBM) the flakes.

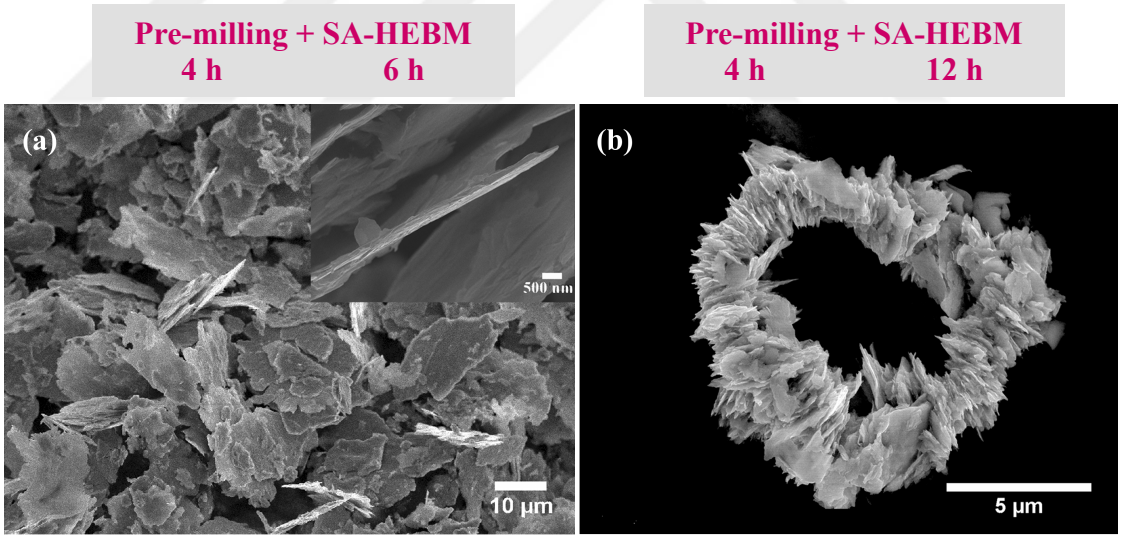

Figure 4.11 Closely packed $Nd_2Fe_{14}B$ nanoflakes (a) SA-HEBM for 6 h and (b) SA-HEBM for 12 h.

We have also investigated how the microstructure changes by keeping the pre milling time constant at 4 h and changing the SA-HEBM time from 6 to 12 h. Figure

4.11 shows SEM image of the slurry pre-milled for 4h and SA-HEBM for 6 and 12 h. The flake thickness decreases from below 100 nm down to below 50 nm with longer SA-HEBM time (Figure 4.11 (b)). Unlike dry milling, wet milling energetically slows down the milling, and the impact that the particles receive is much less. Although the majority of flakes produced by two-step HEBM are polycrystalline and isotropic, a very small fraction of the slurry contains flakes, which stays single crystalline and/or have low-angle grain boundaries (Figure 4.11 (b)). Orientation of the subgrains does not deviate much from the orientation of the single-crystal precursor particles as long as the boundaries remain small angle-type [15]. Those flakes are stocked parallel to each other and formed ring structures. The most likely mechanism behind such arrangement is the minimization of the magnetostatic energy. This implies, in particular, that the easy magnetization directions of the individual flakes are oriented perpendicular to the surface of the flakes.

4.3.2 Formation Mechanism of Nanoparticles

As discussed above, the addition of surfactant (Oleic acid, OA) facilitates the formation of both nanoflakes and nanoparticles. Wet ball milling in the presence of a solvent and/or surfactant is known to decrease particle agglomeration during the milling [16, 17]. Other important effects of solvent and surfactants include the following: preserving the crystal structure of magnetic phases and avoiding amorphization, decreasing interparticle friction, lowering the energies of freshly cleaved surfaces, thus enabling long-range capillary forces and lowering the energy required for crack propagation [18].

During the milling process, as soon as the particles and/or fresh surfaces are formed, surfactants are absorbed on to the surface of the particles by the formation of

the chemical bonds, which prevents agglomeration (The tail portions (R) of the surfactants repel each other, see Chapter 3). This greatly reduces cold welding and the re-welding of crushed particles, which finally allows the separated particles with smaller sizes to be formed.

FTIR study has been performed on the samples, which shows the chemical structure of the molecules. Figure 4.12 presents FTIR spectra of $N_2dFe_{14}B$ samples milled with and without the OA. The peaks at 2922, 2853 and 1705 cm^{-1} correspond to the C-H (symmetric and asymmetric oscillations) and C=O bonds [19] (the peaks at 2335 - 2360 cm^{-1} are believed to be caused by carbon dioxide present in the air.). Importantly, the peak at 1705 cm^{-1} (Figure 4.12 (c)) is dramatically suppressed compared to the spectrum of pure OA [19] indicating that the C=O bond is broken. This suggests that during the SA-HEBM of the powders, the OA molecule is chemically attached to the surface of the particles in a carboxylate form.

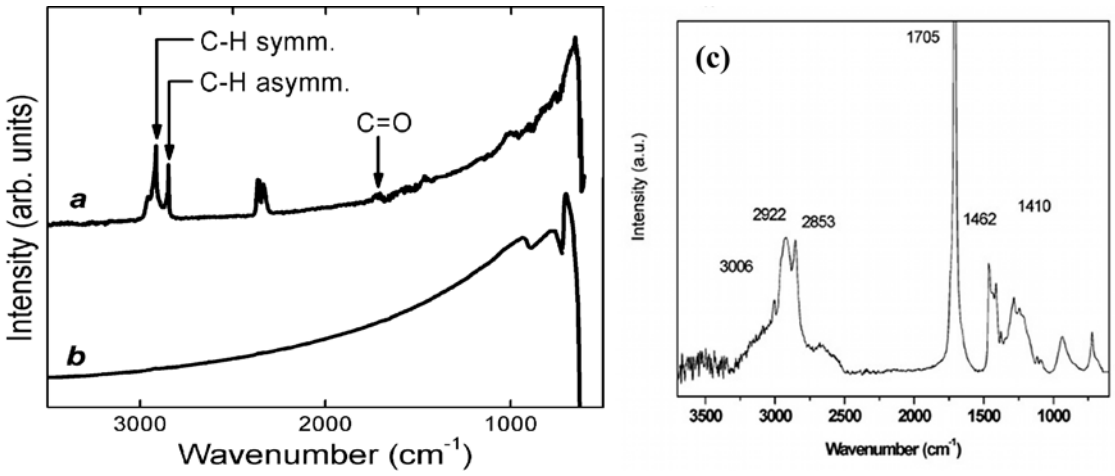

Figure 4.12 FTIR spectra of $Nd_2Fe_{14}B$ powders milled for 6 h (a) with OA, (b) without OA and (c) FTIR spectra of pure OA.

Figure 4.13 The nanoparticles along with the flakes after two-step milling.

When surfactants were added, along with heptane during milling, a black-colored liquid containing a dispersion of nanoparticles was obtained along with coarse particles (slurry particles), which quickly settled down at the bottom of the milling vial. The tail portions of the surfactant are hydrophobic in nature and are soluble in heptane (C_7H_{16}), which helps the nanoparticles to disperse into the heptane. It was found that the suspension time of these powders milled without surfactants in heptane was less than 1 minute, while particles milled with surfactants remained floating in heptane for several hrs or even many days, depending on particle size. Nanoparticles with a size less < 20 nm can disperse in heptane for long periods of time. As soon as the heptane dispersion of particles (after the ball milling) is transferred to a storage container, the larger size particles sediment quickly at the bottom of the container because of gravity. In Figure 4.13, the black liquid contained a dispersion of the nanoparticles.

As mentioned before, nanoparticles have been obtained after SA-HEBM along with the flakes. When the separation has been done on the slurry, we have observed

nanoparticles with an average size from 2.7 to 25 nm depending on the pre-milling time (Figure 4.14) [20]. The particle size distributions were determined by using the image processing software ImageJ, sampling over five hundred nanoparticles to have better statistics. The histograms of nanoparticles are shown for all sizes in Figure 4.14. From the distribution fit, the mean sizes were determined to be 25, 16, 10 and 2.7 nm with standard deviations from 1.6 to 0.27, respectively.

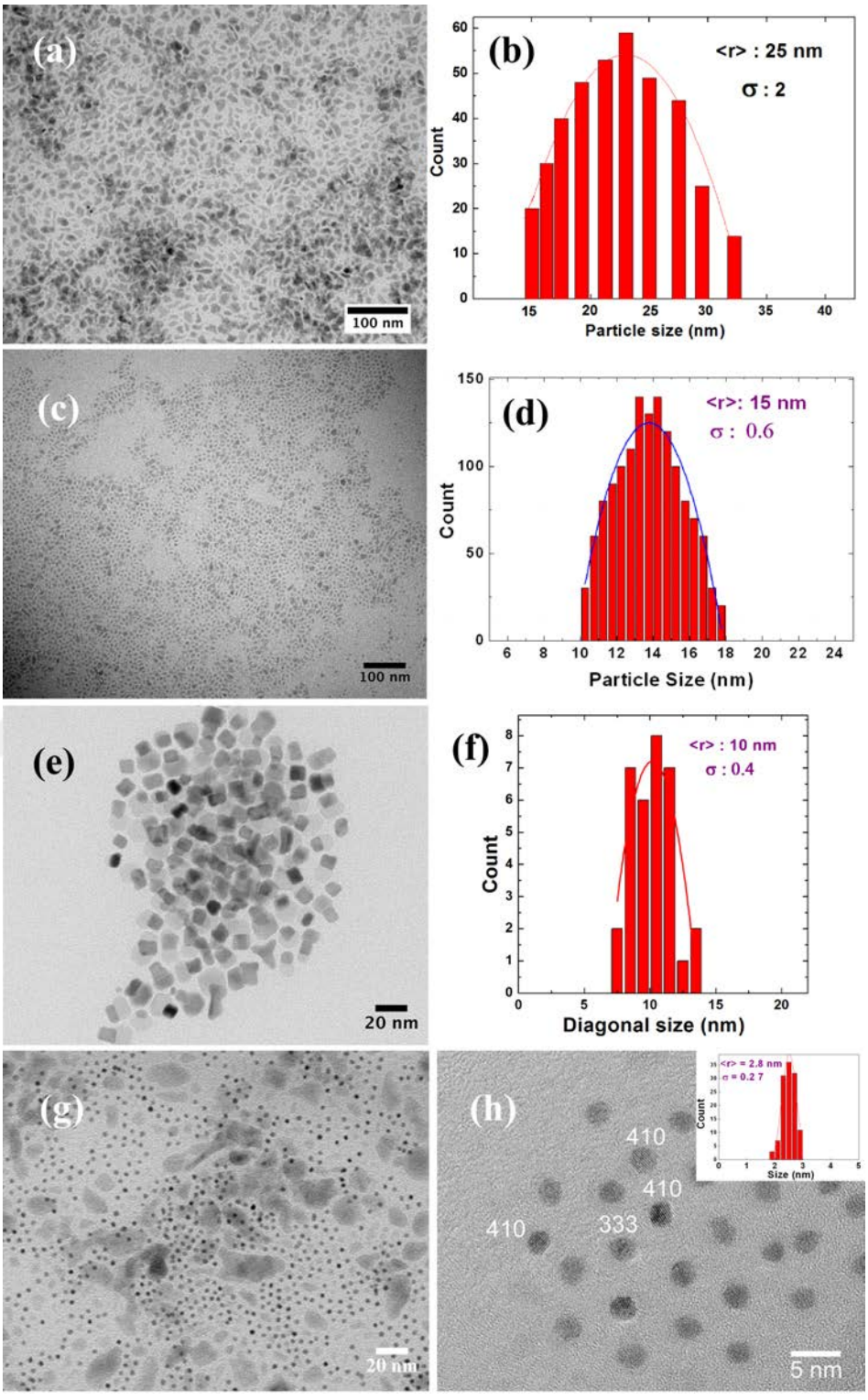

Figure 4.14 $Nd_2Fe_{14}B$ nanoparticles with different sizes from 25 to 2.7 nm.

Selected area diffraction (SAD) patterns shown in Figure 4.15 (b) are used to investigate the crystal structure of the nanoparticles. The SAED patterns match that of the 2:14:1 structure with no rings corresponding to bcc Fe or other impurities. Moreover, the SAED patterns suggest that the particles are crystallographically oriented. A high-resolution TEM (HRTEM) (Figure 4.15 and Figure 4.17) reveals that the particles are single crystals; the d-spacing values measured for the images shown correspond to the peaks of the tetragonal 2:14:1 structure. Energy dispersive x-ray spectroscopy confirms that the composition of the nanoparticles is the same as the one of the starting $Nd_2Fe_{14}B$ alloy and the Fe/Nd ratio is very close to 7, which is the same as the starting ratio (Figure 4.16) [20].

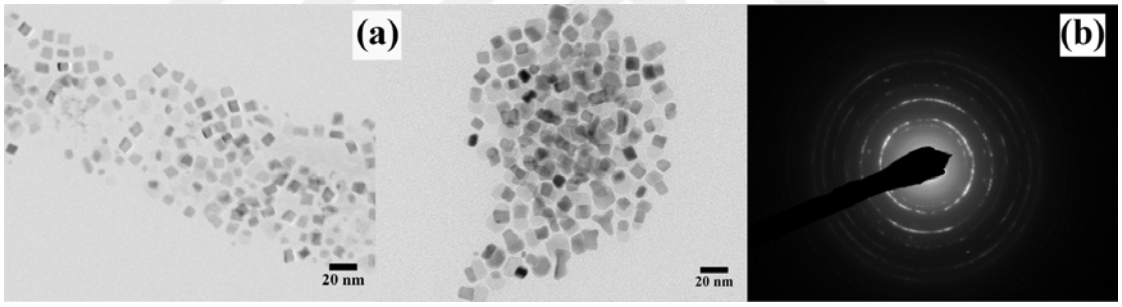

Figure 4.15 TEM bright field image of separated $Nd_2Fe_{14}B$ square nanoparticles and corresponding SAED.

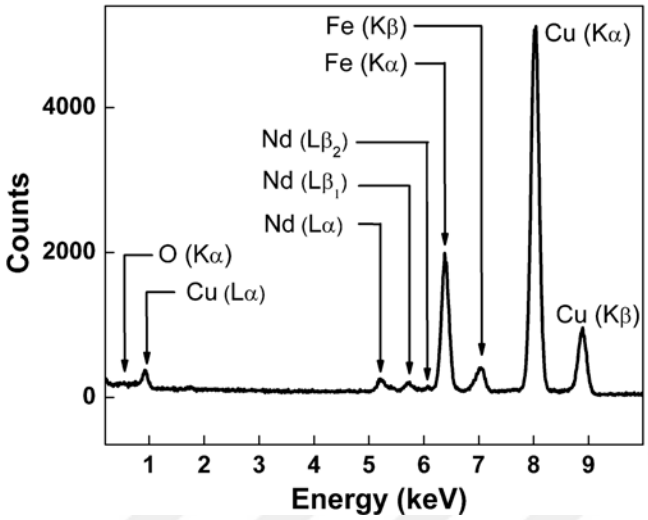

Figure 4.16 Energy dispersive x-ray spectroscopy of the nanoparticles. Cu contribution comes from the Cu grid.

4.3.2.1 Tuning of Particle Size

One of the goals of this study was to obtain nanoparticles with different sizes and study the correlation between the hard magnetic properties (as well as the intrinsic properties which are discussed in Chapter 6) and particle size. In this study, tuning of the size of $Nd_2Fe_{14}B$ was achieved by controlling the grain size of the precursor powder by milling for different times (Figure 4.6). Our findings in this work revealed that the shape and size of the nanoparticles are mostly dependent on the experimental parameters used in the processing. The precursor grain size plays an important role on the size of the nanoparticles. As the grain size of the precursor powder changes with milling time, the resultant grain sizes of the flakes changes as well. Table 4.2 summarizes the changes in grain sizes from the starting pre-milled powders to the flakes. As seen from the Table, when the duration of pre milling time was increased from 15 min to 4 h, the grain sizes of the nanoflakes decreases from 35 to 11 nm and the corresponding nanoparticle size decreased from 25 nm down to 10 nm (Figure

4.17). Grain size of the flake and the size of the nanoparticles, which are found in that batch, are in a very close agreement (Table 4.2). This suggests that there is a strong correlation between the grain sizes of the flakes in the slurry and the corresponding nanoparticles. Therefore, our data strongly suggest that the nanoparticles break from the nanoflakes along the grain boundaries, which behave as low energy breaking points.

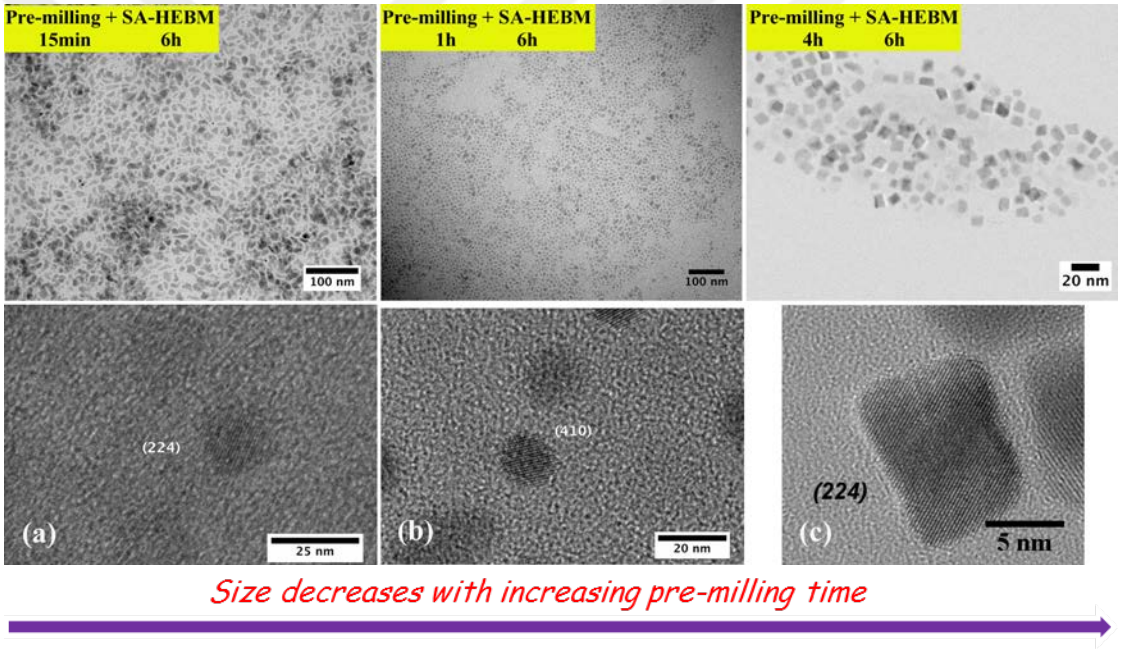

Figure 4.17 TEM bright field images of separated $Nd_2Fe_{14}B$ nanoparticles and corresponding HRTEM images a) 25 nm, b) 16 nm and c) 10 nm.

Table 4.2 Effect of different experimental conditions on the final particle size.

Milling Media	Pre-Milling Time	Grain Size (nm)	Type of Surfactant	Surfactant Wt. (%)	OA Milling Time	**Grain Size of flakes (nm)**	Upper Solution	**Nanoparticle Size**
Heptane	15 min	---	OA	15	6 h	**35 nm**	Low-Medium	**25 nm**
Heptane	30 min	> 50 nm	OA	15	6 h	**18 nm**	Medium	**22 nm**
					12 h	**9 nm**	Dark	**2.7 nm**
Heptane	1 h	42 nm	OA	15	6 h	**13 nm**	Dark	**16 nm**
Heptane	2 h	30 nm	OA	15	6 h	**12 nm**	Very Dark	**14 nm**
Heptane	4 h	18 nm	OA	15	6 h	**11 nm**	Pitch Dark	**10 nm**

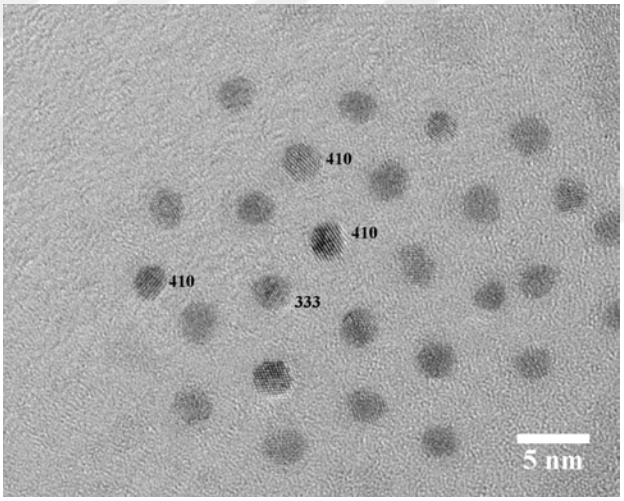

Figure 4.18 TEM bright field images of separated $Nd_2Fe_{14}B$ nanoparticles SA-HEBM for 12 h.

In the previous studies, the SA-HEBM time was kept constant while changing the pre-milling time (1st step). In order to observe the microstructure of the nanoparticles for different SA-HEBM times, the 30 minutes pre-milled powder was also subjected to SA-HEBM for longer time, 12 h. As seen in Figure 4.18, this

resulted in nanoparticles with 2.7 nm average size, which does not directly correspond to the grain size of the nanoflakes in the slurry (Table 4.2). In the initial 6 h of SA-HEBM, a considerable nanoparticle quantity was already produced. There are two possible explanation for the mismatch between the nanoparticle size and the grain size of the nanoflakes in this case: 2.7 nm particles might be produced by *i)* over milling the nanoparticles which are already produced in the initial 6 h of SA-HEBM, and/or *ii)* breaking the nanoflakes with grain sizes around 3 nm into nanoparticles.

4.3.2.2 Shape Control

TEM examination of the $Nd_2Fe_{14}B$ slurry led to a surprising discovery: the presence of well-shaped square $Nd_2Fe_{14}B$ particles with an average size of 11 nm in the case of the longest pre-milled precursor powders (whereas otherwise we have only observed nanoparticles with regular shapes). To investigate the reason behind such effect, we have examined the microstructure of the slurries (flakes). In the case of square nanoparticles, when performing HRTEM on the slurry, we observed what appeared to be planar defects (Figure 4.19 (b)). The defect planes (including, perhaps, grain boundaries) could facilitate the breakage [20] of the flakes into square nanoparticles. This further proves that the nanoparticles break from the micron size flakes.

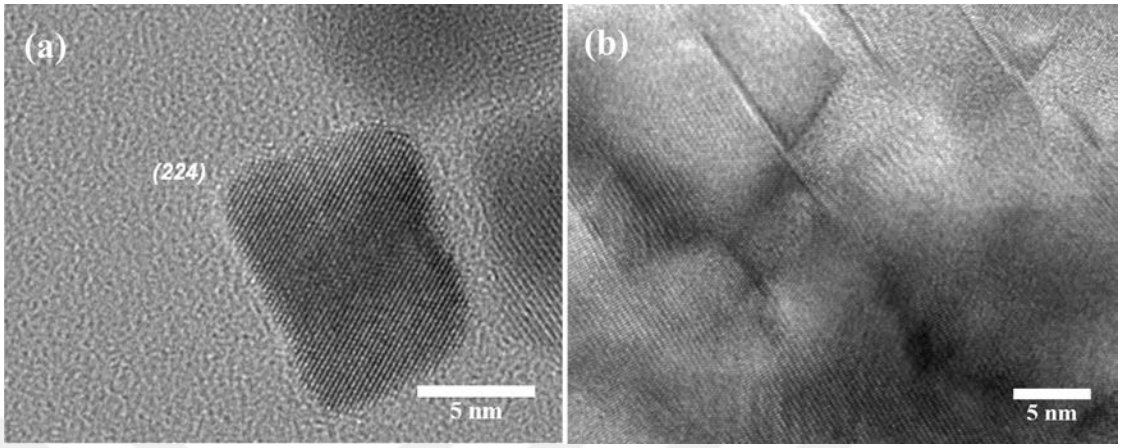

Figure 4.19 HRTEM image of the square nanoparticles and corresponding HRTEM of the nanoflakes.

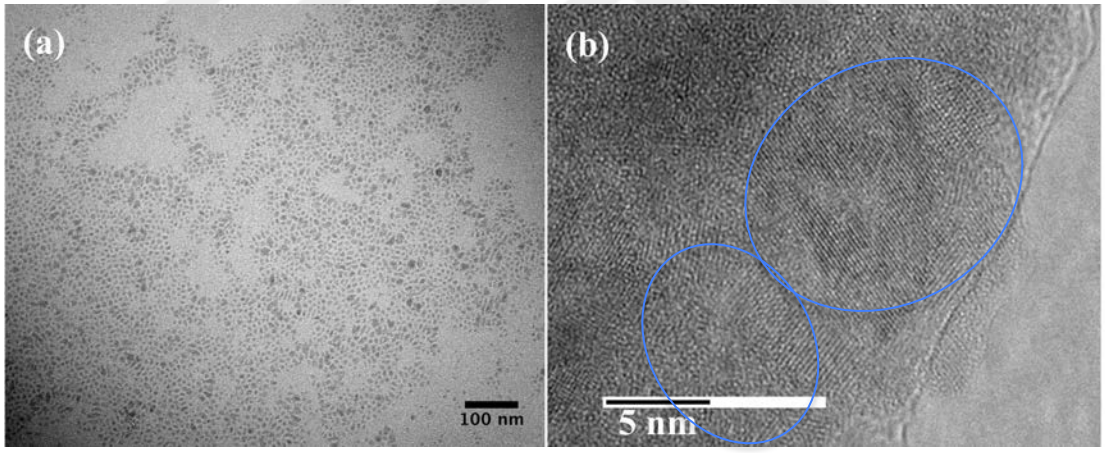

Figure 4.20 TEM image of the regular shaped nanoparticles and corresponding HRTEM of the nanoflakes.

On the other hand, when examining the slurries (flakes) where we obtained the regular shaped nanoparticles, we have not seen any trace of strain. As seen in the TEM

image of the flakes (Figure 4.20), the grains are regularly shaped and unlike the square nanoparticles they exhibit grains with strain.

It is evident that the shape and morphology of the nanoparticles are mostly dependent on the experimental parameters used in the processing. Microstructure and grain size of the flakes plays an important role on the size of the nanoparticles. The examinations strongly suggest that the nanoparticles break from the nano-size flakes during SA-HEBM.

4.3.3 Effect of Milling Conditions

4.3.3.1 Effect of Solution Polarity on Particle Morphology

Coarsely grained as-cast precursors powders showed tendency toward formation of thin flakes if milled in polar liquids (acetone and ethanol) in the marked contrast to milling in non-polar heptane.

To investigate further what triggers the formation of either the nanoflakes or the nanoparticles, we investigated the influence of different solvents such as, ethanol and acetone.

4.3.3.1.1 Heptane

As shown in Figure 4.21, HEBM in a non-polar solvent, heptane, produced irregularly shaped but more or less equiaxed particles. The range the particle sizes became narrower with increasing the milling time (section 4.3.1). In general, the process can be described as similar to the one observed for HEBM in argon [5]:

breaking of the coarse ingot fragments is followed by agglomeration of the debris and subsequent densification of the agglomerates.

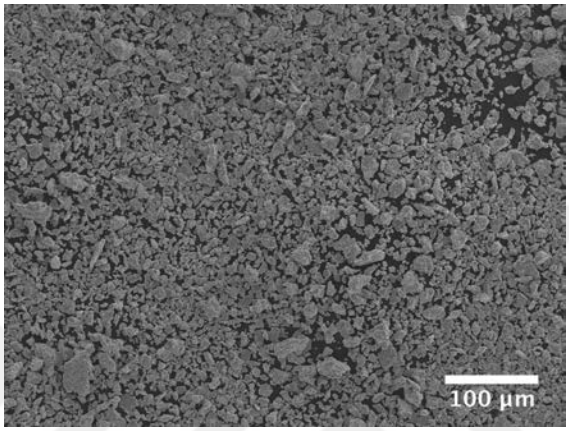

Figure 4.21 Particles in slurry after wet-milling in heptane.

4.3.3.1.2 Ethanol and Acetone

The critical role of the surfactants in suppressing agglomeration of the powder particles of the rare-earth hard magnetic materials has been demonstrated earlier, but so far only for HEBM performed in heptane, a non-polar liquid. On the other hand, surfactant-free high-energy milling in ethanol and aceton, which is polar, reportedly yielded flakes in the case of Fe-Co and Sn-Ag-Cu alloys [13,21].

Polarity (the dielectric constant) of the liquid environment is known to be among the most important factors influencing the milling process. The dispersibility of certain ceramic powders increases and their agglomeration decreases with increasing the dielectric constant of the surrounding liquid. This plays a crucial role in producing the powders in the form of flakes [3,4,22].

When the as-prepared $SmCo_5$ was milled in acetone and ethanol the results were markedly different. After 60 min of milling in these polar liquids, the fraction of small particles (smaller than 10 μm) was considerably greater than after the milling in heptane. This difference may indicate the reduced rate of agglomeration. After 2 h, the ethanol-milled particles of all sizes also had a distinctly anisotropic shape. After 5 h, as it is shown in Figure 4.22, the particles evolved into the 0.1 - 0.2 μm-thick flakes having several microns in the lateral dimension. Qualitatively, this shape evolution during the surfactant-free HEBM in ethanol is very similar to the one observed for the surfactant-assisted HEBM in heptane. As seen in Figure 4.23, the milling in acetone also produced anisotropically shaped particles, but more coarse than the milling in ethanol.

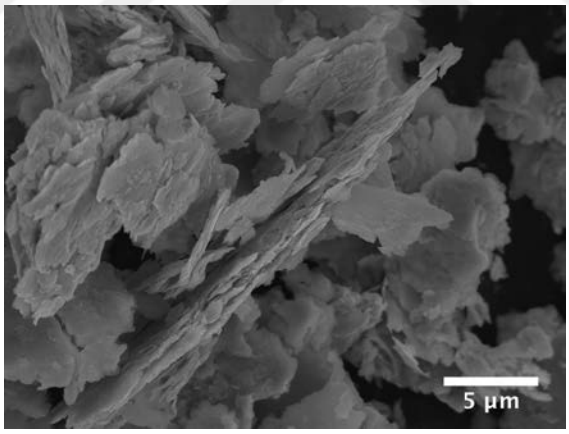

Figure 4.22 SEM of the slurry after milling in ethanol.

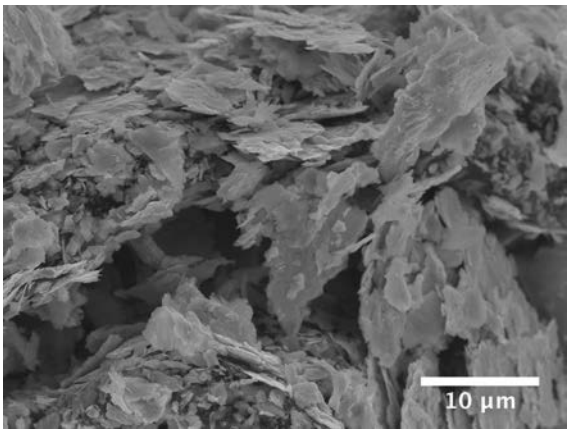

Figure 4.23 SEM of the slurry after milling in aceton.

Our finding does not establish a direct correlation between the effect of liquid and its dielectric constant, but they strongly suggest that such correlation exists.

4.3.3.2 Effect of Different Surfactants

Coarsely grained as-cast precursors powders showed tendency toward formation of different size nanoparticles and thin flakes if two-step SA-HEBM is applied. The above "surfactant-assisted" milling relies on the complex process control agent, the mixture of a non-polar "solvent" (e.g., heptane) and a separate "surfactant" (e.g., oleic acid).

To investigate further what triggers the formation of either the nanoflakes or the nanoparticles, we investigated the influence of different surfactants such as, OY, octanoic acid, TOP and TOA.

4.3.3.2.1 Oleylamine (OY)

The first step in HEBM is performed milling the powder in heptane without the presence of surfactants, as before. In the second stage, the OY is added to the milling vial as the surfactant, which is filled with heptane.

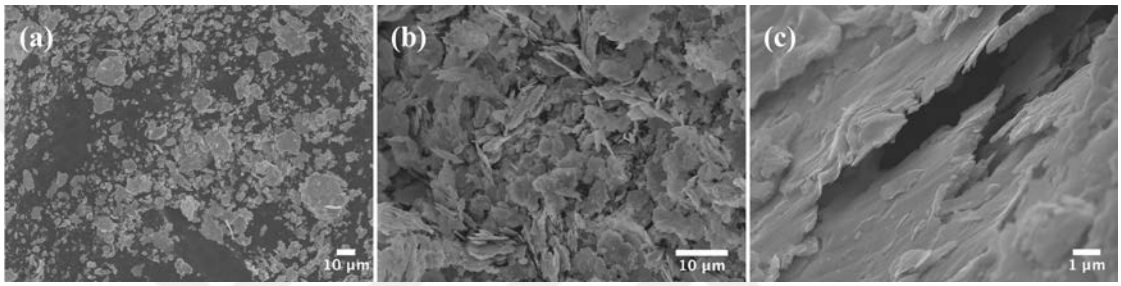

Figure 4.24 SEM image of $Nd_2Fe_{14}B$ powders SA-HEBM with OY (a) 6 h, (b) 12 h, and (c) HR-SEM of 12 h.

OY showed tendency toward formation of thin flakes much later (after 12 h) in the milling in contrast to milling with OA (Figure 4.24).

4.3.3.2.2 Octanoic Acid

As compared to OY as the surfactant, octanoic acid has shown the same behavior, in contrast to milling with OA.

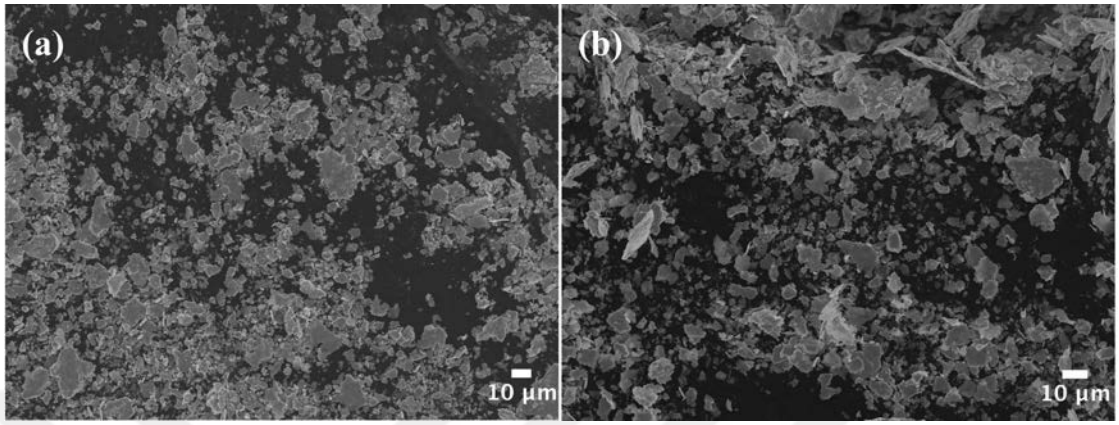

Figure 4.25 SEM image of $Nd_2Fe_{14}B$ powders SA-HEBM with octanoic acid for (a) 6 h, and (b) 12 h.

4.3.3.2.3 Trioctylphospin (TOP)

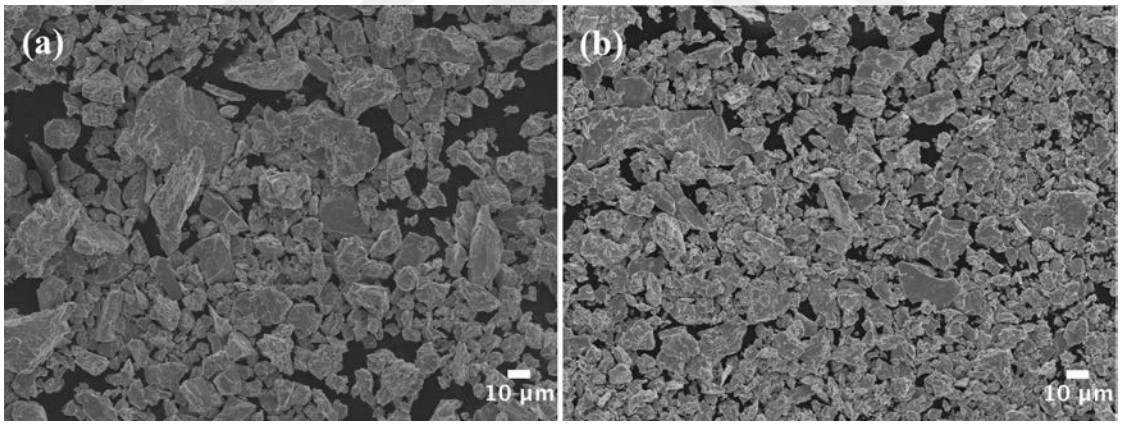

Figure 4.26 SEM image of $Nd_2Fe_{14}B$ powders SA-HEBM with TOP for (a) 6 h, and (b) 12 h.

4.3.3.2.4 Trioctylamine (TOA)

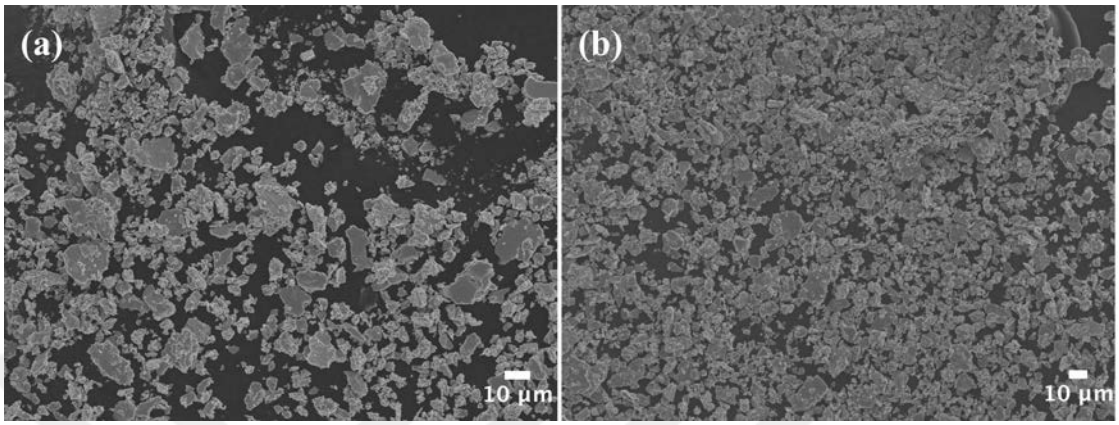

Figure 4.27 SEM image of $Nd_2Fe_{14}B$ powders SA-HEBM with TOA for (a) 6 h, and (b) 12 h.

In the case of TOA and TOP, except some flattening (Figure 4.26 and Figure 4.27), no flake formation has been observed. As mentioned in the previous section, Polarity (the dielectric constant) of the liquid environment is known to be among the most important factors influencing the milling process. Our study has revealed that none of the surfactants we have tried so far is as compatible surfactant as OA to provide the right dielectric environment.

At the end of the milling procedure, the color of the liquid medium did not change, indicating that there was no dispersion of nanoparticles in the solution. It shows that the surfactants (OY, octanoic acid, TOA and TOP) did not functionalize the particles fully.

Figure 4.28 shows that FTIR of the nanoparticles milled with TOP does not show any change with respect to the FTIR of the pure TOP. This suggests that during

the SA-HEBM of the powders, the TOP molecule is chemically not attached to the surface of the particles.

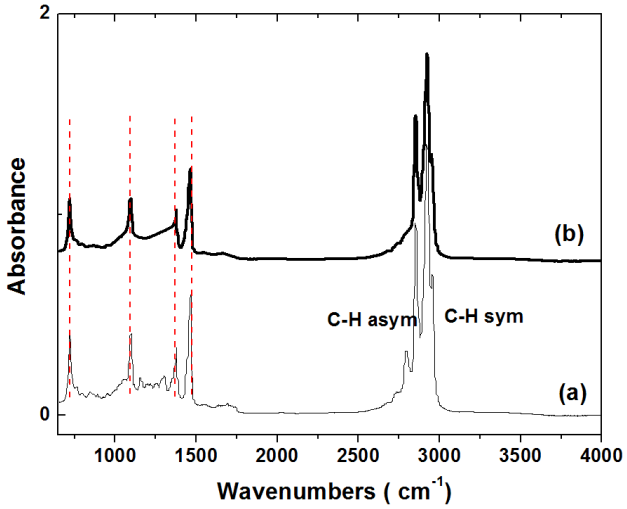

Figure 4.28 FTIR spectra of $Nd_2Fe_{14}B$ powders milled for 6 h with OA (a), and pure TOP (b).

4.4 $Nd_2(Fe,Mn)_{14}B$ Nanoflakes and Nanoparticles

The study of magnetic ordering at high temperatures in rare earth transition-metal nanoparticles and nanoflakes presents a great challenge due to both the very high reactivity of these materials and the negative effect of surfactants on the magnetic properties at high temperature. It is well known that Mn substitution for Fe in $Nd_2Fe_{14}B$ compound decreases the Curie temperature to below RT [23-25]. This allows for reliable measurements to be made since the oxidation problem is eliminated.

The aim of this study is to synthesize $Nd_2(Fe,Mn)_{14}B$ nanoparticles and nanoflakes and study the effect of particle size on their intrinsic properties (Curie temperature and spin reorientation) and hard magnetic properties by subjecting a brittle $Nd_2Fe_{14-x}Mn_xB$ alloy to a successive wet and surfactant-assisted high energy ball milling (SA-HEBM). In this chapter, we will focus on the structural properties and microstructures.

4.4.1 Structural Studies

After the two-stage HEBM (wet followed by surfactant-assisted wet), the slurry consists mostly of micron size flakes with thicknesses from below 500 nm to 50 nm and with an aspect ratio as high as 10^2 - 10^3 (Figure 4.29 (a, b, c)) [5,20]. As seen from the figure, as the pre-milling time increases, the flake thickness decreases like in the case of $Nd_2Fe_{14}B$. Figure 4.29 (a', b', c') shows the TEM bright field image of the corresponding anisotropic $Nd_2Fe_{14-x}Mn_xB$ nanoparticles with a size from 10 to 5 nm. High-resolution TEM (HRTEM) revealed that the particles are single crystalline.

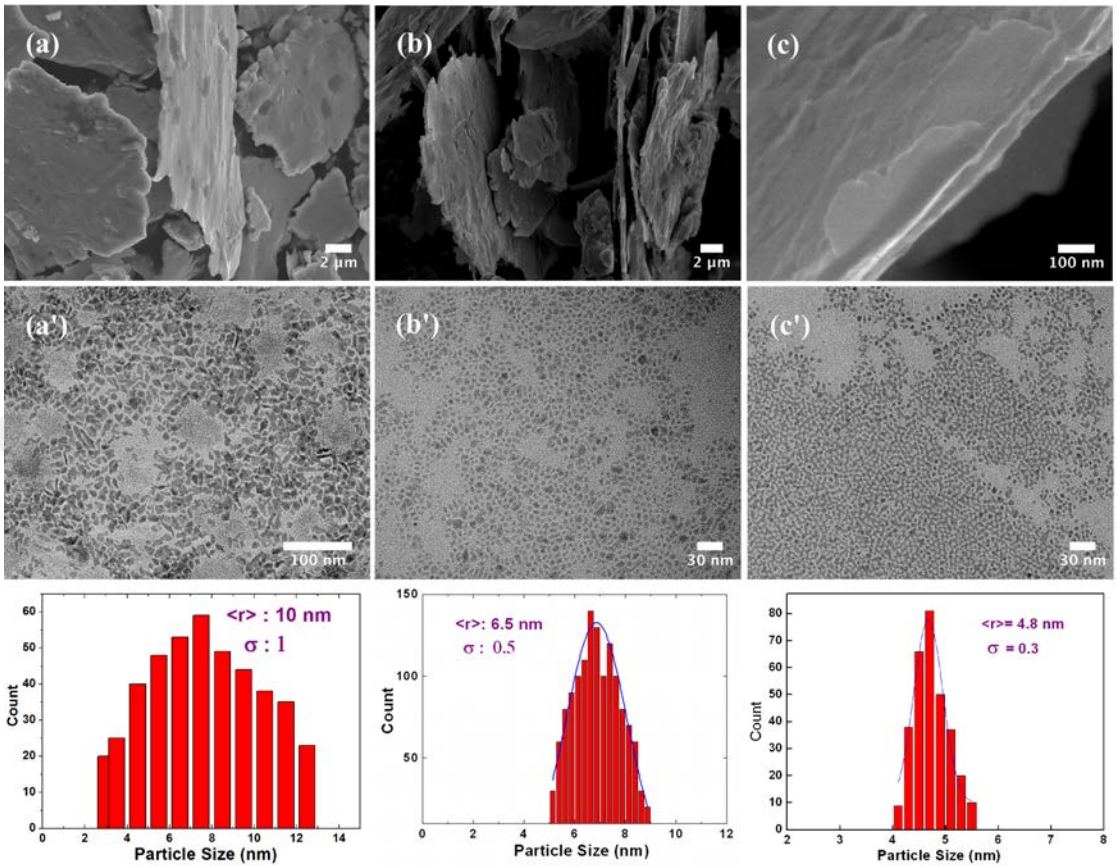

Figure 4.29 (a), (b) and (c) SEM images of the slurry milled for 3, 4, 6 h, respectively. (a'), (b') and (c') corresponding TEM images and size distributions of separated $Nd_2Fe_{14-x}Mn_xB$ nanoparticles.

Element	*Atomic %*	*[Nd/Mn(at%) : 0.667]*
NdL	*10.774*	
MnK	*17.748*	*0.60*
FeK	*71.478*	
Total	*100.0*	

Figure 4.30 Compositional analysis by EDX spectrum.

Energy dispersive x-ray spectroscopy (EDX) was used to identify the composition of the particles, especially those of smaller particles. EDX confirmed that the composition of the nanoparticles is the same as the one of the starting $Nd_2(Fe,Mn)_{14}B$ alloy (Figure 4.30).

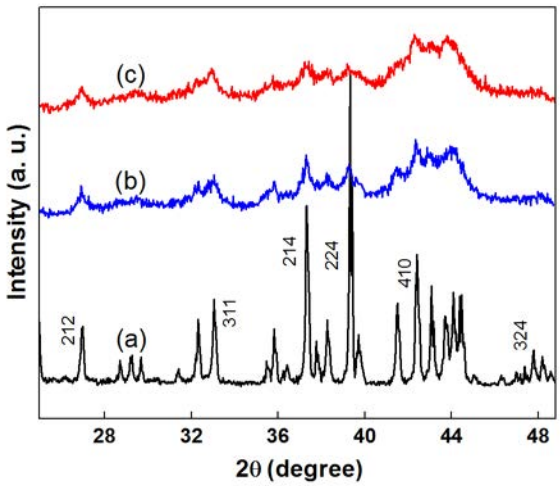

Figure 4.31 X-ray diffraction data for $Nd_2Fe_{11}Mn_3B$ alloy, which was homogenized (a) and pre-milled for 4 h and followed by SA-HEBM for 6 h (b) and pre-milled for 6 h and followed by SA-HEBM for 6 h (c).

XRD characterization of the $Nd_2Fe_{11}Mn_3B$ pre-milled powders (4 h and 6 h) after subsequent SA-HEBM for 6 h, is presented in Figure 4.31. It can be seen that no peaks from oxides or pure iron, are present in the diffraction patterns, indicating that the prepared powders have been effectively protected. The diffraction patterns also confirm that no detectable contamination or decomposition in the particles has occurred during the milling process. The crystallite size of the flakes is found to decrease from 26 to 10 nm.

Bulk $Nd_2Fe_{11}Mn_3B$ has a lower anisotropy and Curie temperature as compared to the ternary 2:14:1 phase [23-25]. We have observed high coercivities both in the starting ingot powder (Figure 4.32) and in the nanoflakes (Figure 4.29) at 50 K and a paramagnetic behavior at 300 K (Figure 4.33 (a,b)).

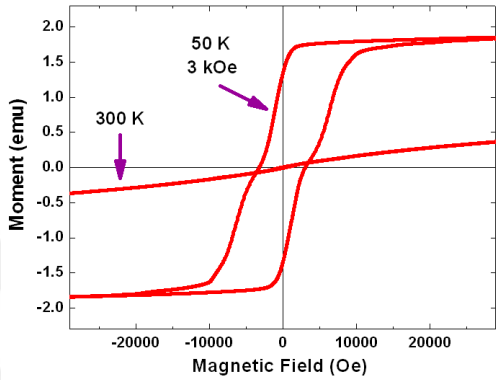

Figure 4.32 Hysteresis loops of the starting ingot.

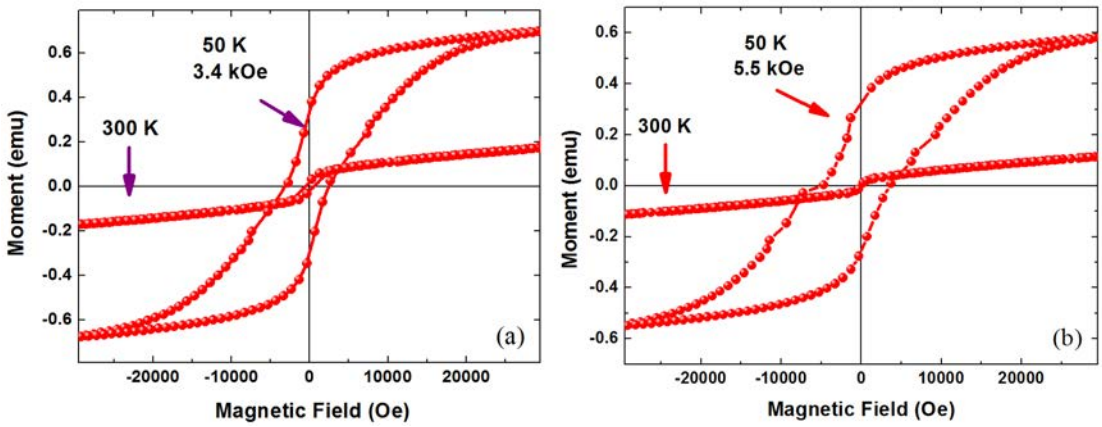

Figure 4.33 (a) and (b) Hysteresis loops of the flakes milled for 3 h and 4 h, respectively.

With decreasing flake thickness the coercivity first increases from 3.4 to 5.5 kOe, and then decreases down to around 2.4 nm as the flake thickness further decreases. The grain size at that point is likely to be approaching to the values comparable to the effective exchange length. Therefore, it is a likely reason for the decrease in coercivity.

Hysteresis loops for nanoparticles have been measured parallel to the alignment at 300 K and 50 K (Figure 4.34 (a',b')). Nanoparticles showed considerable coercivities at low temperature, with values at 50 K of 2.4 kOe and 0.72 kOe for the 9 and 6.5 nm nanoparticles, respectively (Figure 4.29). Unlike the case of flakes and bulk, the loops observed at 300 K for the nanoparticles exhibited ferromagnetic behavior instead of paramagnetic.

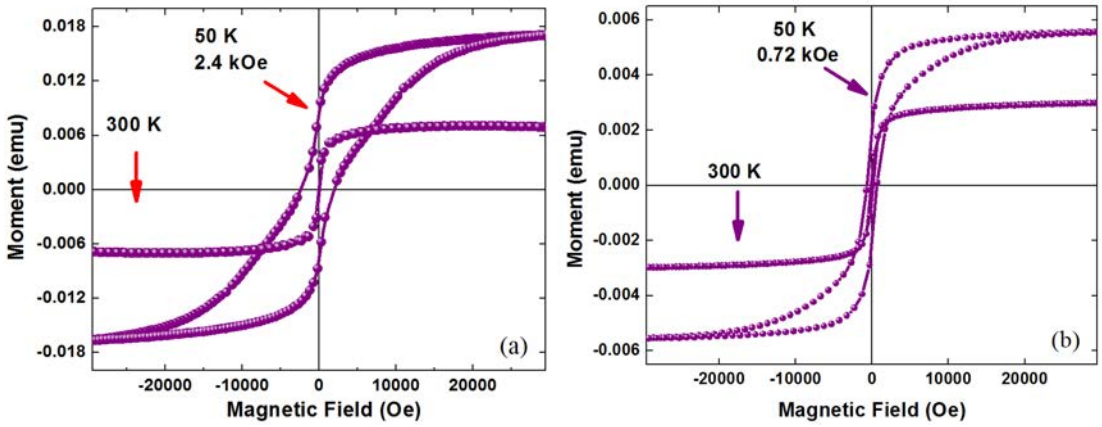

Figure 4.34 Hysteresis loops of separated $Nd_2Fe_{11}Mn_3B$ nanoparticles (a) 9 nm and (b) 6.5 nm.

In the case flakes, as seen in Figure 4.35 (a), the coercivity initially increases up to around 5.5 kOe due to grain size refinement then decreases (as discussed in

section 2). In the case of nanoparticles, the coercivity shows a strong dependence on particle size (Figure 4.35 (b)). As the particle size decreases, the coercivity declines substantially. The reason for this behavior may be a reduced magnetocrystalline anisotropy of the nanoparticle because of surface disorder and thermal effects.

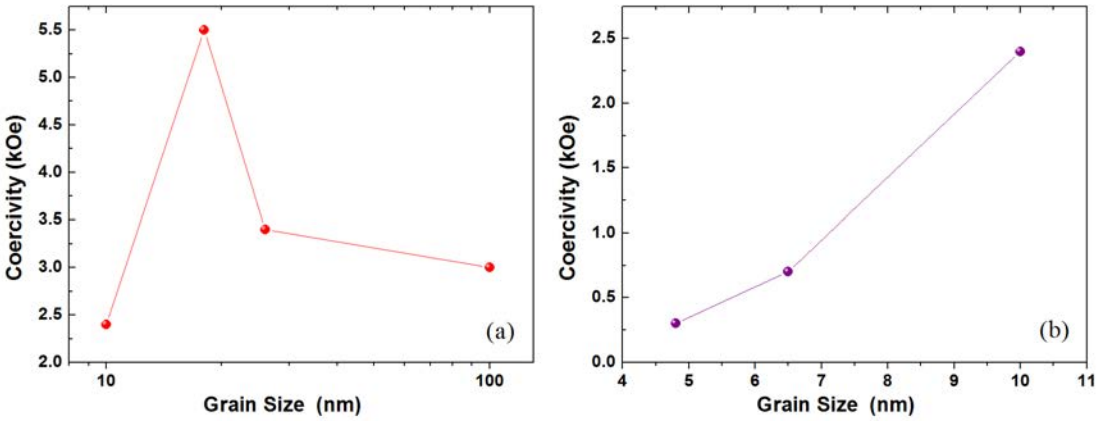

Figure 4.35 Plots of coercivity versus grain size plots of $Nd_2Fe_{11}Mn_3B$ (a) nanoflakes and (b) nanoparticles.

Figure 4.36 shows the change in coercivity with temperature from 100 K to 300 K. As the temperature goes down, the coercivity increases due to the increase in anisotropy (Discussed in Chapter 5).

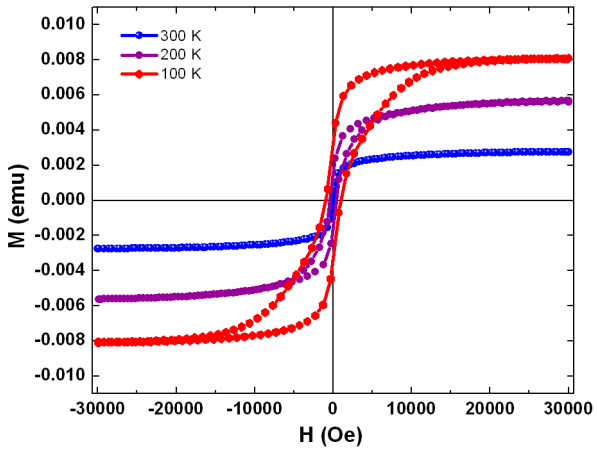

Figure 4.36 The change in coercivity with temperature.

4.5 $NdCo_5$ Nanoflakes and Nanoparticles

In this study, we have made $NdCo_5$ nanoparticles and nano-thick flakes by subjecting the brittle Nd-Co alloy to a successive wet and surfactant-assisted high energy ball milling (SA-HEBM). In this chapter, we will focus on the structural properties and microstructures. The magnetic properties will be reported in chapter 6.

4.5.1 Structural Studies

After pre milling for 1, 2, 4 h, the slurry contains polycrystalline micron size particles with the particle size distribution shown in Figure 4.37. Figure 4.38 (a) shows an SEM image of the slurry collected after the first-stage HEBM (wet milling in heptane for 4 h). The slurry consists mostly of micron size polycrystalline powders.

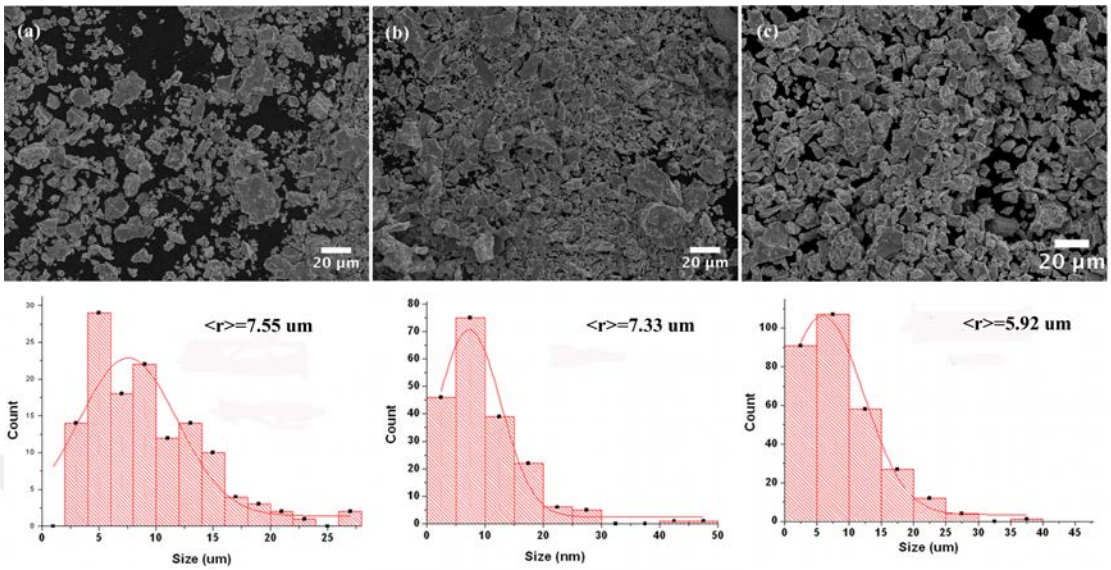

Figure 4.37 SEM images of $NdCo_5$ powders wet-milled (step 1) in heptane and corresponding size distributions (a) 1 h, (b) 2 h and (c) 4 h.

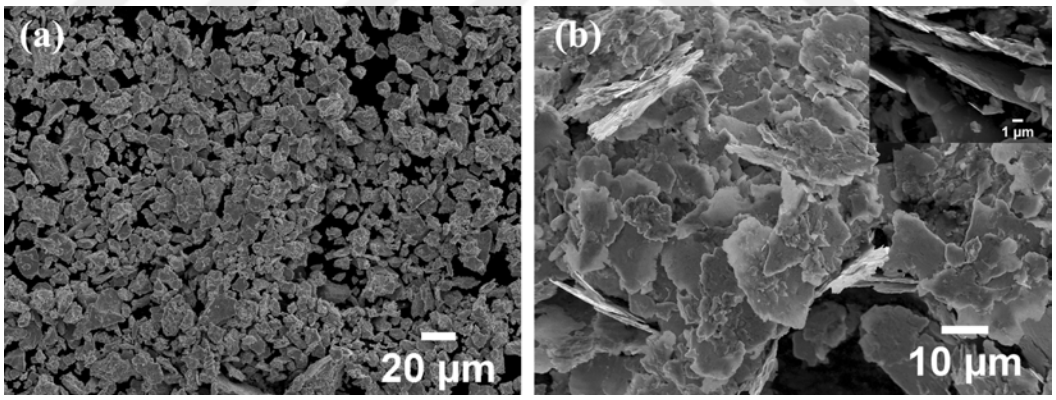

Figure 4.38 SEM image of $NdCo_5$ (a) polycrystalline powders and (b) nanoflakes.

After the two-stage HEBM (wet followed by surfactant-assisted wet), the slurry consists mostly of micron size flakes with an average thickness of 0.025 - 0.2 µm and with an aspect ratio as high as 10^2 - 10^3 (Figure 4.38 (b)). Similarly to $SmCo_5$ [5], the observed shape evolution of the particles of the brittle $NdCo_5$ material can be

attributed to its increased plasticity in the nanocrystalline state, which occurs via grain-boundary sliding. [11]

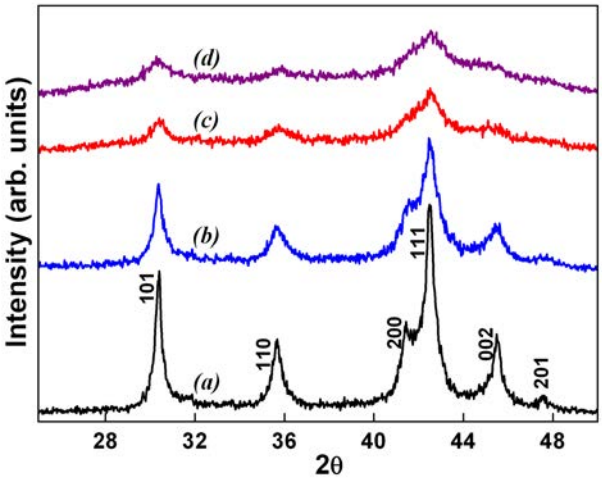

Figure 4.39 X-ray diffraction data for $NdCo_5$ (a) bulk alloy, (b) milled for 2 h in heptane, (c) milled for 4 h in heptane and (d) additional 6 h with OA.

XRD patterns of the $NdCo_5$ powders SA-milled for different time (up to 10 h) are presented in Figure 4.39. The as-made ingot exhibits the single $NdCo_5$ phase with $CaCu_5$ structure (hereinafter 1:5). The surfactant-free milling leads to a considerable broadening of the XRD peaks (Figure 4.39 (b,c)), but the subsequent surfactant-assisted milling does not change the peak width. During 6 h of the SA-HEBM, the average crystallite size decreased by only 1 nm, from 9 nm to 8 nm. The values of the microstrain determined were very small, 0.66% - 0.6%, for the initial 4 h and additional 6 h of milling.

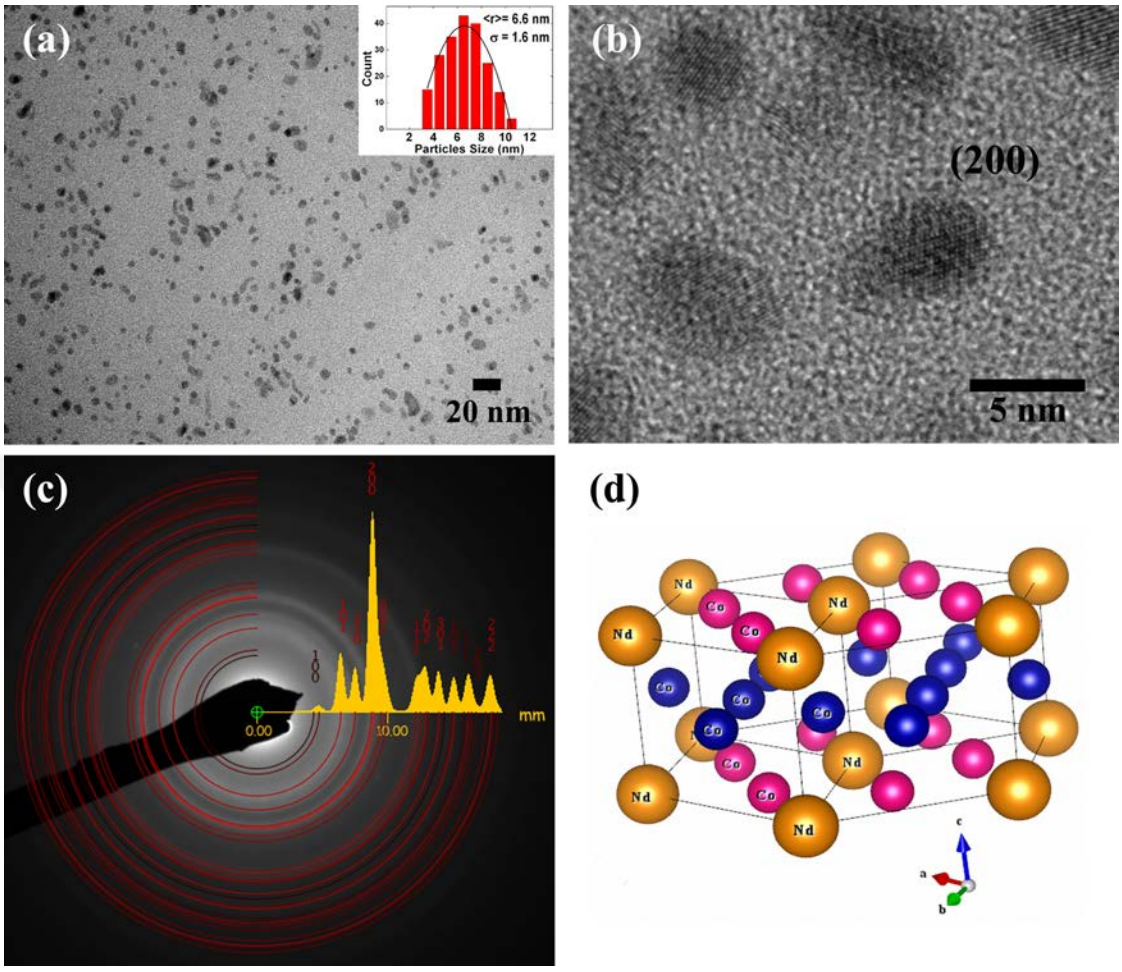

Figure 4.40 TEM image of separated $NdCo_5$ nanoparticles (a) bright field, (b) HRTEM image, (c) SAED pattern; and (d) $NdCo_5$ (hexagonal $CaCu_5$) crystal structure.

Figure 4.40 (a) shows the TEM bright field image of the nanoparticles with an average size 7 nm. A high-resolution TEM (HRTEM) (figure 4.40 (b)) reveals that the particles are single crystal; the *d*-spacing values of 0.198 and 0.211 nm measured for the image shown correspond to the (002) and (111) peaks of the hexagonal 1:5 structure. Indexed SAED image also proved the 1:5 structure (Figure 4.40 (c)).

Hysteresis loops for aligned powders and nano-flakes (Figure 4.38) have been measured parallel to the alignment direction at 300 K and 50 K. Although bulk $NdCo_5$ has a-axis anisotropy at 50 K [26-28], we have observed high coercivities in the nanoflakes at that temperature. (Figure 4.41 (a,b)) This behavior can be explained by rotation between different "a" direction.

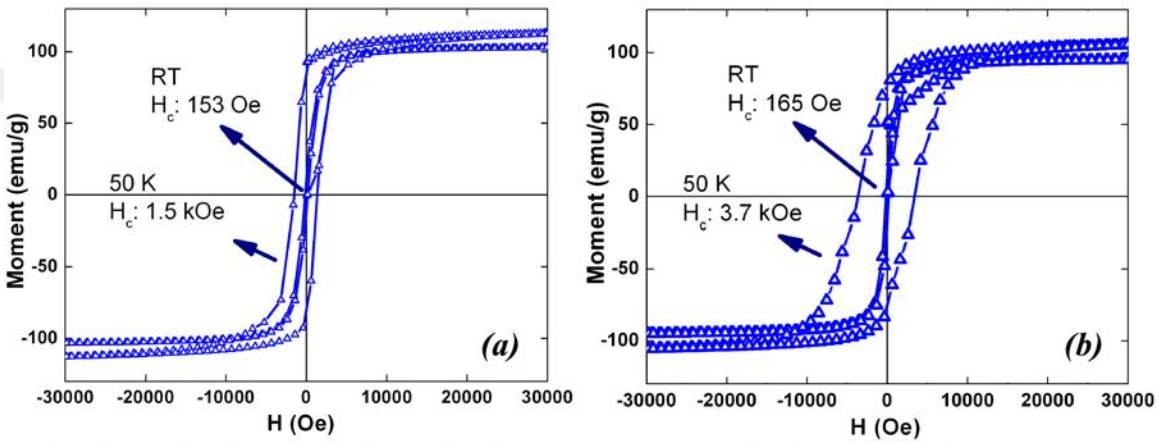

Figure 4.41 Hysteresis loops of aligned $NdCo_5$ samples, (a) after milling in heptane (nanocrystalline micron size powder) and (b) after surfactant-assisted HEBM (nanoflakes).

To our surprise, we have observed high coercivities, like in the case of flakes, on $NdCo_5$ nanoparticles (7 nm) (Figure 4.40) where the alloy has a uniaxial anisotropy. As seen in Figure 4.42 (a), the coercivity was found to be 1.2 kOe at 50 K, which is lower as compared to the flakes. The high values of coercivity, which were not expected in an a-axis anisotropy phase, can be attributed to the large surface anisotropy of nanoparticles that leads to an effective uniaxial-type of behavior. We have measured the hysteresis loop of those nanoparticles field-cooled below 240 K,

which is determined as the transition temperature from cone to a-axis. Field-cooled nanoparticles allowed the hysteresis loop measurement along the a-axis (Figure 4.42 (b)). The coercivity was found to be 3 kOe at 50 K, which is higher than the RT-aligned sample due to the much better alignment.

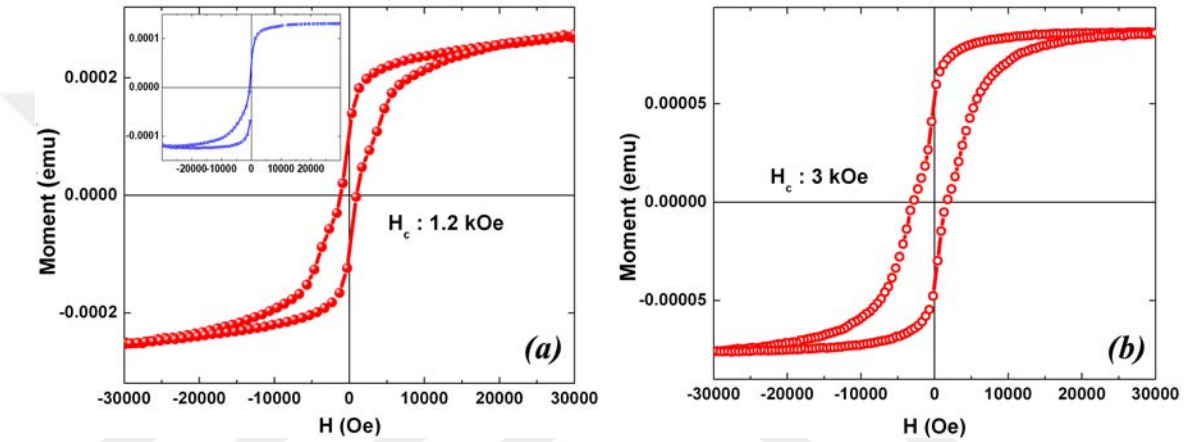

Figure 4.42 Hysteresis loops of $NdCo_5$ nanoparticles (a) Field aligned at RT measured at 50 K, inset: loop at RT and (b) Field cooled (3T) in heptane measured at 50 K.

4.6 $Sm_2(Co,Fe)_{17}$ Nanoparticles

4.6.1 Structural Studies

We produced magnetically hard $Sm_2(Co_{0.8}Fe_{0.2})_{17}$ nanoparticles. For the first time, Mono dispersed self-assembly of $Sm_2(Co_{0.8}Fe_{0.2})_{17}$ nanoparticles have been observed [29] with ultra-narrow size distribution after 4 h of SA-HEBM (Figure 4.43). Room-temperature coercivities have been obtained with maximum value of 2.9 kOe.

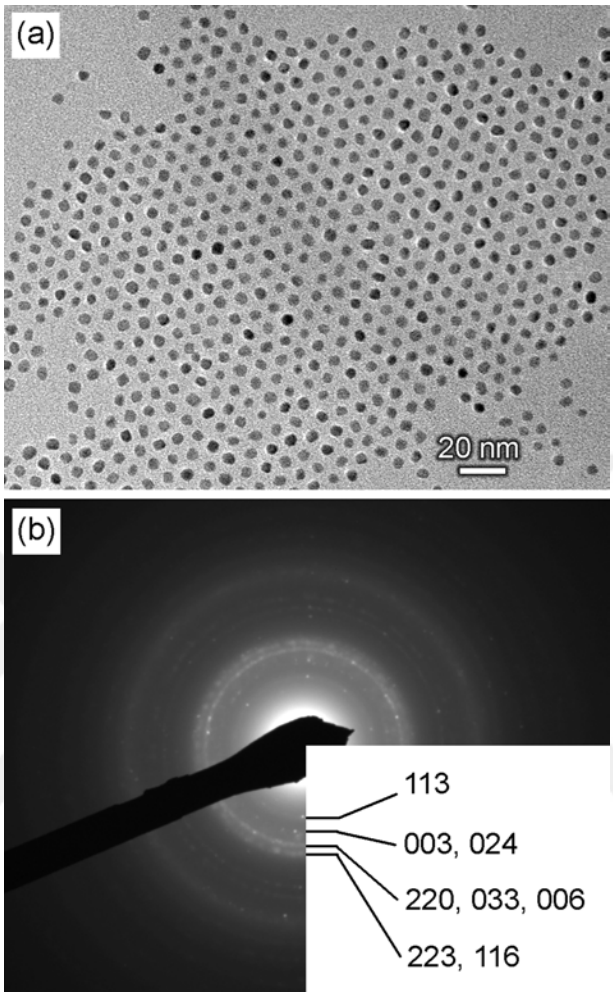

Figure 4.43 (a) TEM image of mono dispersed self-assembly of $Sm_2(Co_{0.8}Fe_{0.2})_{17}$ nanoparticles with 5 nm average size (b) corresponding indexed SAED image.

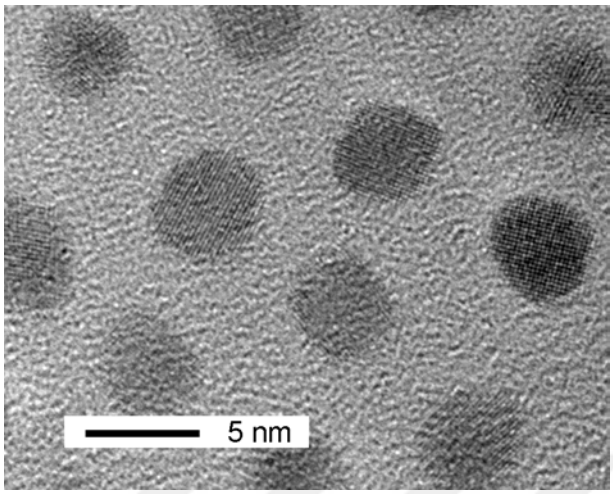

Figure 4.44 High resolution TEM image of the 4 h milled 2:17 alloy.

As seen in Figure 4.44, high resolution TEM images revealed anisotropic single crystalline nanoparticles [29]. The d spacings were measured in the lattice-imaging micrographs and found to match the rhombohedral (hkl) peaks. The energy dispersive spectroscopy revealed that the composition of the nanoparticles was the same as in the starting $Sm_2(Co_{0.8}Fe_{0.2})_{17}$ alloy.

4.7 $PrCo_5$ Nanoparticles

Figure 4.45 (a) shows the change in coercivity with milling time which exhibited a tendency to form what appears to be rod-shaped particles, especially for longer milling times (12 h). The formation of such rod-shaped nanoparticles was earlier explained [6,30] through either selective cleavage of crystals along the preferred orientation or anisotropic "growth" of the nanoparticles. The selective cleavage mechanism, though possible, is expected to be more prominent at the early stage of milling. The anisotropic "growth" of particles, on the other hand, appears more likely (this growth, of course, can only occur through coalescence of the smaller

particles), and the most probable reason for this is the magnetostatic interaction between the single domain particles [5,6].

Figure 4.45 (a) compares the magnetic properties of field-oriented $Pr_{1.02}Co_5$ powders wet-milled with and without the surfactant. The minimum of remanence M_r and the maximum of coercive force H_c which the powders milled without OA exhibit after about 100 min must correspond to a polycrystalline state of the powder particles with mostly randomly oriented grains. The polycrystallinity during milling is usually being induced via coalescence of the particles and/or via formation of new (sub)grains [11]. Further milling probably decreases the average grain size to values comparable to the effective exchange length, thus leading to the enhanced (isotropic) M_r and decreased H_c [31,32]. The particles milled with OA exhibit much slower evolution of M_r and H_c.

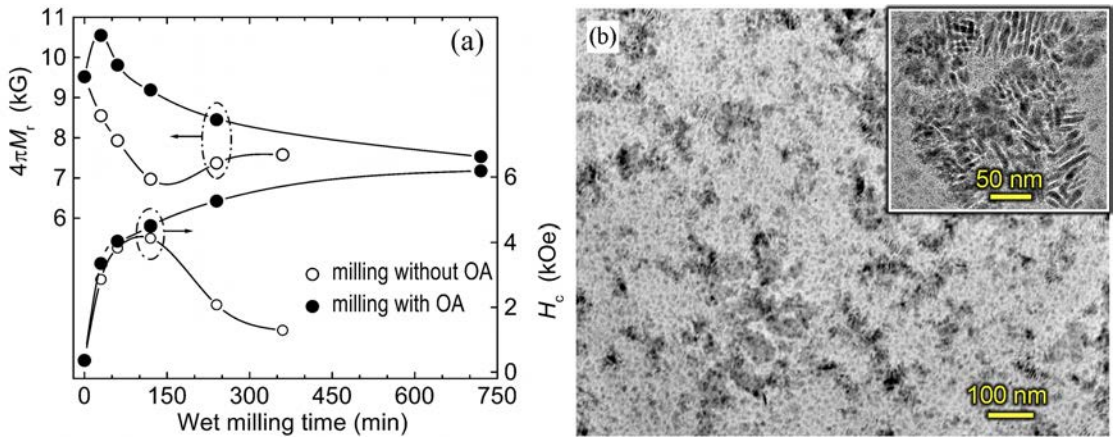

Figure 4.45 (a) Remanent magnetization and intrinsic coercivity of $PrCo_5$ powders milled in heptane with and without additions of surfactant. Powders were magnetically oriented and the measurements were corrected for self-demagnetizing field (b) $PrCo_5$ nanoparticles.

4.8 Effect of Mechanical Properties of the alloy on the production

To investigate further what triggers the formation of either the nanoflakes or the nanoparticles, we investigated the influence of different grain structure of the precursor powders.

4.8.1.1 MQ3

Textured nanocrystalline MQ-3 alloy was used as a precursor for the milling experiments (Figure 4.46 (a)). The range of studied conditions included single-step wet milling with %15 OA added as the surfactant. Milling time was varied from 1 min to 1 h.

As seen in Figure 4.46 (a), die-upset MQ-3 magnet consists of plate-like grains [33], approximately 600 run in length by 150 run in width, together with larger equiaxed grains that contain a speckling of precipitates in the grain interior. Nd-rich phases are found at the grain boundary.

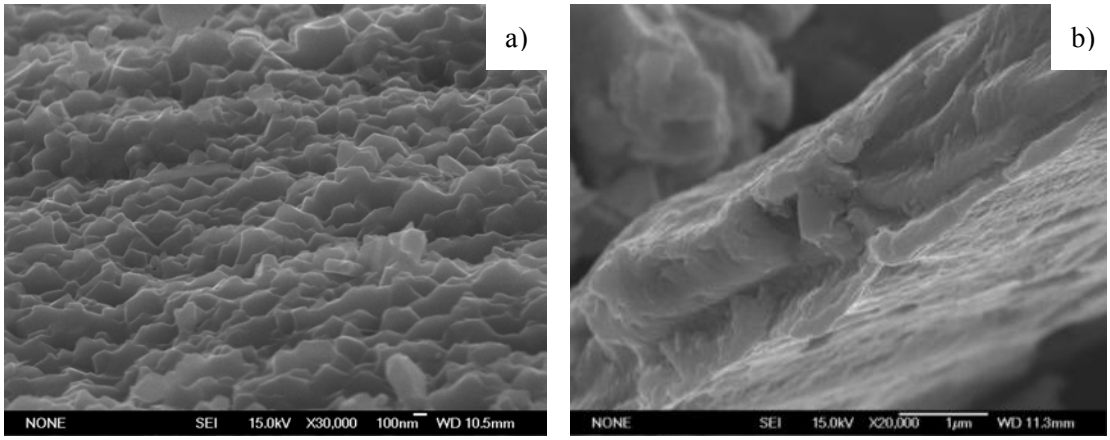

Figure 4.46 (a) Textured nanocrystalline MQ-3 alloy with exposed grains, (b) arc-melted ingot with protected grains.

We compared the nanocrystalline MQ-3 alloy with platelet shaped grains (Figure 4.46 (a)) and the arc-melted ingot with regular grains (Figure 4.46 (b)). Different milling times have been employed starting from very early stages of milling, 1 minute. Figure 4.47 compares the MQ-3 alloy and arc-melted ingot and shows the change in morphology with milling. As seen in Figure, in the case of MQ-3 alloy the powder starts breaking into submicron size particles within 6 min of milling whereas in the case of arc-melted ingot the powders does not break that easily. As seen in Figure 4.47 (b), amount of sub-micron particles is insignificant. It shows that grains being platelet shape facilitates the breakage of the grains into submicron particles.

When the microstructures were compared at later stages of milling, we have seen that the flake formation starts around 12 min of milling, which is much earlier as compared to arc-melted ingot. It has been suggested that the mechanical properties of nanocrystalline materials prepared by mechanical attrition are no longer controlled by dislocation movement through the crystals but by cohesion across the grain boundaries. Intercrystalline regions, which were believed to be formed in the HEBM, must greatly facilitate grain-boundary sliding. Grains being platelet and stacked together in MQ-3 powder, as seen in Figure 4.46 (a), makes that happen much easier.

It is evident that microstructure of the grains within the particles is the determinant in this process and that the formation of particles occurs through breakage of the grains into submicron particles along the grain boundaries. The findings are consistent with previous experiments with other alloys.

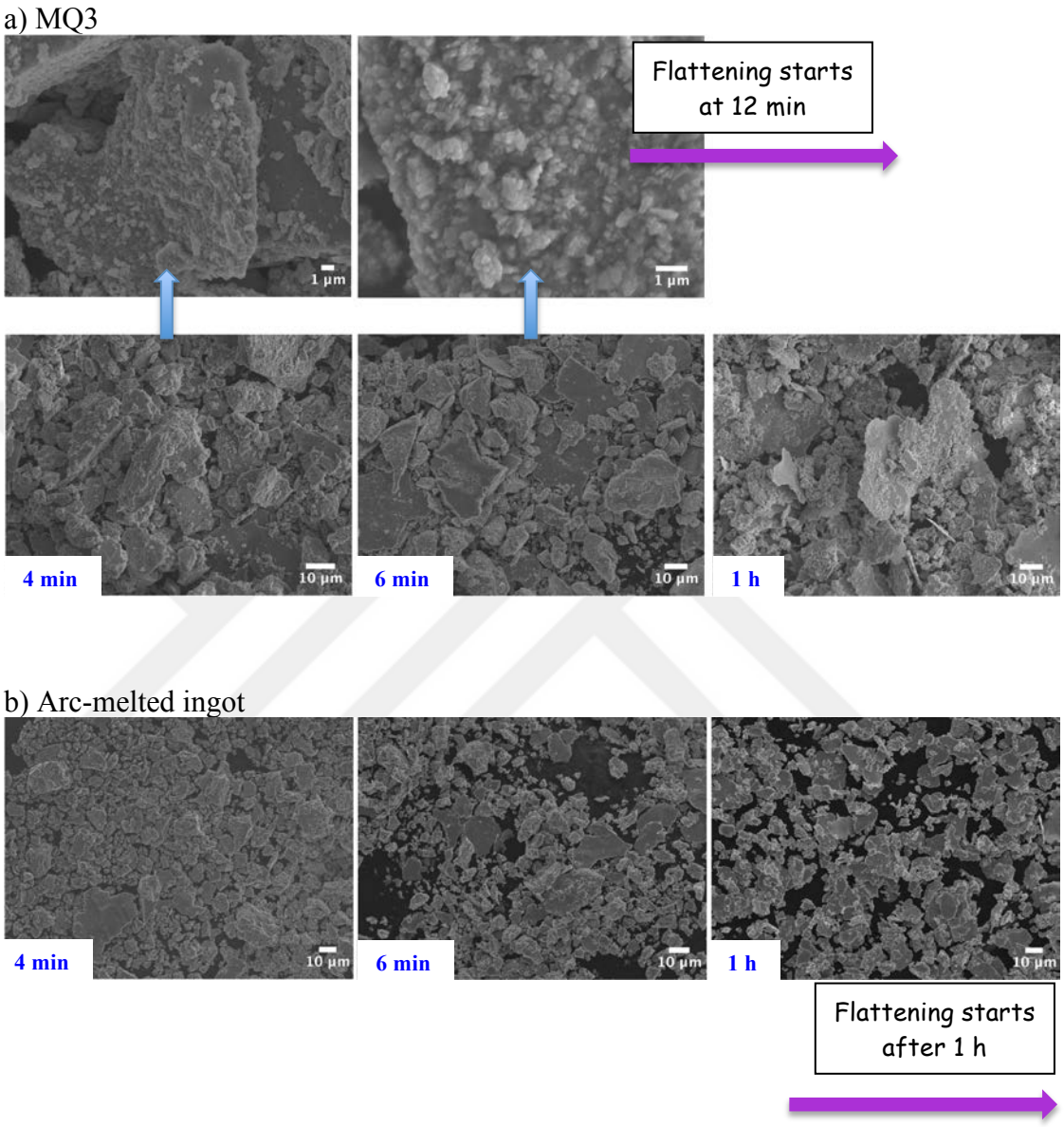

Figure 4.47 SA-HEBM of a) MQ-3 and b) arc-melted ingot powders for 4 min, 6 min and 1 h.

4.9 Stability Studies in the Magnetic Properties of Nanoparticles

As mentioned before, the rare earth metals are known for their high reactivity which makes the fabrication of rare-earth intermetallic nanoparticles very challenging.

The OA molecule itself, which makes a chemical bond at the surface of the particle, is an oxygen containing surfactant. Depending on the particle size, nanoparticles oxidize at a certain rate. Figure 4.48 shows the stability study on 25 nm particles (Figure 4.14). As seen in the figure, the magnetic properties (coercivity) start deteriorating after 2 days and are nearly lost after 5 days. The observation suggested that another surfactant, which does not include any O molecule, should be used (if they would allow the production of nanoparticles like OA!).

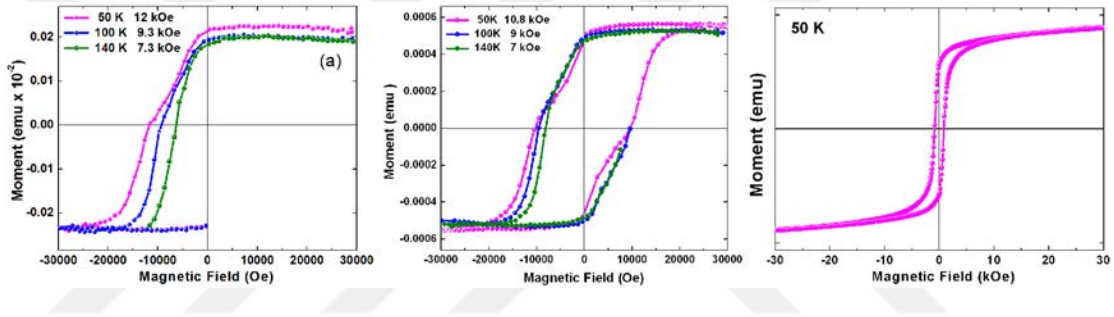

Figure 4.48 Stability study on 25 nm particles (a) a day old, (b) 2 days old and (c) 5 days old.

4.10 Summary

The studies have shown that two-stage SA-HEBM is a powerful technique, which allows us to obtain the compounds with different microstructures and control the shape and the size. It is found that the nanocrystalline structure acquired in the course of wet milling strongly influences the evolution of the particle shape and size during the second milling stage. A strong correlation between the grain size of the nanoflakes and the size of the nanoparticles has been observed. The data suggests that the nanoparticles break from the nanoflakes along the grain boundaries during milling.

For the first time, Mono dispersed self-assembly of 5 nm $Sm_2(Co_{0.8}Fe_{0.2})_{17}$ nanoparticles and $Nd_2Fe_{14}B$ nano-cubes have been observed with ultra-narrow size distribution using the novel SA-HEBM technique.

Our studies on different surfactants has revealed that the type of surfactant is the key to fabricate nanaoparticles and nanoflakes and none of the surfactants we have tried so far is as compatible surfactant as OA to provide the right dielectric environment.

To investigate further what triggers the formation of either the nanoflakes or the nanoparticles, we investigated the influence of different grain structure of the precursor powders. We studied MQ-3 alloy with platelet shaped grains and observed that the powder starts breaking into submicron size particles in the very early stages of milling. It revealed that grains being platelet shape facilitates the breakage of the grains into submicron particles.

It is evident that microstructure of the grains within the particles is the determinant in this process and that the formation of particles occurs through breakage of the grains into submicron particles along the grain boundaries.

Stability studies in the magnetic properties showed that the lifetime of the nanoparticles are quite short due to oxidation. The magnetic properties (coercivity) start deteriorating after 2 days and are nearly lost after 5 days. In order to solve this problem later efforts should be focused on finding an appropriate surfactant which has no oxygene molecule and also compatible with RE-TM compounds at the same time!

REFERENCES

1. W. Kraus and G. Nolze *J. Appl. Crystallogr.* 29, 301 (1996).
2. G. K. Williamson and W. H. Hall *Acta Metall.* 1, 22 (1953).
3. H. El-Shall and P. Somasundaran *Powder Technol.* 38, 275 (1984).
4. Y. H. Choa, N. Bamba, H. Hayashi, H. Kondo, T. Sekino and K. Niihara *J. Mater. Sci.* 34, 3789 (1999).
5. A. M. Gabay, N. G. Akdogan, M. Marinescu, J. F. Liu and G. C. Hadjipanayis *J. Phys.: Condens. Matter.* 22, 164213 (2010).
6. N. G. Akdogan, G. C. Hadjipanayis and D. J. Sellmyer *IEEE Trans. Magn.* 45, 10 (2009).
7. L. Schultz, J. Wecker and E. Hellstern *J. Appl. Phys.* 61, 3583 (1987).
8. J. Han, S. Liu, X. Zhang, H. Du, C. Wang, Y. Yang, M. Yue and X. Liu *J. Appl. Phys.* 101, 09K502 (2007).
9. E. M. Kirkpatrick, S. A. Majetich and M. E. McHenry *IEEE Trans. Magn.* 32, 4502 (1996).
10. J. I. Lee, H. W. Kwon and Y. S. Kang *J. of Magnetics* 13, 102 (2008).
11. H. J. Fecht *Nanostruct. Mater.* 6, 33 (1995).
12. B. Jiang and G. J. Weng *Int. J. Plast.* 20, 2007 (2004).
13. P. H. Zhou, L. J. Deng, J. L. Xie and D. F. Liang *J. Alloys Compd.* 448, 303 (2008).
14. X. Xiao, Z. G. Zeng, Z. W. Zhao and S. W. Xiao *Mater. Sci. Eng. A* 475, 166 (2008).
15. B.Z. Cui, L.Y. Zheng, W.F. Li, M. Marinescu, J.F. Liu, G.C. Hadjipanayis, "Anisotropic $Nd_2Fe_{14}B$ flakes with a submicron thickness," submitted to *Journal of Physics D: Applied Physics.*
16. P. Somasundaran and I. J. Lin *Ind. Eng. Chem. Process Des. Dev.* 11, 321 (1972).
17. D. Guérard *Rev. Adv. Mater. Sci.* 18, 225 (2008).

18. W. A. Kaczmarek and B. W. Ninham *Mater. Chem. Phys.* 40 21 (1995).

19. T. K. Jain, M. A. Morales, S. K. Sahoo, D. L. Leslie-Pelecky and V. Labhasetwar *Mol. Pharm.* 2, 194 (2005).

20. N. G. Akdogan, G. C. Hadjipanayis and D. J. Sellmyer *Nanotechnology* 21, 295705 (2010).

21. S.T. Kao, J.G. Dun, J. Electronic Materials, 33, 1445 (2004).

22. Y.Z. Chen, Y. Liang, F. Zheng, R.C. Zhou, Z.C. Feng *Ceram. Int.* 27, 73 (2001).

23. F. Bolzoni, F. Leccabue, O. Moze, L. Paret and M. Solzi *J. Magn. Magn. Mater.* 67, 373 (1987).

24. G. Z. Xie, Z. J. Tian, Z. Yu, B. X. Gu, M. Lu, Y. W. Du *J. Magn. Magn. Mater.* 251, 109 (2002).

25. G. Xie, S. Yin, F. Zhang, P. Lin, B. Gu, M. Lu, Y. Du and Z. Yuan, *Materials Letters* 58, 636 (2004).

26. M. Seifert, L. Schultz and V. Neu *J. Appl. Phys.* 106, 073915 (2009).

27. C. Patterson, D. Givord, J. Voiron and S. B. Palmer *J.Magn. Magn. Mater.* 54-57, 891 (1986).

28. H. Pang, L. Qiao and F. S. Li *Phys. Status Solidi B* 246, 1345 (2009).

29. N. G. Akdogan, G. C. Hadjipanayis and D. J. Sellmyer *J. Appl. Phys,* 105, 07A710, (2009).

30. V. M. Chakka, B. Altuncevahir, Z. Q. Jin, Y. Li and J. P. Liu *J. Appl. Phys.* 99, 08E912 (2006).

31. G. Herzer *IEEE Trans. Magn.* 26, 1397 (1990).

32. R. Skomski *J. Phys.: Condens. Matter* 15, R841 (2003).

33. F. Von Staa, K. A. Hempel, H. Artz, Y. Wang, J. Schneider, *J. Magn. Magn. Mater.* 157, 23 (1996).

Chapter 5

INTRINSIC PROPERTIES

Previous studies revealed novel behavior in the optical and magnetic properties of materials as the size decreases [1-3]. Of fundamental importance is the behavior of the magnetocrystalline anisotropy, saturation magnetization, Curie temperature and spin reorientation temperature in ferromagnetic systems; however, such behaviors are little explored in nanoparticles, although it has been well accepted that there is a size effect on the ferromagnetism of low-dimensional systems [4-12]. In the case of nanometer scale particles the surface/volume atoms ratio is large (50% surface atoms in 3 nm particles) and broken symmetry at surface/interface causes changes of (a) band structure, (b) atomic coordination number, and (c) lattice constant. Electronic environment/charge transfer also occurs at interface with (a) ligands, (b) other metals, and (c) insulators. All of these changes affect the intrinsic properties of the magnetic materials.

In this chapter, we have investigated the change in intrinsic magnetic properties such as magnetocrystalline anisotropy, Curie temperature, spin reorientation temperature and saturation magnetization with respect to microstructure and particle size.

5.1 Size and Temperature Dependence of Magnetocrystalline Anisotropy

5.1.1 $Nd_2Fe_{14}B$

The magnetocrystalline anisotropy (K_1 and K_2) of nanoparticles and micron powders was found by plotting the *M-H curves* and fitting to the Stoner-Wohlfarth model which is for non-interacting uniaxial single domain particles. Figures 5.1 shows the fitting of the high-field data to the Stoner-Wohlfarth model [13] for different nanoparticle sizes and flakes with nano-size grains. As seen in Figure, the model fits our experimental data very well on isolated single crystalline nanoparticles. As compared with the uniaxial single domain particles, we can see that the Stoner-Wohlfarth model (Chapter 2) cannot be applied to the micron size nanoflakes with 35 nm grains due to their polycrystalline nature with strong magnetic interaction among the grains.

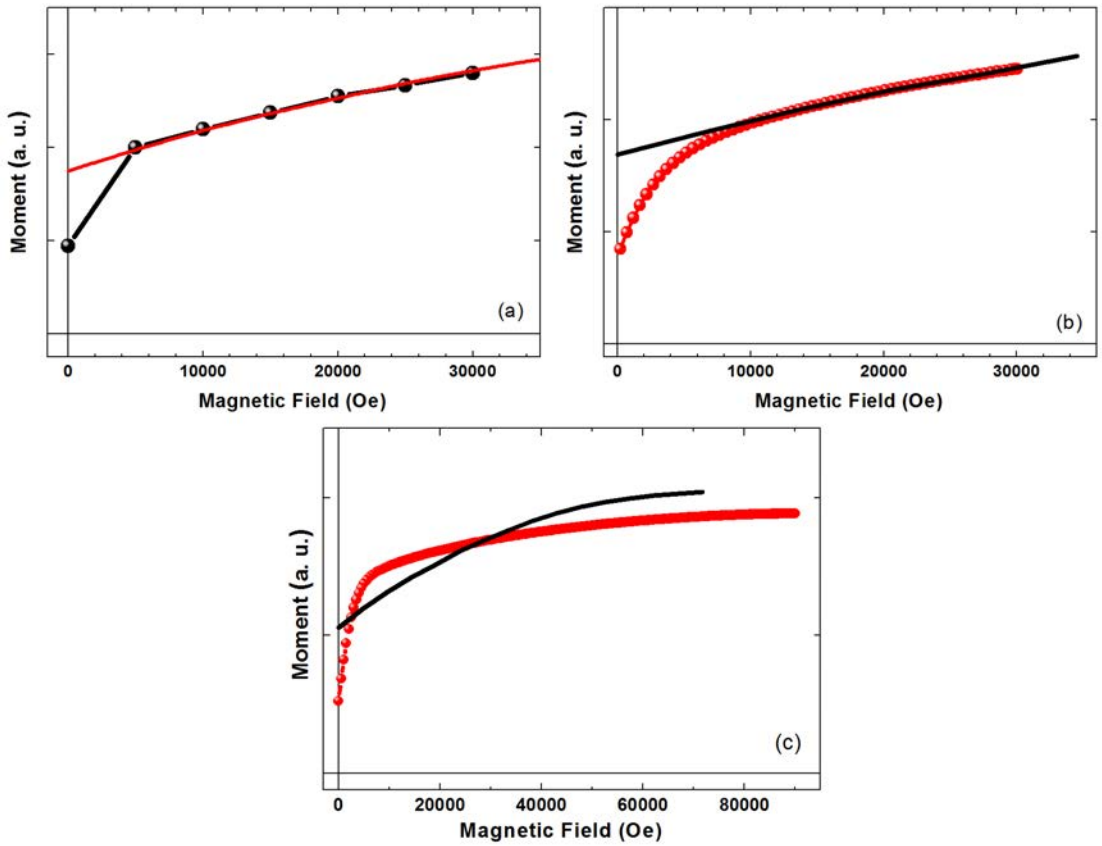

Figure 5.1 Fitting of the high field magnetic data to the Stoner-Wohlfarth model for nanoparticles with average size (a) 10 nm, (b) 25 nm and (c) nanoflakes with 35 nm grains (Table 4.1).

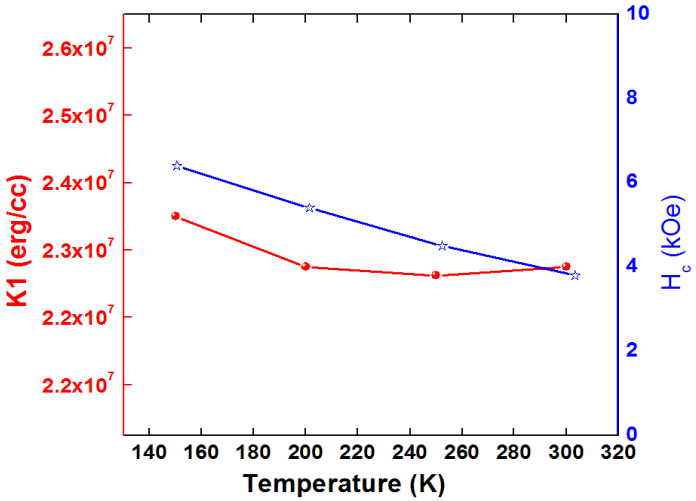

Figure 5.2 Magnetocrystalline anisotropy constants K_1 for 16 nm $Nd_2Fe_{14}B$ particles at different temperatures and corresponding coercivities.

Figures 5.2 shows the change in anisotropy constant (K_1) and coercivity values with temperature. Although the change in anisotropy is small within this temperature range, the coercivity follows the change in K_1, as expected.

In order to determine both K_1 and K_2, we have performed the analysis of the magnetization curves using the law of approach to saturation. The calculations are done on the magnetization curves (section 2.7.1) (Figure 5.3), which are taken at different temperatures and with the maximum applied field of 9T. The saturation magnetization M_s and K_1 can be found by plotting M versus $1/H^2$ (Figure 5.4) and extrapolating to $1/H^2 = 0$ (1). The slope of this curve gives the constants, A and B. To determine K_1 and K_2, M(H) curves were fitted to the equation:

$$M = M_S \left(1 - \frac{A}{H^2} - \frac{B}{H^3} - \cdots\right) \qquad (5.1)$$

The constants A and B (section 2.7.1) depend on the anisotropy constant K_1 and K_2

$$A = \frac{4}{15}\left(1 + \frac{16}{17}\frac{K_2}{K_1} + \cdots\right)\frac{K_1^2}{M_S^2}$$
$$B = \frac{16}{105}\left(1 + \frac{8}{3}\frac{K_2}{K_1} + \cdots\right)\frac{K_1^3}{M_S^3} \qquad (5.2)$$

Where K`s are the principal anisotropy constants. K_1 and K_2 values have been determined solving equation A and B eq. (5.2), simultaneously.

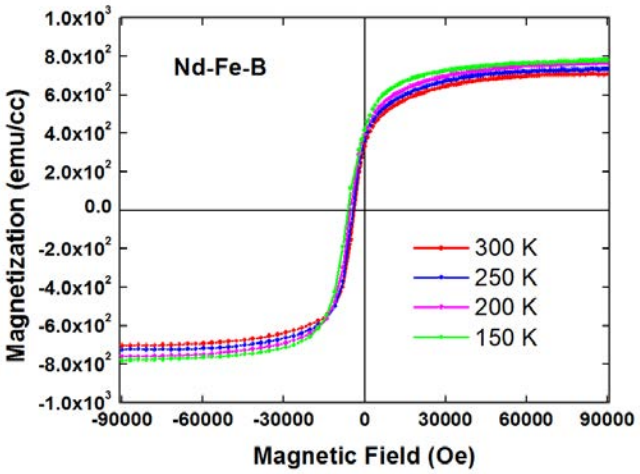

Figure 5.3 Hysteresis loops on randomly oriented 16 nm $Nd_2Fe_{14}B$ particles at different temperatures.

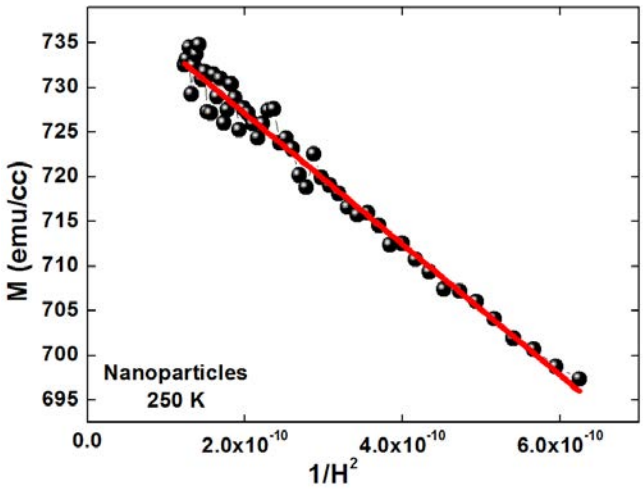

Figure 5.4 Magnetization as a function of $1/H^2$ for 16 nm $Nd_2Fe_{14}B$ particles. The saturation magnetization is determined by the Y-intercept of the M_s at high field.

The RT data gave the following two values of the anisotropy constants on micron powders; $K_1 = 4.72\ 10^7$ *ergs/cc* and $K_2 = 1.84\ 10^7$ *ergs/cc*. Calculations on nanoparticles (with average size of 16 nm) gave anisotropy constants which are lower than the micron powders; $K_1 = 2.1\ 10^7$ *ergs/cc* and $K_2 = 1.2\ 10^7$ *ergs/cc* (Figure 5.5 (a)). Anisotropy constants for bulk $Nd_2Fe_{14}B$ are $K_1 = 5\ 10^7$ *ergs/cc* and $K_2 = 2\ 10^7$ *ergs/cc* [14]. The lower anisotropies observed in the nanoparticles are attributed to size and surface effects. The estimated anisotropy constant values predicted by Stoner-Wohlfarth fit are in good agreement with values predicted by the law of approach to saturation. Theoretical calculations by [1-3] showed that disorder at the particle surface can lead to a substantial reduction in anisotropy.

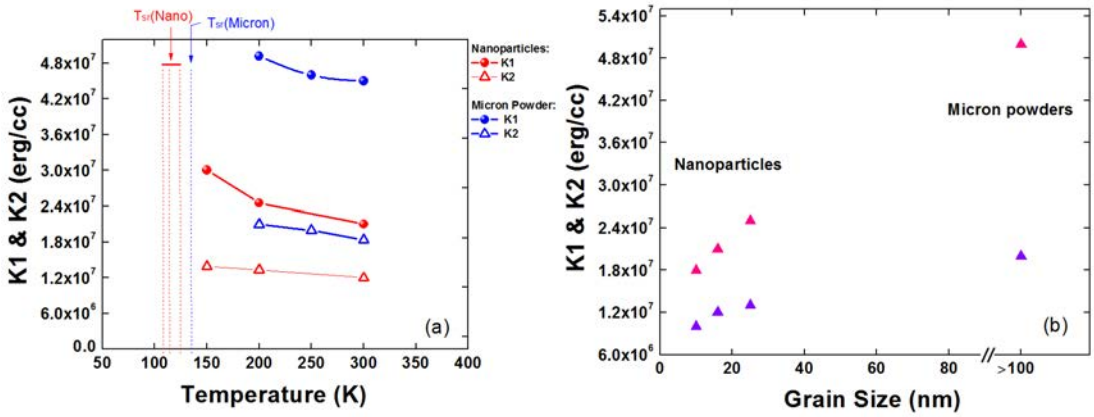

Figure 5.5 (a) Magnetocrystalline anisotropy constants K_1 and K_2 for 16 nm $Nd_2Fe_{14}B$ particles at different temperatures and (b) grain size dependences of the anisotropy constants K_1 and K_2.

Figure 5.5 (a) depicts the change in anisotropy constants K_1 and K_2 of 16 nm particles as compared to micron size powders at different temperatures. The change with temperature is very small and similar in both the particle size.

5.1.2 $Nd_2(Fe,Mn)_{14}B$

The resultant anisotropy of $Nd_2Fe_{14}B$ is reduced by Ni and Co substitution whilst it is not affected by Mn substitution in the composition range under consideration, which is due to the different site preference of substituted atoms [4].

We have also fitted the magnetization curves (Figure 5.6) to the law of approach to saturation (Figure 5.7), and determined the anisotropy constants, K_1 and K_2.

The data at 200 K gave the following two values of the anisotropy constants on micron powders; $K_1 = 4.72\ 10^7$ *ergs/cc* and $K_2 = 1.84\ 10^7$ *ergs/cc*. As in the case of

$Nd_2Fe_{14}B$, the same trend has been observed for the behavior of anisotropy for different particle sizes. Calculations on nanoparticles (with average size of 4.8 nm) estimated the anisotropy constants which are lower than the micron powders; $K_1 = 2.48\ 10^7$ *ergs/cc* and $K_2 = 0.98\ 10^7$ *ergs/cc*. As mentioned earlier, the lower anisotropies observed for the nanoparticles are due to size and surface effects.

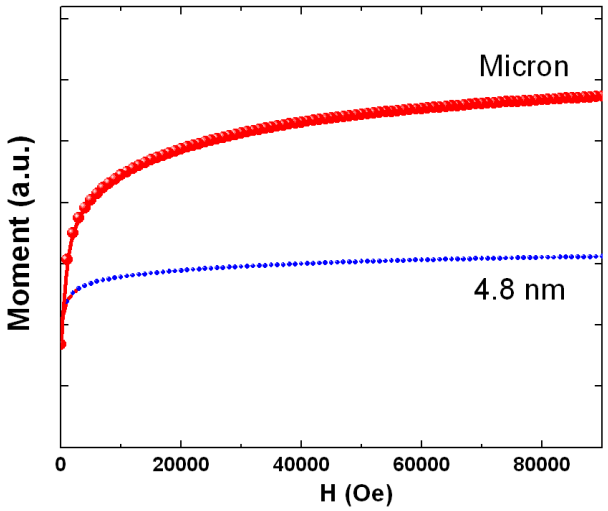

Figure 5.6 Hysteresis loops at 200 K on randomly oriented $Nd_2(Fe,Mn)_{14}B$ micron size powders and nanoparticles.

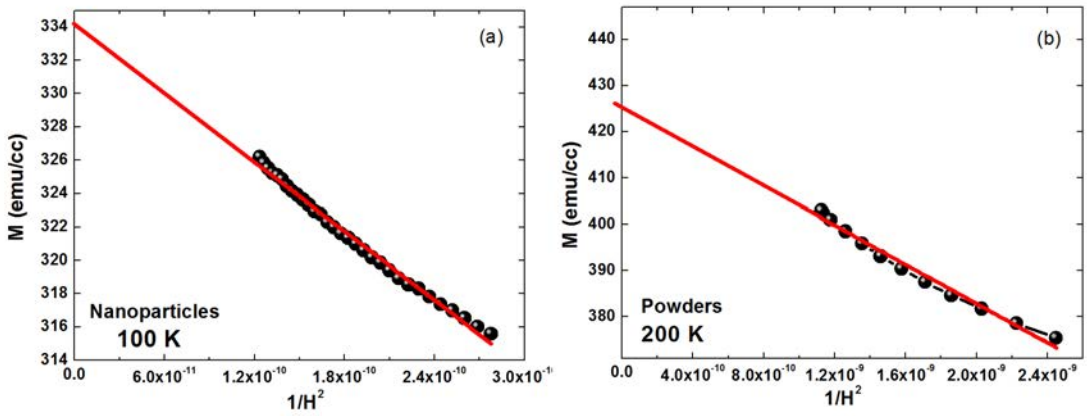

Figure 5.7 Fitting of high field magnetization data to the law of approach to saturation.

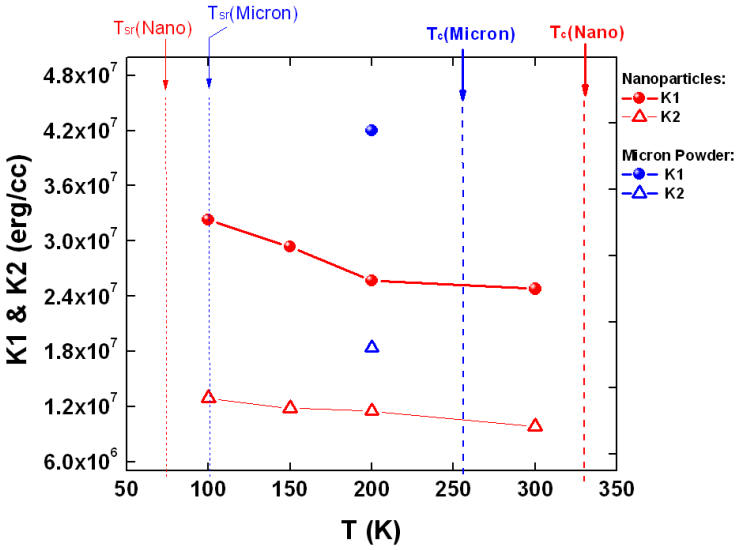

Figure 5.8 Magnetocrystalline anisotropy constants K_1 and K_2 for 4.8 nm $Nd_2(Fe,Mn)_{14}B$ particles at different temperatures.

Figure 5.8 depicts the change in anisotropy constants of nanoparticles as compared to micron size powders at different temperatures. A similar trend has been observed in these particles too. Lower K_1 and K_2 values have been observed for $Nd_2Fe_{11}Mn_3B$ nanoparticles as compared to micron size powders. The change of anisotropy with temperature is very slight as in the case of $Nd_2Fe_{14}B$.

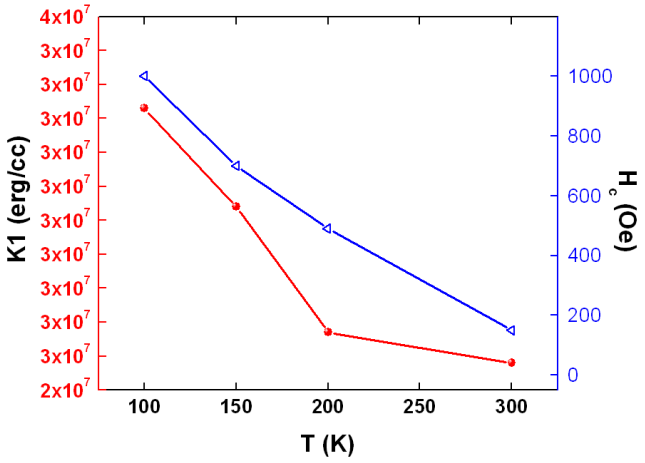

Figure 5.9 The change in K_1 and coercivity with temperature in $Nd_2(Fe,Mn)_{14}B$ particles.

The coercivity behavior with respect to temperature follows the change in anisotropy constants as in the case of $Nd_2Fe_{14}B$.

5.2 Size Dependence of Saturation Magnetization

Under a strong magnetic field, ferromagnetic materials are magnetized to their saturated state, where all the moments are aligned in the same direction as the applied field. The specific value of saturation magnetization (M_s) for different size

powders was determined from *M(H)* curve, after corrections to saturation magnetization for surfactant present at the surface of the particles.

The surfactant, which is used in the fabrication of nanoparticles, was washed away using mild alternating washing procedure as discussed in Chapter 3. Even after washing, there is at least a layer of surfactant on the surface of the particles, which is confirmed with FTIR measurements (Chapter 4). Due to the surfactant present at the surface of the particles, the magnetization needs to be corrected for the surfactant. The surfactant amount left at the surface can be estimated using thermo gravimetric analysis (TGA) by heating the sample and monitoring the weight loss. However, because of the high reactivity of rare-earth compounds at high temperatures, sample weight starts increasing as soon as the surfactant starts decomposing before it reaches its boiling point. Therefore, 8 wt% surfactant contribution to the mass was assumed which is the lowest limit of magnetization correction due to surfactant coating as it accounts for only one single layer of surfactant at the particle`s surface and does not account for the contribution from extra amount.

5.2.1 $Nd_2Fe_{14}B$

The M_s was found by fitting high field magnetization data (from 25 to 30 kOe) to the law of approach to saturation, and extrapolating the M versus $1/H^2$ (Figure 5.10) to zero.

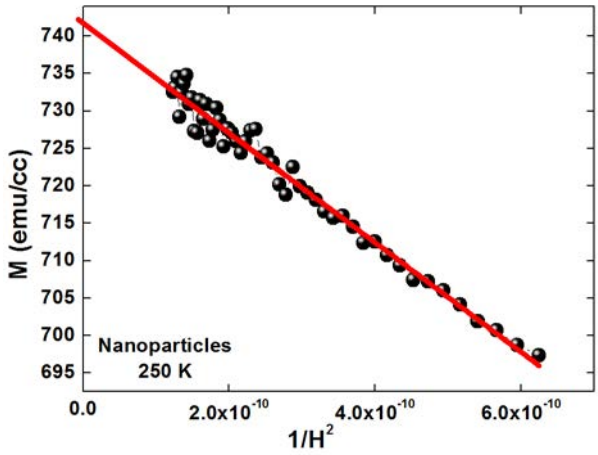

Figure 5.10 Magnetization as a function of $1/H^2$ for 16 nm $Nd_2Fe_{14}B$ particles. The saturation magnetization is determined by the Y-intercept of the M_s at high field.

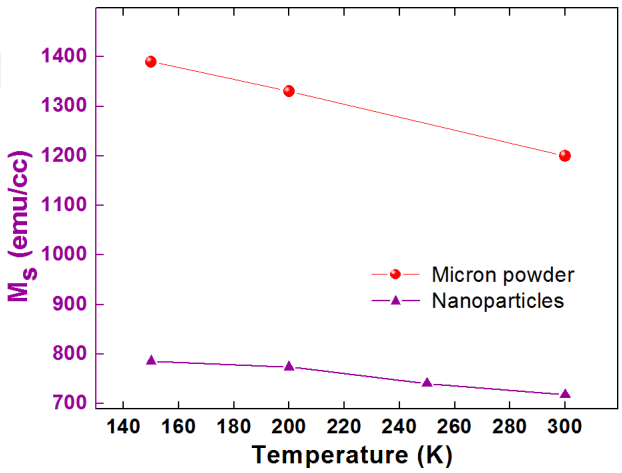

Figure 5.11 The change in saturation magnetization with temperature for micron size powders and 16 nm $Nd_2Fe_{14}B$ particles.

As seen in Figure 5.11, the saturation magnetization value for nanoparticles was found to be smaller as compared to the $Nd_2Fe_{14}B$ micron size powders. The

maximum value of M_s was found to be 60 % of the bulk in 16 nm particles. The main reasons for the lower value of saturation magnetization of anoparticles may be related to the non-collinearity of magnetic moments on the surfaces of the nanoparticles, finite size effects and spin canting [15]. Magnetic materials intrinsically possess magnetically disordered spin glass like layers near the surface due to the reduced spin–spin exchange coupling energy at the surface [16]. In case of small particles the higher surface to volume ratio being larger as compared to micron size particles facilitates this phenomena. Another reason for the lower M_s is the dilution of magnetization because of a larger amount of surfactant at the particle surface.

Figure 5.11 also shows the change in saturation magnetization with temperature. As the temperature decreases, thermal activation energy decreases thus the spins become more thermally stable and fluctuate less which in turn causes an increase in magnetization. The same behavior has been also observed for nanoparticles (Figure 5.11).

5.2.2 $Nd_2(Fe,Mn)_{14}B$

In a similar way, the M_s was found by fitting the high field magnetization data (from 25 to 30 kOe) to the law of approach to saturation, extrapolating the M versus $1/H^2$ (Figure 5.12) to infinite fields.

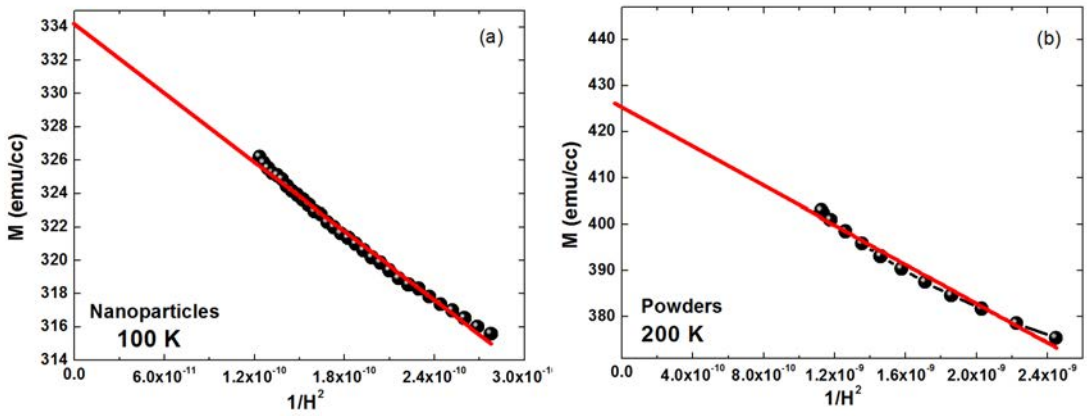

Figure 5.12 Magnetization as a function of $1/H^2$ for (a) micron size powders and (b) 4.8 nm $Nd_2(Fe,Mn)_{14}B$ particles. The saturation magnetization is determined by the Y-intercept of the M_s at high field.

Saturation magnetization studies have been done on pre-milled powders (micron size) and 4.8 nm particles to investigate the effect of different microstructures. Calculations have been applied taking the spin reorientation and Curie temperature into account (Figure 5.13). As seen in Figure 5.13, compared to the $Nd_2Fe_{14}B$ bulk value (~180 emu/g at 200 K), smaller saturation magnetization values have been observed for $Nd_2Fe_{11}Mn_3B$ powders (~ 45 emu/g at 200 K), which are attributed to the dilution of the magnetization due to the decrease in Fe content. The Mn-Fe distances are in the region less than 2.8 A, where antiferromagnetic coupling is expected [4] and a probable explanation is that the manganese atoms couple antiparallel to iron, resulting in a rapid decrease in the saturation moment.

Lower saturation magnetization values have also been observed for $Nd_2Fe_{11}Mn_3B$ nanoparticles as compared to micron size powders indicating again a

size effect on the saturation magnetization as discussed in the previous section (5.2.1) [15,16].

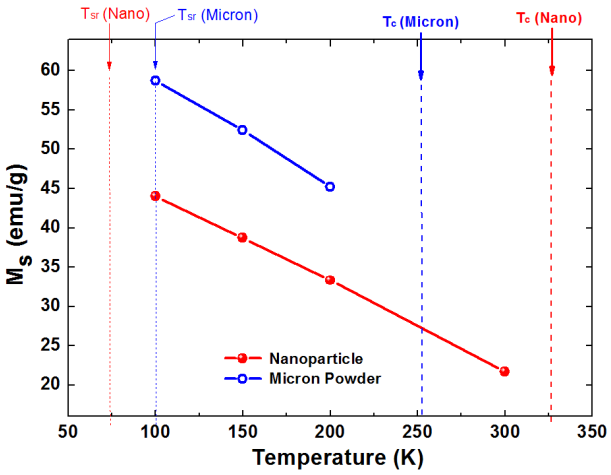

Figure 5.13 The change in saturation magnetization with temperature for micron size powders and 4.8 nm $Nd_2(Fe,Mn)_{14}B$ particles.

5.3 Curie Temperature

Previous studies have reported a decrease in Curie temperature in 2D systems (thin films) [17], which suggest that the nanoparticles in which all three dimensions are limited offer an interesting system for such studies. So far most studies reported have been focused on low-dimensional ferromagnets, which are granular thin films, and nanocomposites, where the polycrystalline granular structures disguise the authentic effect of particle size [18]. Therefore, it is very important to understand the correlation between the Curie temperature and particle size in isolated ferromagnetic nanoparticles.

The study of magnetization at high temperatures in rare earth transition-metal nanoparticles and nanoflakes presents a great challenge due to the very high reactivity of these materials. This makes it difficult to study the magnetic ordering behavior of these materials which in bulk have Curie temperature around 585 K.

5.3.1 Attempts to Measure Curie Temperature of $Nd_2Fe_{14}B$ Nanoflakes and Nanoparticles

The Curie temperature of arc-melted and crushed $Nd_2Fe_{14}B$ ingot powder was determined by measuring the temperature dependence of dc magnetization. As seen in Figure 5.14, the T_c is found to be 585 K, which is close to the values reported in the literature [19].

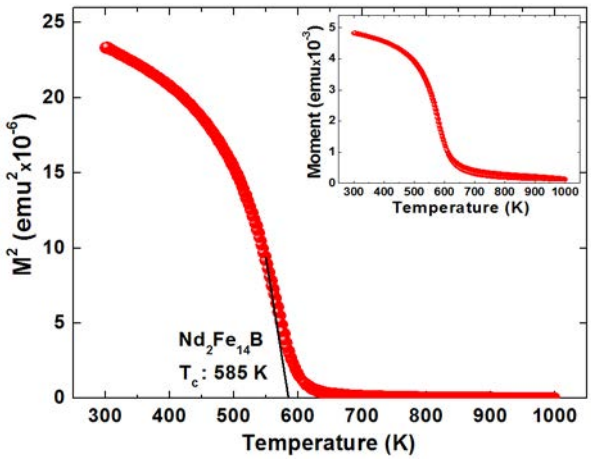

Figure 5.14 M^2 as a function of temperature, T, for arc-melted and crushed $Nd_2Fe_{14}B$ ingot powder, inset: Magnetization vs. temperature.

Measurements on SA-HEBM flakes using OA as the surfactant revealed that flakes being nano-thin are very prone to oxidation. As seen in Figure 5.15, the powder is going through series of phase changes as the temperature increases. As discussed in

Chapter 3, Oleic acid has "O" molecule at the end of the group where it attaches to the surface of the particles and the boiling point of OA is around 350^{o}C (623 K). Therefore, it is highly likely that the OA on the surface starts oxidizing the sample once the temperature reaches around 500 K. Another oxidant agent in high temperature magnetization measurements is the water-based cement, which is in contact with the powder sample.

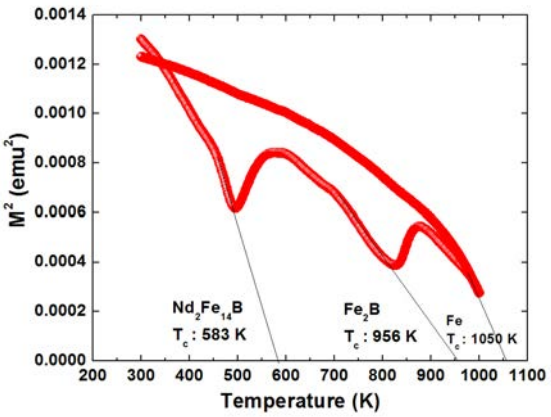

Figure 5.15 M^2 as a function of temperature, T, for SA-HEBM $Nd_2Fe_{14}B$ flakes using OA as the surfactant.

In an attempt to do more reliable M vs. T measurements, the $Nd_2Fe_{14}B$ flakes were embedded in fine Ag (and Cu) matrix. As seen in Figure 5.16, the flakes still get oxidized despite the matrix. Then we used a surfactant, which does not contain any oxygen molecule, tryloctylamine (TOA).

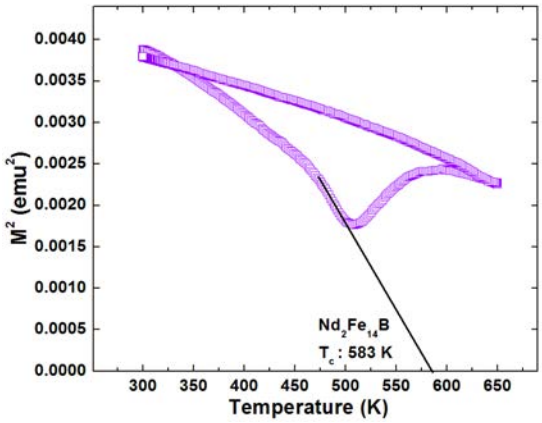

Figure 5.16 M^2 as a function of temperature, T, for SA-HEBM $Nd_2Fe_{14}B$ flakes using OA as the surfactant and embedded in Ag matrix.

The flakes, which are produced using the TOA as the surfactant, were used in determining the Curie temperature. Magnetization vs. temperature measurement was carried out on flakes embedded in Ag. The data presented in Figure 5.17 show that the oxidation of the flakes is inevitable. Later measurements on TOA (Chapter 4) milled flakes revealed that TOA is not as compatible surfactant as OA. It appears that the TOA does not functionalize the flakes fully. Therefore, the flakes oxidized through the bare non-functionalized surface areas in this case.

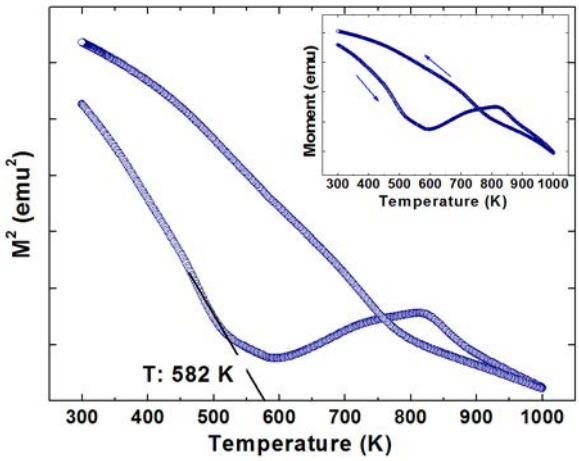

Figure 5.17 M^2 as a function of temperature, T, for SA-HEBM $Nd_2Fe_{14}B$ flakes using TOA as the surfactant and embedded in Ag matrix, inset: Magnetization vs. temperature.

Since the flakes being nano-thin are highly prone to oxidation, one had to employ another method in order to understand the correlation between the Curie temperature and particle size in isolated ferromagnetic nanoparticles. As we will discuss below, we used the Mn substituted Nd-Fe-B alloy which has a much lower Curie temperature and therefore does not need to be heated to high temperatures avoiding thus the oxidation problem.

5.3.2 Size Dependent Curie Temperature of $Nd_2(Fe,Mn)_{14}B$

It is well known that Mn substitution for Fe in $Nd_2Fe_{14}B$ compound decreases the Curie temperature to a temperature range that allows for reliable measurements to be made [4]. Curie Temperature decreases rapidly when iron is replaced by manganese, indicating a weakening of the Fe-Fe magnetic interaction. In $R_2Fe_{14-x}Mn_xB$ systems, it is postulated that the manganese atoms also replace a portion of the

8j and $16k_1$ iron atoms and the manganese couple antiparallel to the iron, resulting also in a rapid decrease of the Curie temperature.

The Curie temperature was determined by employing two different methods; *(i)* the temperature dependence of dc magnetization and *(ii)* ac susceptibility. We first determine the Curie point in the most direct manner possible, by measuring the spontaneous change in magnetization in a small applied field as the temperature varies through T. As seen in Figure 5.18 (a), temperature dependence of magnetization reveals a very small shift in transition temperature as the particle size and morphology change from the starting ingot to 100 nm thin flakes with a 10^2 aspect ratio. On the other hand, the effect is quite considerable when all three dimensions are decreased (Figure 5.18 (b)). The Curie temperature increases up to 338 K for the 4.8 nm particles as compared to 255 K for the ingot powder. Figure 5.19 (a) presents a systematic investigation of the ac susceptibility of $Nd_2Fe_{14-x}Mn_xB$ nanoparticles with different sizes as a function of temperature in the temperature range from 200 to 345 K and using a magnetic field with 5 Oe amplitude. The data corroborate the magnetization versus temperature measurements and we have not observed any shift in the positions of the peak with increase in the measuring frequency, which indicates that the nanoparticles are not in the superparamagetic regime [20]. Data presented in Figure 5.19 (b) (normal-log plot) shows the change in Curie temperature starting from the reference powder.

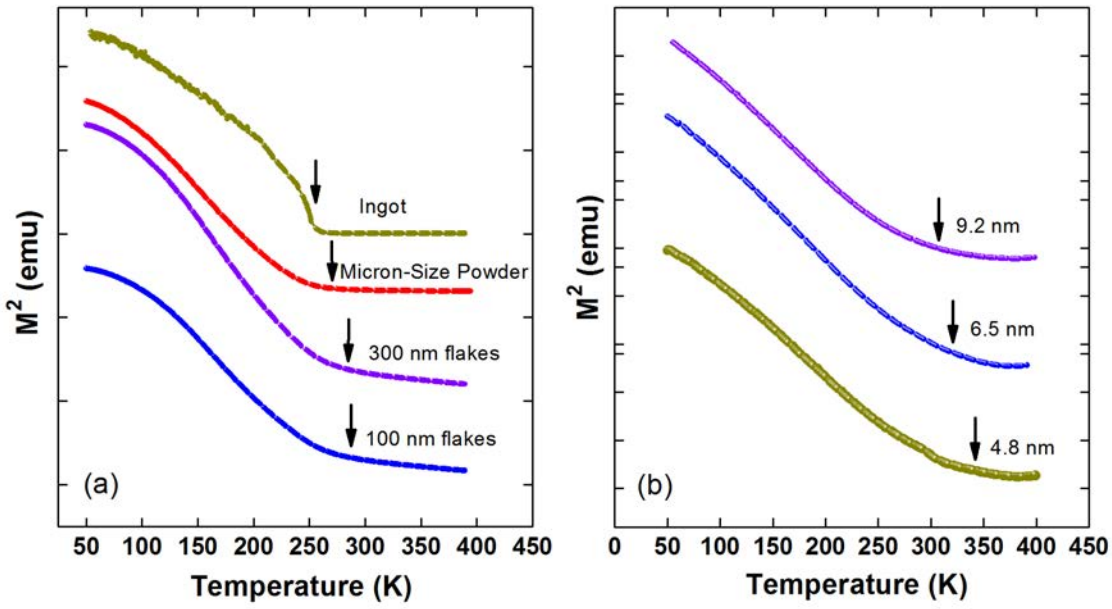

Figure 5.18 Magnetization, M, as a function of temperature, T, for (a) different $Nd_2(Fe,Mn)_{14}B$ powders and (b) nanoparticles with different size.

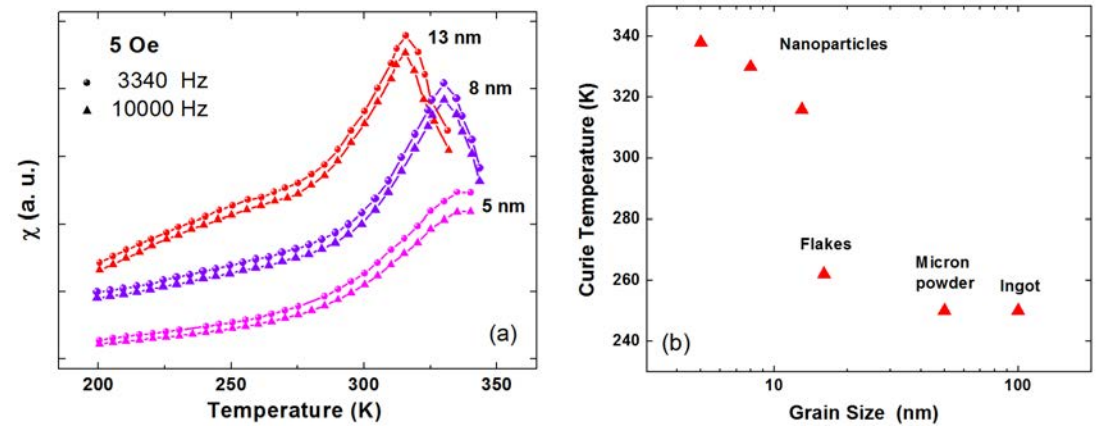

Figure 5.19 (a) Temperature dependences of the ac susceptibilities χ' (real component) at the measuring frequencies and (b) grain size dependences of the Curie temperatures in $Nd_2(Fe,Mn)_{14}B$.

5.3.2.1 Finite Size Scaling Theory

We have investigated the Curie temperature behavior of nanoparticles in terms of predictions of finite-size scaling theory [21-25]. The theory predicts that the change in the transition temperature from that of the bulk depends on the size of the system in the following fashion:

$$\frac{[T_c - T_c(\infty)]}{T_c(\infty)} = {}^{+}_{-}(d/d_o)^{-\lambda} \qquad (5.3)$$

Where d is the particle size and λ is predicted to be related to the correlation length exponent through the expression λ = 1/v. $T_c(\infty)$ is the Curie temperature of the starting powder as the reference material. Figure 5.20 presents the plot of $[T_c - T_c(\infty)]/T_c(\infty)$ versus d. Fitting the data with eq. (5.3), amplitude (d_o) is found to be 2.45 ± 0.09 nm which is roughly twice the lattice spacing of 2:14:1 phase and $v = 0.72 \pm 0.08$, which agrees well with those predicted by the isotropic three-dimensional Heisenberg model [22] which predicts v in the range from $v = 0.65 \pm 0.07$ to $v = 0.733 \pm 0.02$. Both parameters fulfill their identification. Hence, since the finite-size-scaling fit yields both a reasonable exponent and amplitude, it suggests that finite-size scaling depicts the change in T_c well.

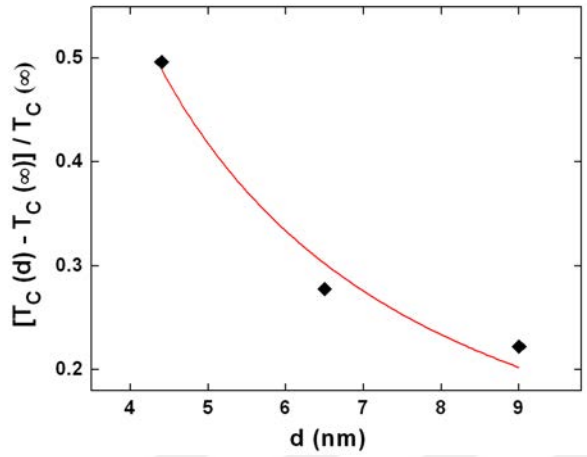

Figure 5.20 Reduced Curie temperature shift vs. particle diameter. Solid line is fitted by Eq. (5.3) with $\lambda = 1.42$ and $d_o = 2.45$ nm.

5.4 Size Dependence of Spin Reorientation Temperature

5.4.1 $Nd_2Fe_{14}B$

$Nd_2Fe_{14}B$ is a typical compound with a spin reorientation temperature about 135 K. In the bulk material, this transition from a collinear magnetic structure, in which the magnetization is parallel to the c-axis, to a magnetic structure where the magnetization is tilted away from the c-axis occurs at 135 K [26].

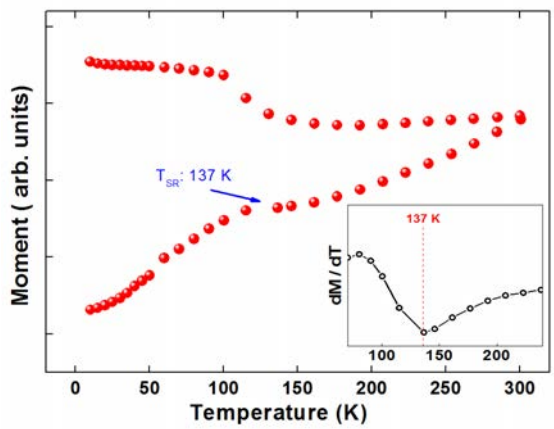

Figure 5.21 Magnetic moment, M, as a function of temperature, T for $Nd_2Fe_{14}B$ alloy sample.

Previous studies, which have been reported to date on the spin reorientation temperature, revealed a strong dependence on particle size [7,27,28]. The magnetization of the starting ingot powders and nanoparticles were measured between 5 and 300 K in a field of 150 Oe after cooling the samples in zero magnetic field (ZFC) and then cooling in a magnetic field of 150 Oe (FC). ZFC and FC curves (Figure 5.21) show the typical behavior for $Nd_2Fe_{14}B$ alloy sample. In ZFC curve, temperature dependence of magnetization reveals a discontinuity for both nanoparticles and nanoflakes (Figure 5.22 (a) and (b)), which is attributed to the spin reorientation temperature.

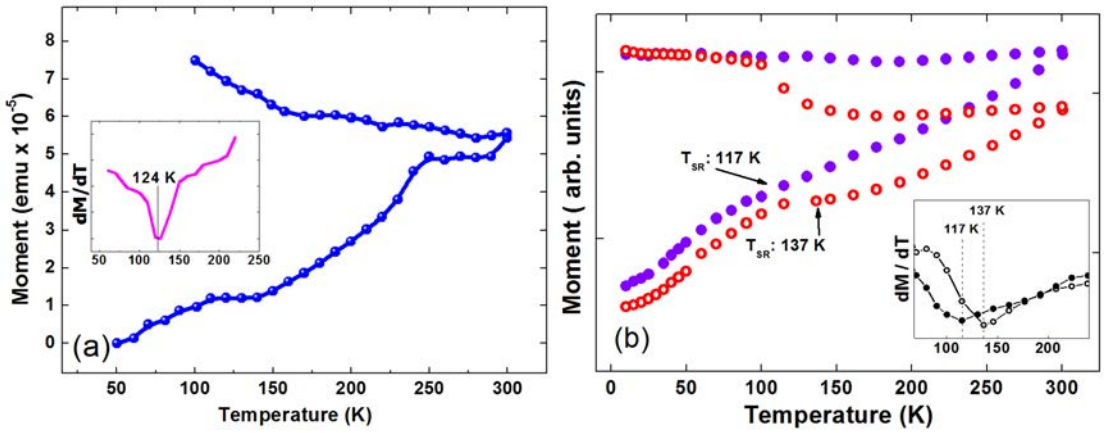

Figure 5.22 Magnetic moment, M, as a function of temperature, T (a) for 25 nm particles (b) for 10 nm $Nd_2Fe_{14}B$ particles (filled circles) and for nanoflakes (open circles). The arrows indicate the corresponding temperatures for which spin reorientation is assumed. Insets: Derivatives of M vs. T curves.

Data presented in Figure 5.23 (normal-log plot) shows the change in spin reorientation temperature starting from the reference powder. The lower transition temperatures observed for the nanoparticles (124 K to 117 K) when compared to 137 K for the flakes, suggests a likely size effect on the spin reorientation temperature. The correlation between the particle size and the effect on spin-reorientation temperature may be attributed to the change in magnetocrystalline anisotropy due to the surface modification. Laosiritaworn et. al. [29] predicted from a Monte Carlo simulation that in the nanostructures strain reduces the spin-reorientation temperature significantly due to the fact that strain may change the anisotropy energy.

The further investigation on spin reorientation temperature was extended to other systems, such as $Nd_2(Fe,Mn)_{14}B$ and $NdCo_5$.

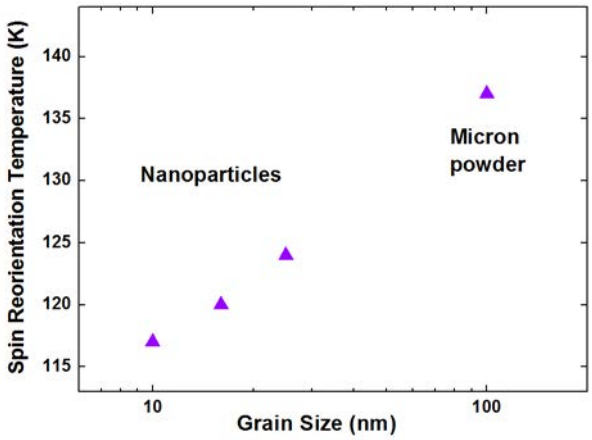

Figure 5.23 Spin reorientation temperature for micron size $Nd_2Fe_{14}B$ powders and nanoparticles.

5.4.2 $Nd_2(Fe,Mn)_{14}B$

Mn substitution in bulk $Nd_2Fe_{14}B$ decreases the spin reorientation temperature down to 100 K for x~3 [4]. Previous studies, which have been reported to date on the spin reorientation temperature, revealed a strong dependence on the particle size [7, 30,31]. The temperature dependence of the ac susceptibility was measured from 20 to 140 K using a magnetic field with amplitude of 5 Oe. Although we have not observed a considerable change in T_{sr} for nanoparticle sizes from 5 to 10 nm, the change is quite significant when compared to the starting powders. The lower transition temperatures (75 to 67 K) observed for the nanoparticles when compared to bulk, suggests a likely size effect on the spin reorientation temperature as discussed in the previous section (5.4.1) (Figure 5.24 (normal-log plot)).

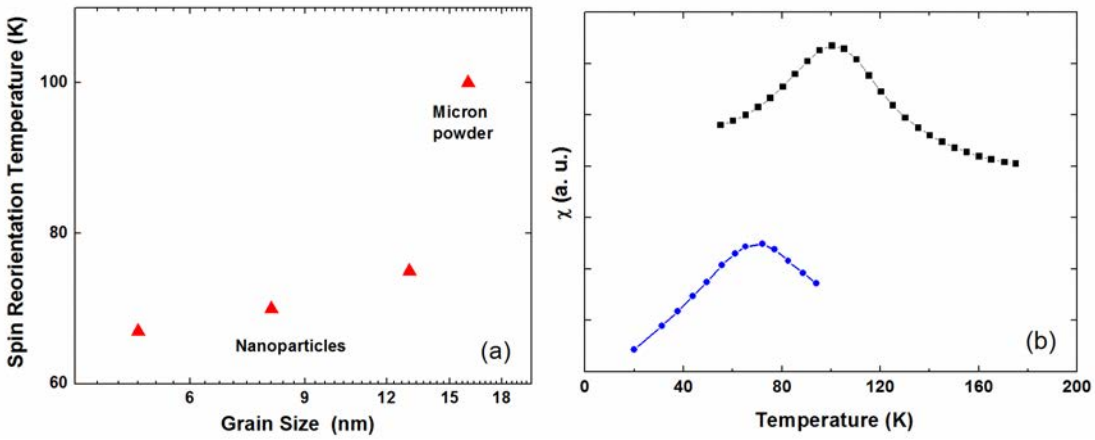

Figure 5.24 (a) Spin reorientation temperature for micron size $Nd_2(Fe,Mn)_{14}B$ powders and nanoparticles and (b) Temperature dependences of the ac susceptibilities χ' (real component) on micron powders and nanoparticles.

5.4.3 $NdCo_5$

$NdCo_5$ is a unique alloy because of its complex magnetic ordering behavior at different temperatures. Bulk $NdCo_5$ has a hexagonal $CaCu_5$ structure with the c-axis as the easy direction of magnetization above 290 K. Below this temperature the moments rotate, in the *ac* plane, and below 245 K the a-axis in the basal plane becomes the easy-axis. The reason for this behavior is that in rare-earth intermetallics, both the RE and Co sublattices contribute to the total magneto-crystalline anisotropy and in some cases the different temperature dependencies of these contributions lead to a change in the easy direction of magnetization with temperature. In $NdCo_5$, the Nd sublattice favors an a-axis anisotropy at low temperature, whereas the Co sublattice has uniaxial anisotropy, which dominates at high temperature [32-34].

To investigate the spin reorientation behavior and determine the transition temperatures T_{SR1} and T_{SR2}, we measured the temperature dependence of magnetization in the temperature range of 50 to 300 K. For this purpose, the sample

was magnetized along the c-axis at 300 K in a 20 kOe field. Starting from 300 K, the sample was cooled down to 50 K while measuring the magnetization parallel to the c-axis. A magnetization increase has been observed until 288 K where the change in anisotropy starts taking place; then as soon as the easy cone opens, the measured projection of the magnetization onto the *c*-axis decreases and finally (below 249 K) it reaches saturation when the *a*-axis becomes the easy axis due to a perpendicular orientation between the measurement axis and the easy magnetization axis (Figure 5.25 (a)) [32-34].

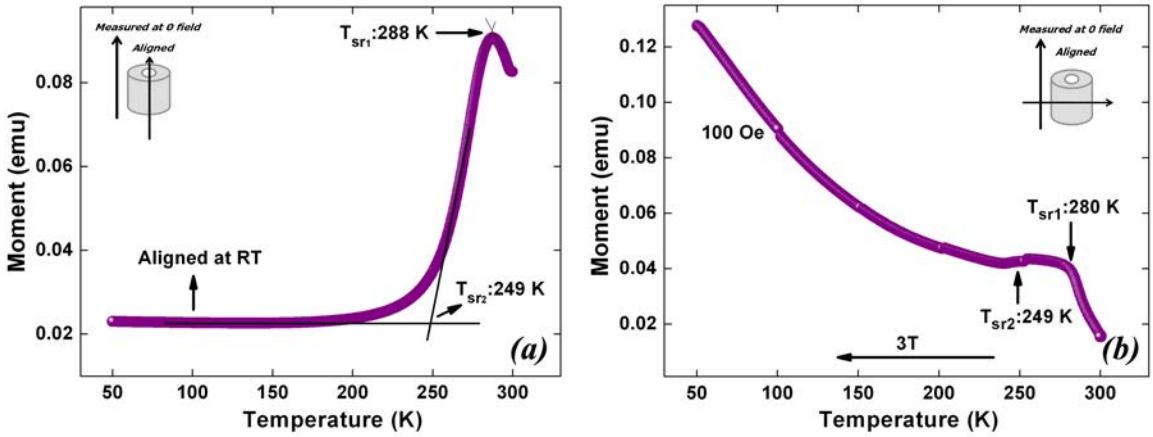

Figure 5.25 Magnetic moment, M, as a function of temperature, T, on field aligned $NdCo_5$ powders measuring the magnetization, (a) parallel to the c-axis at "0" field and (b) perpendicular to the c-axis measured at "100 Oe" field.

In another experiment, the magnetization was measured perpendicular to the alignment direction where the sample was field cooled and then measured at 100 Oe (Figure 5.25 (b)). We have done the same experiment on single crystalline ingot powder where we have seen similar transition temperatures as shown in Figure 5.25

(a). In this case, we have observed a drop in magnetization due to lack of perfect alignment of a-axis.

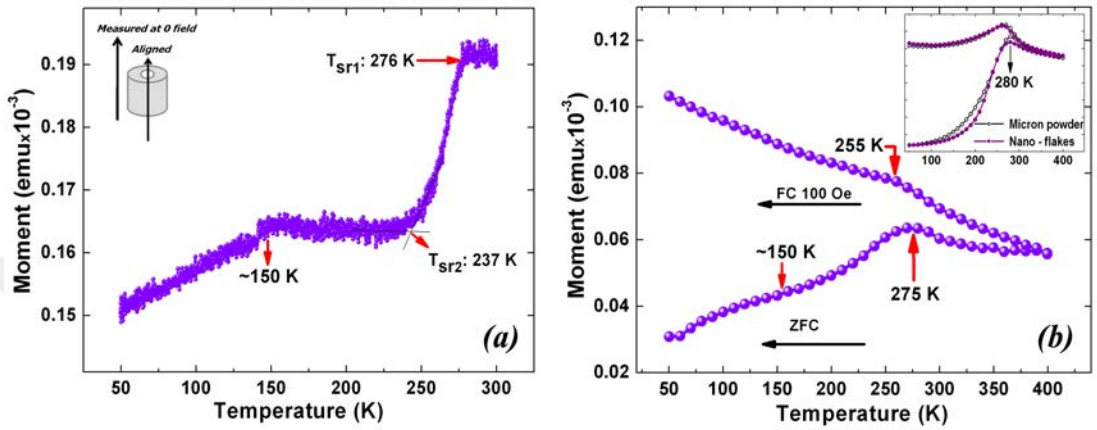

Figure 5.26 Magnetic moment, M, as a function of temperature, T, (a) on field-aligned $NdCo_5$ nanoparticles measured at zero-field and (b) on random nanoparticles, inset: Magnetic moment, M, as a function of temperature, T on random powders (ZFC and FC curves).

Compared to the powders and bulk samples, smaller spin reorientation values have been observed for the nanoparticles of 7 nm size. The T_{SR1} and T_{SR2} transition temperatures observed for the nanoparticles are 276 K and 237 K, respectively. These values are lower when compared to the 290 K and 245 K values of bulk, indicating a likely size effect on the spin reorientation temperatures (Figure 5.26 (a)) [29]. When the temperature is further decreased, a discontinuity in the M vs. T has been observed at 150 K. This may be related to a new magnetic transition, possibly to an easy axis, which can also explain the high coercivity (3 kOe) of nanoparticles observed at 50 K (Figure 4.12 (b)). Figure 5.26 (b) shows the M vs. T on randomly oriented nanoparticles. Compared to M vs. T on randomly oriented flakes (Figure 5.26 (b)

inset), we have observed a different behavior on the ZFC curve, a discontinuity around 150 K (like in the case of aligned M vs. T on nanoparticles, Figure 5.26 (a)).

5.5 Summary

In this chapter, we have investigated the change in intrinsic magnetic properties such as magnetocrystalline anisotropy, Curie temperature, spin reorientation temperature and saturation magnetization with respect to microstructure and particle size. Intrinsic properties showed different behavior for different particle morphologies as compared to bulk.

Lower K_1 and K_2 and saturation magnetization values have been observed for RE-TM nanoparticles as compared to micron size powders, which indicate a strong size effect due to size and surface effects.

The effect of particle size on Curie temperature was investigated on Mn substituted $Nd_2Fe_{14}B$ alloys which in bulk have a Curie temperature, close to room temperature avoiding thus the oxidation problem. Two types of methods have been employed to determine the Curie temperature of $Nd_2Fe_{14-x}Mn_xB$ powders and nanoparticles. According to our findings, we have observed an enhancement in Curie temperature for the first time for the rare-earth based compounds when all three dimensions are reduced without any change in the composition and structure. The enhancement in Curie temperature from that of the bulk is well described by the finite-size-scaling formula with proper exponent and characteristic microscopic dimension.

The $Nd_2Fe_{14}B$, $Nd_2Fe_{14-x}Mn_xB$ and $NdCo_5$ nanoparticles showed lower spin reorientation temperatures as compared to bulk. The lower anisotropy constants have

been observed for nanoparticles may be the reason for lower spin reorientation temperatures.

REFERENCES

1. R. P. Andres, R. S. Overback, W. L. Brown, L. E. Brus, W. A. Goddard, A. Kaldor, S. G. Louie, M. Moscovitis, P. S. Peercy, S. J. Riley, R. W. Seigle, F. Spaepen, and Y. Wang *J. Mater. Res.* 4, 704 (1989).

2. C. M. Schneider, P. Bressler, P. Schuster, and J. Kirschner *Phys. Rev. Lett.* 64, 1059 (1990).

3. A. Gavrin, J. R. Childress, C. L. Chien, B. Martinez and M. B. Salamon *Phys. Rev. Lett.* 64, 2438 (1990).

4. F. Bolzoni, F. Leccabue, O. Moze, L. Paret and M. Solzi *J. Magn. Magn. Mater.* 67, 373-377 (1987).

5. W. Kraus and G. J. Nolze *Appl. Crystallogr.* 29, 301 (1996).

6. G. K. Williamson and W. H. Hall *Acta Metall.* 1, 22 (1953).

7. N. G. Akdogan, G. C. Hadjipanayis and D. J. Sellmyer *Nanotechnology* 21, 295705 (2010).

8. M. E. McHenry and D. E. Laughlin Acta Mater. 48, 223 (2000).

9. G. C. Hadjipanayis J. Magn. Magn. Mater. 200, 373 (1999).

10. O. Gutfleisch, M. A. Willard, E. Bruck, C. H. Chen, S. G. Sankar and J. P. Liu *Adv. Mater. 23*, 821 (2011).

11. R. Skomski and D.J. Sellmyer *J. of Rare Earths* 27, 675 (2009).

12. O. Akdogan, W. Li, G. C. Hadjipanayis, D. J. Sellmyer *J. Nanopart. Res. 13*, 7005 (2011).

13. E. C. F. R. S. Stoner, E. P. Wohlfarht, *Phil. Trans. R. Soc. A 240*, 599 (1948).

14. T. Bublat and D. Goll *J. Appl. Phys.* 108, 113910 (2010).

15. C. B. Rong, D. R. Li, V. Nandwana, N. Poudyal, Y. Ding, Z. L. Wang, H. Zeng, and J. P. Liu *Adv. Mater.* 18, 2984 (2006).

16. M. P. Morales, S. Veintemillas-Verdaguer, M. I. Montero and C. Serna *J. Chem. Mater.* 11, 3058 (1999).

17. A. F. Ferdinand and M. E. Fisher *Phys. Rev.* 185, 832 (1969).

18. H. Zeng, R. Sabirianov, O. Mryasov, M. L. Yan, K. Cho and D. J. Sellmyer *Phys. Rev. B: Condens. Matter Mater. Phys.* 66, 184 (2002).

19. Cullity, B.D. *Introduction to Magnetic Materials.* Addison-Wesley: Reading, MA, 1972.

20. M. S. Seehra, V. Singh, P. Dutta, S. Neeleshwar, Y. Y. Chen, C. L. Chen, S.W. Chou and C. C. Chen *J. Phys. D: Appl. Phys.* 43, 145002 (2010).

21. M. N. Barber, in Phase Transitions and Critical Phenomena, edited by C. Domb and J. L. Lebowitz (Academic, New York, 1983), Vol. 8, p. 145.

22. S.N. Kaul *J. Magn. Magn. Mater.* 53, 5 (1985).

23. G. A. Y. Allan *Phys. Rev. B* 1, 1 (1970).

24. R. F. Sabiryanov and S. S. Jaswal *Phys. Rev. B* 79, 1 (1970).

25. Z. X. Tang, C. M. Sorensen, K. J. Klabunde and G. C. Hadjipanayis *Phys. Rev. B* 67, 25 (1991).

26. K. H. J. Buschow *Rep. Prog. Phys.* 54, 1123 (1991).

27. X. C. Kou, M. Dahlgren, R. Grossinger and G. Wiesinger *J. Appl. Phys.* 81, 4428 (1997).

28. C. Rong, N. Poudyal and J. P. Liu *Phys. Lett. A* 374, 3967 (2010).

29. Y. Laosiritaworn, R. Yimnirun and J. Poulter *Current Appl. Phys.* 6, 469 (2006).

30. G. Z. Xie, Z. J. Tian, Z. Yu, B. X. Gu, M. Lu and Y. W. Du *J. Magn. Magn. Mater.* 251, 109 (2002).

31. G. Xie, S. Yin, F. Zhang, P. Lin, B. Gu, M. Lu, Y. Du and Z. Yuan *Materials Letters* 58, 636 (2004).

32. M. Seifert, L. Schultz, and V. Neu *J. Appl. Phys.* 106, 073915 (2009).

33. C. Patterson, D. Givord, J. Voiron and S. B. Palmer *J.Magn. Magn. Mater.* 54-57, 891 (1986).

34. H. Pang, L. Qiao and F. S. Li *Phys. Status Solidi B* 246, 1345 (2009).

Chapter 6

HARD MAGNETIC PROPERTIES

6.1 Introduction

Nanometer scale magnetic particles exhibit a variety of unique magnetic properties that are drastically different from those of their bulk counterparts. Differences in properties have been attributed to size and surface/interface effects. The intrinsic properties have been discussed in Chapter 5. In this chapter, we focused on the hard magnetic properties.

One of the important extrinsic parameters of permanent magnets is coercivity. As the particle size is reduced, there is a critical size corresponding to a transition from multi-domain to single domain state where coercivity increases with a $D^{-1/2}$ dependence, until it reaches a maximum at the single-domain particle size. With further reduction in size, particles become superparamagnetic [1-4]. Coercivity being an extrinsic property strongly depends on the microstructural properties of the material. Coercivity is also controlled by the impurities on the surface of the particles, such as dents scratches, voids and etc., which are acting as nucleation sites. As the particle size decreases, the number of impurities on the surface decrease and this facilitates the initial coercivity increase [5].

Recent studies reported a considerable progress in the synthesis of Sm-Co [6-8] and Nd-Fe-B [6, 9,10] nanoparticles via surfactant-assisted ball milling; so far, however, the room-temperature coercivity of the as-synthesized nanoparticles with a

size below 10 nm did not exceed 0.1 kOe [10]. In this chapter, the change in hard magnetic properties with respect to size and microstructure has been discussed in the intermetallic compounds that have been investigated in this thesis.

6.2 Nanoflakes

6.2.1 $Nd_2Fe_{14}B$

6.2.1.1 Size Dependence of Coercivity and M_r in wet-milled Precursor Powders

Hysteresis loops of the pre-milled powders (Figure 4.4), measured parallel ($M_{\parallel}$) and perpendicular ($M_{\perp}$) to alignment direction, can be seen in Figure 6.1. The milling time has changed from 15 min to 4 h. As seen in Figure 6.1, after 15 min of wet milling the texture of the powders (as seen from the difference in $M_{\parallel}$ and $M_{\perp}$ curves) is decreasing as the milling continued. After 4 h, grain size decreases to 18 nm (Table 4.1) and texture completely disappears and this corresponds to a polycrystalline powders with mostly randomly oriented grains. The increase in the high-field slope further suggests polycrystallinity. The polycrystallinity during milling is usually being induced via coalescence of the particles and/or via formation of new (sub)grains [11-14]. When compared to argon milling [15] where the texture is lost in the earlier stages of milling, in wet milling, the loss of texture occurs at longer times since the agglomeration is strongly suppressed by the heptane media.

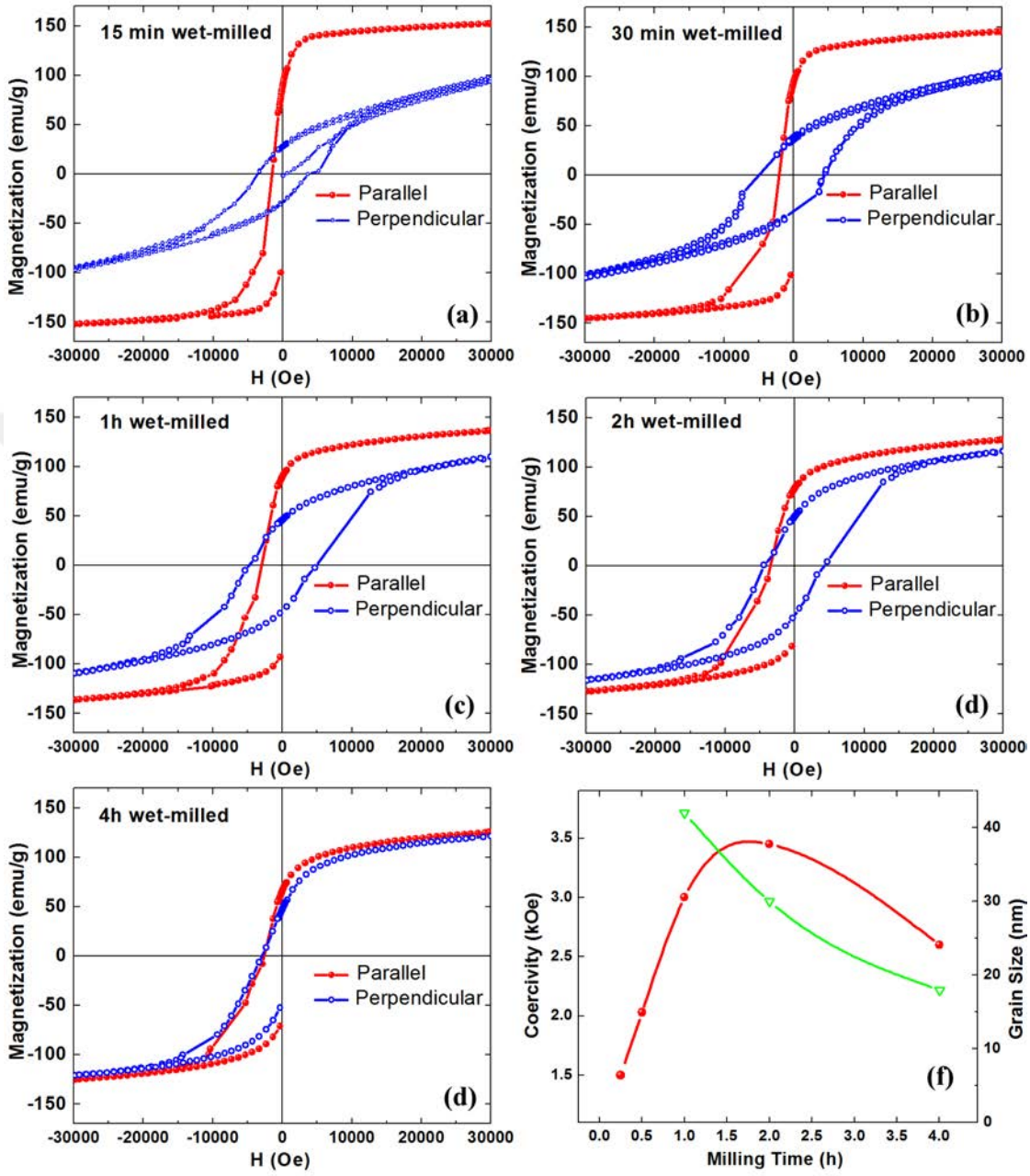

Figure 6.1 The hysteresis loops of the pre-milled $Nd_2Fe_{14}B$ powders for different times, measured parallel and perpendicular to the alignment direction. (a) to (e). (f) The change in coercivity ($H_{c\parallel}$) with milling.

As seen in Figure 6.1 (f), the coercivity initially increases up to around 3.5 kOe due to initial particle size refinement (as discussed in section 2) and then decreases with further milling. Traditionally, increase of remanence and decrease of coercivity must be expected in a nanocrystalline ferromagnet as the direct result of intergranular exchange coupling [16,17]. However, M_r and reduced M_r of the powders do not exhibit any enhancement (Figure 6.2). The M_r/M_s data show randomization/polycrystallinity of grains to a reduced remenance of 0.5 as expected. Though the local amorphisation in the intergranular regions is likely, there are no sufficient reasons to consider an amorphous phase (or local $\alpha - Fe$ de-mixing) as the major factor leading to the decline of coercivity (Figure 6.1 (f)). In this case, the decline in H_c can be attributed to surface disorder, which can lead to a decrease in anisotropy that results in the decline of H_c.

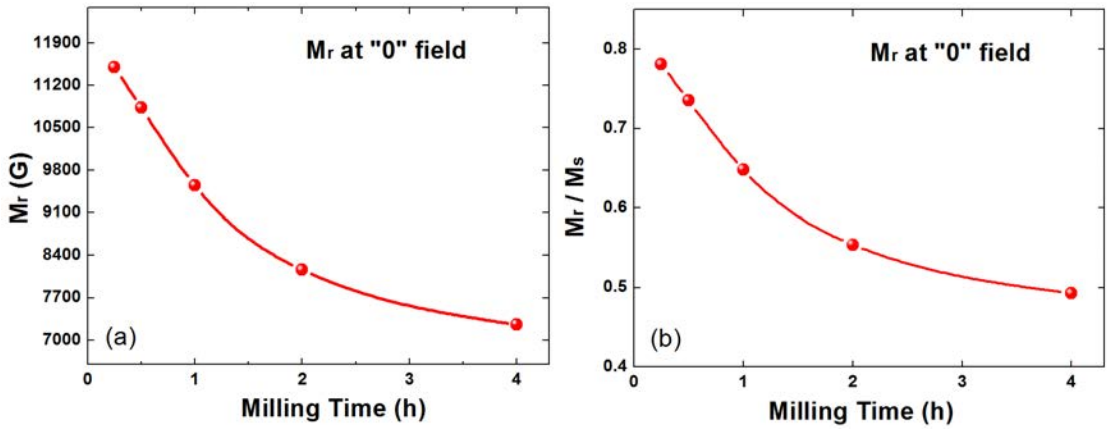

Figure 6.2 (a) Remenance (after demagnetization correction) and (b) Reduced remenance, versus milling time $Nd_2Fe_{14}B$ powders.

6.2.1.2 Dependence of Coercivity on Flake Thickness

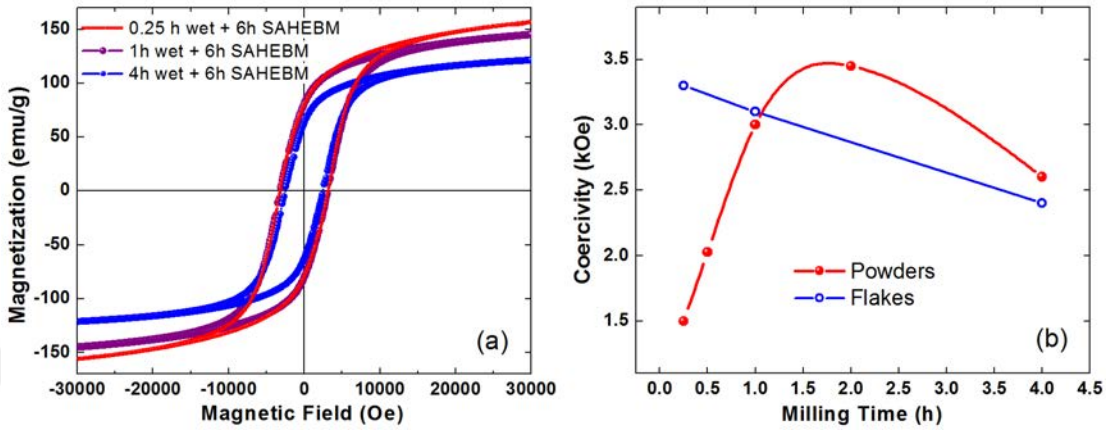

Figure 6.3 (a) The RT hysteresis loops of $Nd_2Fe_{14}B$ flakes with different thicknesses (b) The change in coercivity (pre-milled powders) with milling compared to corresponding flakes.

As mentioned earlier, flakes are formed when surfactants are added during milling. Hysteresis loops of the flakes with different thicknesses (Figure 4.6) can be seen in Figure 6.3. As seen in Figure 6.3 (b), we have observed a great change in coercivity from 1.5 to 3.4 kOe when the flakes were produced using a short time (15 min) pre-milled precursor powders. For longer time pre-milled powders, the change in coercivity is very small (Figure 6.3 (b)). The reason is that 15 min pre-milled precursor powders are lacking complete particle size refinement; therefore, further SA-HEBM causes the change in coercivity to be greater.

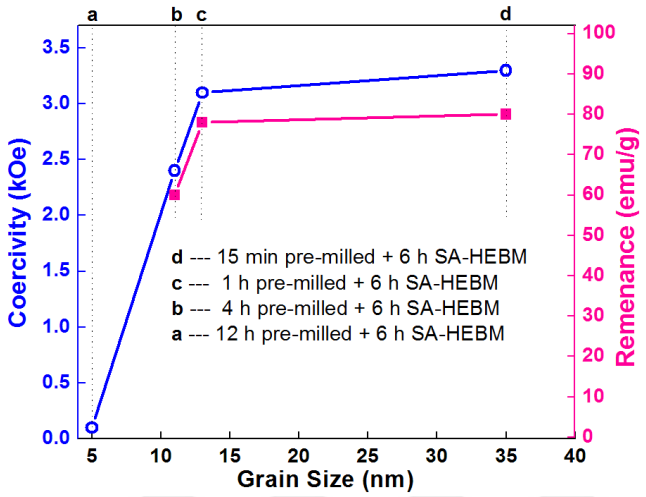

Figure 6.4 The change in coercivity and remenance with grain size of $Nd_2Fe_{14}B$ flakes.

As the flake thickness decreases with milling (Table 4.1) (grain size decreases simultaneously), the coercivity declines (Figure 6.3 (b) and Figure 6.4). The effect of grain size on coercivity for Nd-Fe-B ribbons is different as compared to nano-flakes. Reference [18] showed that grain size refinement leads to an increase in coercivity for Nd-Fe-B micron thick ribbons. Therefore, the apparent difference in behavior of coercivity can be attributed to different surface to volume ratios and to a reduced magnetocrystalline anisotropy of the powders due to the surface effects, which can lead to a decrease in anisotropy that results in the decline of H_c.

The remenance is also decreasing with decreasing grain size, which arises due to the fact that the powders start getting disordered and losing alignment.

6.2.1.3 Texture Studies

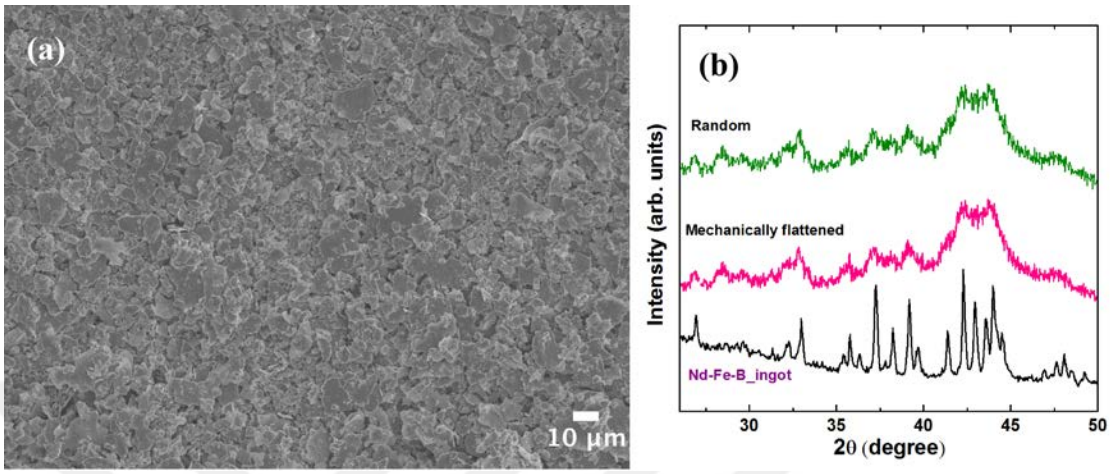

Figure 6.5 (a) SEM image of mechanically flattened $Nd_2Fe_{14}B$ flakes and (b) XRD on random and flattened flakes.

In an attempt to observe the overall texture in the flakes, XRD measurements have been done on random and mechanically flattened flakes (Figure 6.5). XRD data did not exhibit any crystallographic orientation, namely texture, which also shows that the slurry (flakes) mostly consists of randomly oriented polycrystalline grains.

6.3 Nanoparticles

6.3.1 $Nd_2Fe_{14}B$

6.3.1.1 Hysteresis Loops

Because of the high reactivity and oxidation of the nanoparticles, we tried a different technique to measure the hysteresis loop of the nanoparticles. Rather than drying the solution and fixing the particles with wax in a holder, the nanoparticles

have been kept in solution, which was frozen upon cooling to low temperatures in the presence of 3T field to achieve better alignment. The coercivity of the separated nanoparticles at different temperatures is shown in Figure 6.6 (Figure 4.14). When zero-field-cooled, the coercivity of 16 nm particles was found to be 4.9 kOe at 50 K, which is lower than the field-cooled sample (9.1 kOe) due to lack of alignment (Figure 6.6 (inset)).

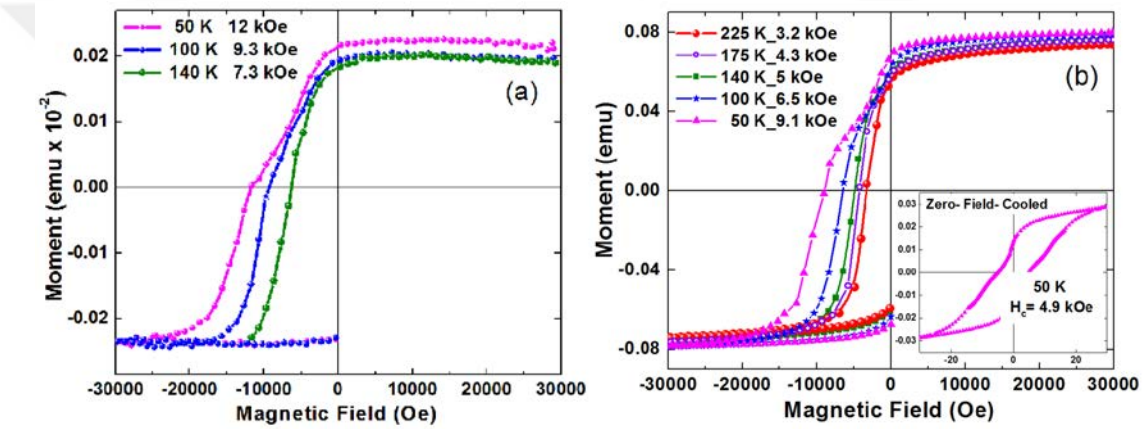

Figure 6.6 Hysteresis loop of separated field-cooled $Nd_2Fe_{14}B$ nanoparticles (a) 25 nm, and (b) 16 nm at different temperatures, insets: zero-field-cooled loop.

The hysteresis loops have been measured at temperatures down to the spin reorientation temperature (140 K) where the anisotropy changes from uniaxial to cone anisotropy [19]. The data showed that, for each particle size, coercivity values are decreasing with increasing temperature, which follows the decrease in magnetocrystalline anisotropy with temperature (Figure 6.7). (The RT coercivity values are estimated when fitted to the temperature dependence of anisotropy field H_a of the nanoparticles and bulk, which is discussed in the previous Chapter)

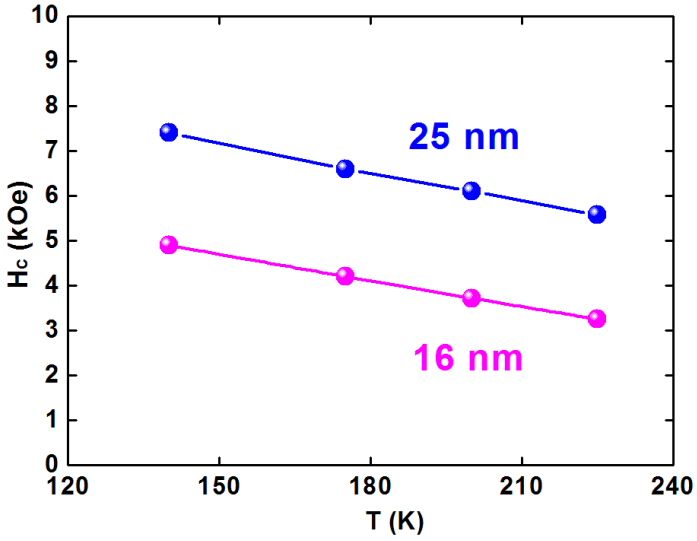

Figure 6.7 Temperature dependence of coercivity in $Nd_2Fe_{14}B$ particles.

6.3.1.2 Particle Size Dependence of Coercivity

As seen in Figure 6.8, the coercivity shows a strong dependence on particle size. As the particle size decreases from 25 nm to 2.7 nm (Figure 4.14), the coercivity declines substantially. The reason for this behavior may be a reduced magnetocrystalline anisotropy of the nanoparticle because of surface disorder and thermal effects. (Discussed further in the previous Chapter)

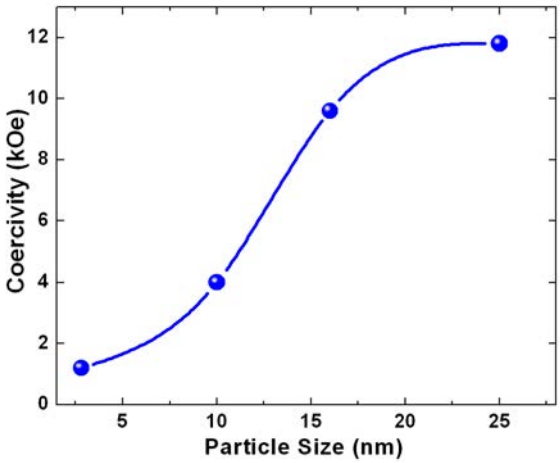

Figure 6.8 The coercivity of the $Nd_2Fe_{14}B$ nanoparticles as a function of particle size at 50 K.

6.4 Magnetic Hardening Studies: Origin of Coercivity

In this section, we investigate the origin of coercivity through correlation between the structural and magnetic data, including size effects and interparticle interaction. Assuming the bulk values of Nd-Fe-B, prediction of room-temperature H_c according to the Stoner-Wohlfarth model [20] is around 35 kOe (H_A=73 kOe). The best result on melt spun Nd-rich Nd-Fe-B ribbons (with grain size around 100 nm) so far is around 27.5 kOe is over 80% of the theoretical limit expected for Stoner-Wohlfarth coherent rotation behavior [21,22].

The coercivity of non-interacting randomly oriented single domain particles is given by

$$H_c = 0.96\frac{K_1}{M_S} \qquad (6.1)$$

Using the experimental values of K_1 (2 10^7 ergs/cc) and M_s (718 emu/cc) determined from the law of approach to saturation, the theoretical value of coercivity is found to be around 26 kOe taking only the K_1 value into account.

As discussed in Chapter 2, a coherent rotation model may be assumed for the coercivity, when the particle size is below the critical single-domain particle size D_c. According to the Stoner-Wohlfarth model [20], the coercivity of a single domain, non-interacting particle system should be proportional to $1-(D_p/D)^{3/2}$ [20]. The size dependence of coercivity for uniaxial particles is given by:

$$H_c(D) = 0.96\frac{K}{M_S}\left[1-(D_p/D)^{3/2}\right] \qquad (6.2)$$

Where D is an isolated particle diameter and D_p is a critical diameter below which the coercivity becomes zero due to superparamagnetism.

Our experimental observations for different size $Nd_2Fe_{14}B$ nanoparticles from the data points suggest that the coercivity dependence on the average particle size is not a perfect fit to the Stoner-Wohlfarth model; but deviation may suggest the presence of particle interaction (Figure 6.9).

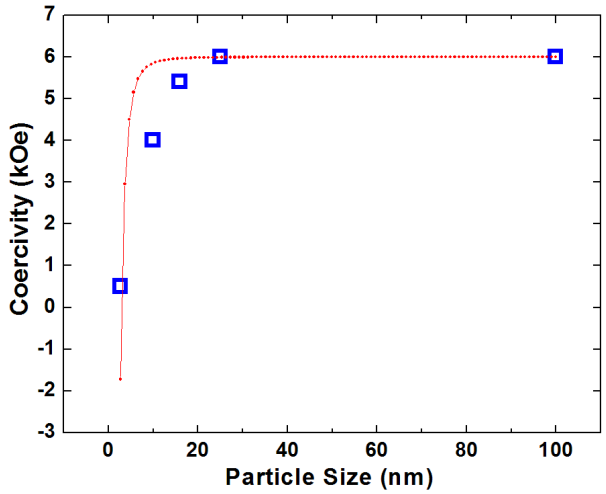

Figure 6.9 Coercivity as a function of grain size for $Nd_2Fe_{14}B$ nanoparticles. Superimposed is a fit of eq. (6.1).

Looking at the results, one can speculate that the magnetization may occur in a mode other than coherent rotation (due to the fact that the fit is not perfect), but it is difficult to reach any concrete conclusions in this matter without any micromagnetic analysis. Particle interactions have been studied for further insight into the behavior.

6.4.1 Particle Interactions

According to the random anisotropy model, overall anisotropy of the system can decrease if there is any interaction occurring in the system. As the anisotropy decreases in the system, the coercivity also decreases. As discussed before, in our system we observed lower coercivities as compared to bulk. In order to see if this phenomenon is due to the interactions between the particles, sigma M plots have been calculated by using the IRM and DCD plots (Figure 6.10 (a)) on $Nd_2Fe_{14}B$ particles with 16 average size (discussed in Chapter 2). $\delta M>0$ represents the presence exchange

interactions and $\delta M<0$ represents the dipolar interactions [23,24]. The calculations were done on the nanoparticles, which have 4 kOe coercivity at RT. As seen in Figure 6.10 (b), δM plots revealed positive values (exchange interaction) around 4 kOe, which may affect the coercivity negatively. Even though it shows positive values of δM, this value is too small (~0.1) to affect the system.

Another method has been applied to the system to confirm the results of δM plots. Magnetic viscosity measurements were used to determine the activation volume, which is related to the reserved magnetized volume [27-30]. Time dependence of moment was fitted to equation 2.19 to find out the viscosity coefficients at different magnetic fields (Figure 6.10 (c)). Figure 6.10 (d) shows the values of S versus applied field. Activation volume was calculated by using the maximum value of S (eq. 2.30). From this, one can find the activation size which was found to be 13.12 nm, which is close the size of the nanoparticles (16 nm). It has been discussed before that there is an exchange interaction if the activation size is bigger than the actual size. This further proved that the lower coercivities in our system cannot be explained solely by exchange interactions between the particles.

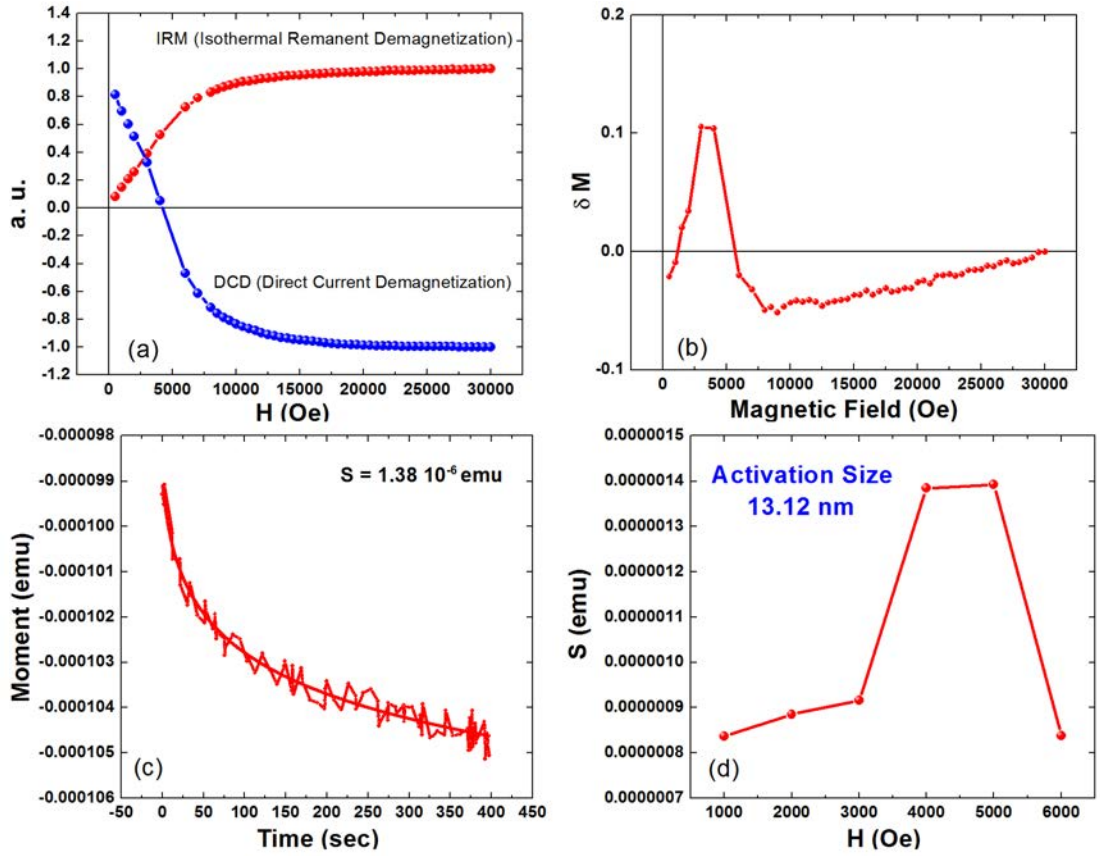

Figure 6.10 (a) IRM & DCD plots, (b) δM plot, (c) Moment vs. Time and (d) viscosity plot on 16 nm $Nd_2Fe_{14}B$ particles.

This is very surprising, according to the Stoner-Wohlfarth fitting, it reveals that the fit is not perfectly suggesting a coherent-type mode, whereas in viscosity studies, the agreement between the grain size and activation size led us to conclude that coherent rotation takes place. A closer look in Figure 6.9 reveals that, the size dependence of H_c deviates from the expression based on a rotation model. One possible reason could be the errors in the calculation of the grain sizes. Another possibility to consider is that the rare-earth based nanoparticles are very prone to oxidation and this could affect the coercivity values thus could alter the Stoner-

Wohlfarth fitting (Figure 6.9). It is difficult to reach any concrete conclusions in this matter without any micromagnetic analysis.

As discussed earlier, the coercivity, which is predicted by Stoner-Wohlfarth model (eq. (6.1)) using $K_1 = 2\ 10^7$ ergs/cc and $M_s = 718$ emu/cc, found to be around 26 kOe for 16 nm particles and the experimental coercivity is only around 5 kOe. The disagreement between the theory and the experiment could be due to a reduced magnetocrystalline anisotropy of the nanoparticles because of surface disorder and thermal effects. Moreover, predicting the coercivity value by Stoner-Wohlfarth model, only first order anisotropy term has been taken into account while K_2 was assumed to be negligible. However, our calculations from Sucksmith and Thomson method showed that the system has considerably high second order anisotropy value.

6.5 Summary

In this chapter, we focused our efforts analyzing the hard magnetic properties of RE-TM compounds for different morphologies. Magnetically hard stoichiometric $Nd_2Fe_{14}B$ nanoparticles and nano-thick flakes were obtained by subjecting a brittle $Nd_2Fe_{14}B$ alloy to a successive wet and surfactant-assisted high energy ball milling (SA-HEBM). It has been observed that hard magnetic properties strongly depend on the size and microstructure of the system. A strong size dependence of coercivity has been observed for $Nd_2Fe_{14}B$, (as well as for $Nd_2(Fe,Mn)_{14}B$ and $NdCo_5$ in Chapter 4) nanoflakes and nanoparticles. Viscosity measurements revealed that there is no exchange interaction in the system. The coercivity, which is predicted by Stoner-Wohlfarth model, found to be around 26 kOe for 16 nm particles and the experimental coercivity is only around 5 kOe. Therefore, the disagreement between the theory and

the experiment may be due to a lower anisotropy of the nanoparticles because of size and surface effects and to thermal effects, as further discussed in chapter 5.

Fabrication of the magnetically anisotropic nanoparticles is seen as an important step in the development of the next-generation hard magnetic materials; such particles may serve as precursors for the bottom-up fabrication of anisotropic exchange-coupled nanocomposite magnets consisting of a fine mixture of magnetically hard and soft particles.

REFERENCES

1. P. Gaunt, *Phil. Mag.* 17, 263 (1968).
2. P. Gaunt, *Phil. Mag.* B 48, 261 (1983).
3. B. D. Cullity 1972 Introduction to Magnetic Materials (Reading, MA, USA: Addison-Wesley).
4. D. Jales Introduction to Magnetism and Magnetic Materials; CRC Press, Boca Raton, FL, (1998).
5. R. A. McCurrie and G. P. Carswell *Philosophical Magazine* 28, 611 (1973).
6. V. M. Chakka, B. Altuncevahir, Z. Q. Jin, Y. Li and J. P. Liu *J. Appl. Phys.* 99, 08E912 (2006).
7. N. G. Akdogan, G. C. Hadjipanayis and D. J. Sellmyer *J. Appl. Phys.* 105, 07A710 (2009).
8. Y. Wang, Y. Li, C. Rong and J. P. Liu *Nanotechnology* 18, 465701 (2007).
9. H. G. Cha, Y. H. Kim, C. W. Kim, H. W. Kwon and Y. S. Kang *J. Phys. Chem.* 111, 1219 (2006).
10. M. Yue, Y. P. Wang, N. Poudyal, C. B. Rong and J. P. Liu *J. Appl. Phys.* 105, 07A708 (2009).
11. L. Schultz, J. Wecker and E. Hellstern *J. Appl. Phys.* 61, 3583 (1987).
12. J. Han, S. Liu, X. Zhang, H. Du, C. Wang, Y. Yang, M. Yue and X. Liu *J. Appl. Phys.* 101, 09K502 (2007).
13. E. M. Kirkpatrick, S. A. Majetich and M. E. McHenry *IEEE Trans. Magn.* 32, 4502 (1996).
14. J. I. Lee, H. W. Kwon and Y. S. Kang *J. of Magnetics* 13, 102 (2008).
15. A. M. Gabay, N. G. Akdogan, M. Marinescu, J. F. Liu and G. C. Hadjipanayis *J. Phys.: Condens. Matter.* 22, 164213 (2010).

16. G. Herzer, *IEEE Trans. Magn. 26*, 1397 (1990).

17. R. Alben, J. J. Becker and M. C. Chi *J. Appl. Phys. 49*, 1653 (1978).

18. T. Harada and T. Kuji D Center*, J. Appl. Phys.* 72, 5443 (1992).

19. K. H. J. Buschow *Rep. Prog. Phys* 40, 1179 (1977).

20. E. C. Stoner and E. P. Wohlfarth *Phil. Trans. Roy. Soc. London.* A240, 599 (1948).

21. E. Girt, K.M. Krishnan and G. Thomas *Scripta Mater.* 44, 1431 (2001).

22. E. Girt, M. K. Kannan, G. Thomas, E. Girt, Z. Altounian *J. of Magn. and Magn. Mat.* 231, 219 (2001).

23. R. Alben, J. J. Becker and M. C. Chi *J. Appl. Phys. 49*, 1653 (1978).

24. R. W. Chantrell, K. O'Grady, *Appl. Magn. 253*, 113 (1994).

25. K. O'Grady, R. W. Chantrell, Proceedings of the International Workshop on Studies of Magnetic Properties of Fine Particles 93 (1992).

26. L. Neel *J. Phys. Rad.* 11, 40 (1959).

27. R. Street, J.C. Woolley and P.B. Smith *Proc. Phys. Soc. B* 65, 679 (1952).

28. E. P. Wohlfarth *J. Phys. F: Met. Phys.* 14, 1155 (1984).

29. P. Gaunt *J. Appl. Phys.* 59, 4129 (1986).

30. A. Lyberatos and R. Chantrell *J. Phys. D: Appl. Phys.* 29, 2332 (1996).

Chapter 7

CONCLUSIONS and RECOMMENDATIONS

7.1 Conclusions

RE-TM nanoparticles and nanoflakes have been fabricated by the novel technique of surfactant-assisted high-energy ball milling. Most of the studies were focused on the understanding of their formation and the understanding of their fundamental and hard magnetic properties as a function of size and shape.

A strong correlation between the grain size of the nanoflakes and the size of the nanoparticles has been observed. The data suggests that the nanoparticles break away from the nanoflakes along the grain boundaries during milling. Our studies on different surfactants have revealed that the type of surfactant is the key to fabricate nanoparticles and nanoflakes and none of the surfactants we have tried so far (List !!) is as compatible as OA to provide the right dielectric environment. To investigate further what triggers the formation of either the nanoflakes or the nanoparticles, we investigated the influence of different grain microstructures of the precursor powders. It is evident that microstructure of the grains within the particles is the determinant in this process and that the formation of particles occurs through breakage of the grains into submicron particles along the grain boundaries.

For the first time, mono dispersed self-assembled $Sm_2(Co_{0.8}Fe_{0.2})_{17}$ nanoparticles have been observed with ultra-narrow size distribution after 4 h of SA-HEBM using novel SA-HEBM technique. Room-temperature coercivities have been obtained with maximum value of 2.9 kOe. In $Nd_2Fe_{14}B$, the nanopowders consisted of

flakes with a thickness below 100 nm and an aspect ratio as high as 10^2–10^3 and anisotropic square and irregular shape nanoparticles with a size from 2.7 to 25 nm. This is the first production of $Nd_2Fe_{14}B$ nano-cubes. The coercivity shows a strong dependence on particle size. As the particle size decreases from 25 nm to 2.7 nm, the coercivity declined substantially. High field magnetization measurements fitted the data to the law of approach to saturation result in lower anisotropy (~$2x10^7$ ergs/cc) and saturation magnetization value (718 emu/cc). The coercivity, which is predicted by Stoner-Wohlfarth model using K_1= $2x10^7$ ergs/cc and M_s= 718 emu/cc, found to be around 26 kOe for 16 nm particles and the experimental coercivity is only around 5 kOe. This value is significantly lower than that predicted by the Stoner-Wohlfarth model for randomly distributed uniaxial single domain particles. The disagreement in coercivity between the theory and the experiment could be due to a reduced magnetocrystalline anisotropy of the nanoparticles because of surface disorder and thermal effects. Lower anisotropies and saturation magnetization values were observed in the nanoparticles, indicate a strong size effect due to size and surface effects.

It has been shown that, size dependence of room temperature coercivity follows the trend theoretically predicted by Stoner-Wohlfarth for the coherent rotation where non-interacting randomly oriented single domain particles with uniaxial anisotropy are assumed.

Curie temperature studies have been carried out on Mn substituted $Nd_2Fe_{14}B$ nanoparticles and nanoflakes. Bulk samples have a Curie temperature, close to room temperature which make the measurements easier because of the absence of oxidation problems. The effect of different particle size and morphologies were investigated. An

enhancement in Curie temperature has been observed for the first time in rare-earth based compounds when all three dimensions are reduced without any change in the composition and structure. The enhancement in Curie temperature from that of the bulk is well described by the finite-size-scaling law with the proper exponent and characteristic microscopic dimension.

Lower spin reorientation temperatures have been observed in $Nd_2Fe_{14}B$, $Nd_2Fe_{14-x}Mn_xB$ and $NdCo_5$ nanoparticles as compared to bulk. Lower anisotropy constants have also been observed in these nanoparticles and this could be the reason for the lower spin reorientation temperatures.

Besides the fundamental interest, these nanoparticles and nanoflakes are good candidates and may serve as precursors for the bottom-up fabrication of anisotropic exchange-coupled nanocomposite magnets consisting of a fine mixture of magnetically hard and soft particles.

7.2 Recommendations

As seen in Chapter 4, SA-HEBM is a very powerful technique to produce different size nanoparticles. The only drawback is the lack of fabricating larger size nanoparticles. In order to study the size effects more extensively, this problem should be addressed. There are different techniques that can be applied to resolve this issue, such as, planetary ball milling, jet-milling, combination of the two and unique separation methods.

Of fundamental importance is the behavior of the systems in which all three dimensions are limited and in order to better understand the unique behavior of nanoparticles and especially the origin of low coercivities and anisotropies. It would

be interesting to study the surface/interface, the composition and structure of the nanoparticles using neutron scattering measurements.

Observed enhancement in Curie temperature for the first time for the rare-earth based nanoparticles is an interesting phenomenon and need to be further investigated on different low-Curie-temperature RE systems. That study might help to get a more insight about this unique behavior.

Technically, unlike regular dry milling in argon, SA-HEBM, being a wet-milling technique, is a lot more complicated and one should be meticulous in handling the experiments. First of all, this gives rise to fast oxidation of powders especially for small sizes. Long term storage of either the flakes and nanoparticles (couple of days) should be strictly avoided.